



# PACIFIC EARTHQUAKE ENGINEERING RESEARCH CENTER

## **Workshop on Modeling of Nonlinear Cyclic Load- Deformation Behavior of Shallow Foundations**

**Wednesday, March 5, 2003**  
**University of California, Davis**

**Bruce L. Kutter**

University of California, Davis

**Geoffrey Martin**

University of Southern California, Los Angeles

**Tara Hutchinson**

University of California, Irvine

**Chad Harden**

University of California, Irvine

**Sivapalan Gajan**

University of California, Davis

**Justin Phalen**

University of California, Davis

# **Workshop on Modeling of Nonlinear Cyclic Load- Deformation Behavior of Shallow Foundations**

**Wednesday, March 5, 2003  
University of California, Davis**

**Bruce L. Kutter**

Department of Civil and Environmental Engineering  
University of California, Davis

**Geoffrey Martin**

University of Southern California, Los Angeles

**Tara Hutchinson**

University of California, Irvine

**Chad Harden**

University of California, Irvine

**Sivapalan Gajan**

University of California, Davis

**Justin Phalen**

University of California, Davis

PEER Report 2005/14  
Pacific Earthquake Engineering Research Center  
College of Engineering  
University of California, Berkeley

March 2006

## ABSTRACT

A PEER-sponsored workshop on the nonlinear cyclic load-deformation behavior of shallow foundations was held at UC Davis on March 5, 2003. This report contains all of the documents distributed for discussion prior to that workshop and closes with a summary chapter based on workshop discussions.

### Goals of the Workshop:

- To disseminate a summary of research findings from the PEER multi-campus research project on shallow foundations and to discuss a plan for future related research.
- To receive feedback from structural engineers, practicing engineers, and geotechnical peers to improve the design of the last model test series and to provide some helpful direction in the ongoing development of procedures to analyze and predict highly nonlinear moment-rotation, shear-sliding, and axial load-settlement behavior of footings for shear walls.

### Attendees:

M. Allen  
R. Bachman  
R. Boulanger  
S. Brandenberg  
R. Chai  
D. Chang  
S. Choi  
C. Comartin

G. Deierlein  
S. Gajan  
S. Polat  
T. Hale  
T. Hutchinson  
C. Harden  
B. Jeremic  
S. Kunnath

B.L. Kutter  
P. Lam  
G. Martin  
M. Moore  
J. Phalen  
T. Shantz  
D. Wilson  
K. Yu

## **ACKNOWLEDGMENTS**

This work was supported by the Pacific Earthquake Engineering Research (PEER) Centers Program of the National Science Foundation under award number EEC-9701568 and PEER project number 2262001. Any opinions, findings, and conclusions or recommendations expressed in this material are those of the author(s) and do not necessarily reflect those of the National Science Foundation.

The coordinators, B.L. Kutter, G. Martin, and T. Hutchinson, would like to thank PEER for ongoing support of these research efforts. Without the support of PEER and the National Science Foundation, this important research would not be possible. The coordinators also thank the workshop participants, both academic and industrial, for their time and valuable input given to this research program.

# CONTENTS

<b>ABSTRACT</b> .....	<b>iii</b>
<b>ACKNOWLEDGMENTS</b> .....	<b>iv</b>
<b>TABLE OF CONTENTS</b> .....	<b>v</b>
<b>LIST OF FIGURES</b> .....	<b>ix</b>
<b>LIST OF TABLES</b> .....	<b>xv</b>
<b>1 INTRODUCTION</b> .....	<b>1</b>
<b>2 BACKGROUND</b> .....	<b>3</b>
2.1 Nonlinear Stiffness and Capacity Model Concepts.....	5
2.2 Moment-Rotation Capacity Concepts.....	6
2.3 Rocking Behavior of Shear Walls.....	8
2.4 Evaluation of Deformations and Settlement Due to Moment Yield and Model Concepts.....	10
2.4.1 Experimental Studies.....	10
2.4.1.1 One g Model Tests.....	10
2.4.1.2 Centrifuge Model Tests.....	11
2.4.2 Theoretical Simulation Using FLAC.....	12
2.4.3 Nonlinear Interface Models for Structural Computer Codes.....	12
2.5 Summary.....	13
<b>3 CENTRIFUGE MODEL TESTS</b> .....	<b>25</b>
3.1 Summary of Model Tests.....	27
3.1.1 Overview.....	27
3.1.2 Configuration of the Structures.....	27
3.1.3 Soil Properties.....	28
3.1.4 Instrumentation.....	30
3.1.5 Summary of All Tests Conducted.....	30
3.1.6 Time Histories of Input.....	31
3.2 Data Reports.....	32
3.3 Data Analysis.....	34
3.3.1 Effect of Vertical Load F.S. on Maximum Moment and Shearing Behavior...34	
3.3.2 Verification of a Three-Dimensional Failure Surface.....	36

3.3.3	Settlement-Rotation Relationships.....	36
3.3.4	Slow Cyclic vs. Dynamic Events.....	37
3.4	Considerations in Planning Future Experiments.....	38
3.5	Summary and Major Findings.....	40
<b>4</b>	<b>NONLINEAR WINKLER-BASED MODELING.....</b>	<b>65</b>
4.1	Introduction.....	65
4.2	Background and Previous Work.....	67
4.2.1	Numerical Studies.....	67
4.2.2	Case Studies.....	69
4.2.3	Observations from the Literature Review.....	70
4.3	OpenSees Implementation.....	70
4.3.1	One-Dimensional Material Response.....	71
4.3.2	Determination of Winkler Spring Properties.....	73
4.3.2.1	Vertical and Rotational Spring Stiffness.....	73
4.3.2.2	Ultimate Bearing Capacity.....	74
4.3.3	Model and Simulation Details.....	75
4.3.4	BNWFShallow Mesh Generator.....	76
4.3.4.1	Lateral Spring Distribution.....	76
4.3.4.2	Bearing Pressure Distribution.....	77
4.3.5	Experimental-Numerical Comparisons in OpenSees.....	77
4.3.5.1	Centrifuge Experiments.....	78
4.3.5.2	One-g Experiments.....	80
4.3.5.2.1	ELSA Laboratory Experiments.....	80
4.3.5.2.2	New Zealand Experiments.....	80
4.4	Sensitivity Study and Discussion of Results.....	82
4.4.1	Bearing Capacity Distribution and Magnitude.....	82
4.4.2	Spring Stiffness.....	83
4.4.3	Tension Capacity.....	84
4.4.4	Distribution of Springs.....	84
4.5	Analysis of Experimental Results.....	85
4.5.1	Energy Dissipation and Equivalent Viscous Damping.....	85
4.6	Additional Plans for the Study.....	87

4.6.1	Additional Available Experimental Datasets .....	87
4.6.2	Combined Nonlinear Structure and Soil-Interface Analysis.....	87
4.7	Summary and Major Findings.....	87
<b>5</b>	<b>MACRO-ELEMENT MODEL .....</b>	<b>113</b>
5.1	Introduction.....	113
5.2	Nova and Montrasio (1991) Model.....	114
5.2.1	Generalized Forces and Displacements .....	114
5.2.2	Interaction Diagrams and Failure Envelope.....	115
5.2.3	Yield Surface and Hardening Law .....	115
5.2.4	Plastic Potential and Flow Rule .....	116
5.3	Houlsby and Cassidy (2002) Model.....	116
5.3.1	Elastic Behavior .....	117
5.3.2	Yield Surface.....	117
5.3.3	Hardening Law.....	118
5.3.4	Plastic Potential.....	118
5.4	Cremer et al. (2001) Model.....	119
5.4.1	Plasticity Model .....	120
5.4.1.1	Elastic Behavior.....	120
5.4.1.2	Failure Envelope.....	120
5.4.1.3	Yield Surface .....	121
5.4.1.4	Hardening Laws.....	122
5.4.1.5	Plastic Potential and Flow Rule.....	123
5.4.2	Uplift Model.....	124
5.4.2.1	Uplift Model for Elastic Soil .....	124
5.4.2.2	Uplift Model for Elasto-Plastic Soil .....	125
5.5	Implementation of Cremer et al. (2001) Model Plasticity Model.....	126
5.5.1	Explicit Method.....	127
5.5.2	Implicit Method .....	127
5.6	Summary .....	128
<b>6</b>	<b>SUMMARY AND PRELIMINARY CONCLUSIONS.....</b>	<b>135</b>
6.1	Centrifuge Model Tests.....	136
6.2	Modeling Foundation Behavior Using the BNWF Approach .....	137

6.3	Macro-Element Modeling .....	138
6.4	Comments and Suggestions from Workshop Participants .....	138
6.5	Update and Future Directions .....	140
6.5.1	Subgrade Reaction Spring Modeling in OpenSees .....	140
6.5.2	Macro-Element Modeling in OpenSees .....	140
6.5.3	Centrifuge Model Testing .....	140
6.5.4	An Eye on the Bigger Picture .....	141
<b>REFERENCES.....</b>		<b>143</b>

## LIST OF FIGURES

Fig. 2.1	Building capacity and global displacement capacities for various performance levels (after Shapiro et al., 2000) .....	16
Fig. 2.2	Uncoupled elasto-plastic spring model for rigid footings.....	16
Fig. 2.3	Shallow foundation model (ATC 1996) .....	17
Fig. 2.4	Basic force-displacement envelope for geotechnical components (ATC 1996).....	17
Fig. 2.5	Global and foundation modeling alternatives (after ATC, 1996).....	18
Fig. 2.6	Idealized concentration of stress at edge of rigid footings subjected to overturning moment (after ATC, 1997a).....	19
Fig. 2.7	Rocking of shear wall on strip footing (after ATC, 1997b).....	19
Fig. 2.8	Shear wall and frame example (after ATC, 1997b).....	20
Fig. 2.9	Foundation stiffness and capacity of footing (after ATC, 1997b) .....	20
Fig. 2.10	Experimental apparatus: The motor unit attached to the wall at the top of the picture rocks the footing via the vertical frame .....	21
Fig. 2.11	Representative results from the University of Auckland Tests (after Taylor et al., 1981) .....	21
Fig. 2.12	Scheme of the experimental setup (after Faccioli, 2001) .....	22
Fig. 2.13	Representative Test Results (after Faccioli, 2001) .....	22
Fig. 2.14	Simulated behavior of Type B footing on clay: $F_v = 1.5$ .....	23
Fig. 2.15	Simulated behavior of Type B footing on clay: $F_v = 3.0$ .....	23
Fig. 3.1	Nomenclature for force and displacement parameters associated with a displaced footing.....	41
Fig. 3.2a	Two views of structure and footing used for a double-wall test. Displacement transducers and actuator locations are also indicated. All dimensions are in model scale millimeters .....	42
Fig. 3.2b	Two views of standard weight shear wall made of aluminum (left) and heavy shear wall made of steel (right) used in single-wall tests. Displacement transducers and actuator locations are also indicated. All dimensions are in model scale millimeters .....	42
Fig. 3.3	Side view of model container with selected wall and footing locations with typical instrument configuration for slow cyclic tests.....	43

Fig. 3.4	Load vs. settlement plots from slow cyclic vertical load tests for (a) KRR01-S2, (b) KRR01-S25, (c) KRR01-S31, (d) KRR02-S54, (e) SSG02 and (f) SSG02.....	44
Fig. 3.5a	Slow cyclic single aluminum wall ready for testing.....	45
Fig. 3.5b	Low horizontal slow cyclic test arrangement, aluminum wall .....	45
Fig. 3.5c	Teflon pads provide support to the single wall system, restricting movement in the transverse direction .....	45
Fig. 3.5d	Settlement and soil wedge failure after standard height horizontal slow cyclic test with heavy (steel) wall.....	46
Fig. 3.5e	Footing imprint preservation after horizontal slow cyclic test with sand surface pre-treated with WD40 .....	46
Fig. 3.5f	Dynamic test configuration with single steel wall (foreground) and double aluminum wall (background).....	46
Fig. 3.6	(a) Time histories of a horizontal slow cyclic test input motion (bottom), two horizontal potentiometer positions (middle) and two vertical potentiometer positions (top). SSG02, test#3a; (b) Acceleration time histories of a dynamic test input base motion (bottom), middle of soil deposit (2 <sup>nd</sup> from bottom) and response of footing, middle and top part of structure. SSG02, test#9e.....	47
Fig. 3.7a	Data from test SSG02, test#3a, FS = 6.7, embedment = 0.0m, load height = 4.9m, footing length = 2.84m.....	48
Fig. 3.7b	Data from test SSG02, test#6a, FS = 6.7, embedment = 0.0m, load height = 1.16m, footing length = 2.84m.....	49
Fig. 3.7c	Data from test SSG02, test#6b, FS = 6.7, embedment = 0.0m, load height = 1.16m, footing length = 2.84m.....	50
Fig. 3.7d	Data from test SSG02, test#5a, FS = 3.3, embedment = 0.0m, load height = 4.82m, footing length = 2.84m.....	51
Fig. 3.7e	Data from test SSG02, test#5b, FS = 3.3, embedment = 0.0m, load height = 4.82m, footing length = 2.84m.....	52
Fig. 3.7f	Data from test SSG03, test#2a, FS = 8.4, embedment = 0.7m, load height = 4.96m, footing length = 2.84m.....	53
Fig. 3.7g	Data from test SSG03, test#2b, FS = 8.4, embedment = 0.7m, load height = 4.96m, footing length = 2.84m.....	54

Fig. 3.7h	Data from test SSG03, test#8c, d, and e, FS = 6.7, embedment = 0.7m, footing length = 2.84m .....	55
Fig. 3.7i	Time histories of settlement, rotation and horizontal displacement; SSG03, dynamic tests, test#8a, b, and c.....	56
Fig. 3.8	Determination of maximum moment, yield moment, and yield rotation from the development of a backbone curve in a moment-rotation plot. SSG02 test#3a.....	57
Fig. 3.9	Maximum moment failure envelope from current test series and other theoretical surfaces .....	58
Fig. 3.10	Maximum shear load failure envelope from current test series and theoretical parabolic surface after Cremer et al. (2001) .....	59
Fig. 3.11	Elliptical cross sections of the failure envelope in constant V planes .....	59
Fig. 3.12	Relationship between normalized settlement per cycle and half-amplitude cyclic rotation .....	60
Fig. 3.13	Comparison of dynamic data trend line with slow-cyclic moment-rotation. KRRO02, test KRR02-S21 after Rosebrook, 2001 (left) and SSG02, test#3a (right).....	61
Fig. 4.1	Winkler foundation concepts (after Broms, 2003) .....	91
Fig. 4.2	Example series of Winkler springs below a rigid foundation represented by two-dimensional finite elements (after Boulanger et al. 1999).....	91
Fig. 4.3	Idealized foundation system by Chopra and Yim (1985): (a) rigid foundation, (b) two-element (spring-dashpot) system, and (c) distributed Winkler (spring-dashpot) system.....	92
Fig. 4.4	Moment-rotation envelope assuming different idealized foundations (Chopra and Yim, 1985) .....	92
Fig. 4.5	Winkler-foundation system below a model inelastic shearwall (Nakaki and Hart 1987) .....	93
Fig. 4.6	Ductility demand versus period relation for structures allowing and preventing uplift (results from analyses using the El Centro earthquake) (Nakaki and Hart, 1987) .....	93
Fig. 4.7	Hysteretic material backbone curve: (a) single material and (b) multiple hysteretic material elements placed in parallel.....	94

Fig. 4.8	Comparison of material response – single element parallel hysteretic and qzsimple1 material in OpenSees.....	94
Fig. 4.9	Determination of maximum and minimum vertical ( <i>apparent elastic</i> ) stiffnesses based on elasto-plastic idealization of experimental data.....	95
Fig. 4.10	Vertical stiffness determination from pure compression experiments, compared with elastic-half space stiffness solutions provided by Gazetas (1991): (a) vertical stiffness versus design $FS_v$ and (b) ratio of vertical stiffness estimates (max and min experimental) normalized by Gazetas (1991) stiffness versus design $FS_v$ .....	95
Fig. 4.11	Compensation for highly coupled vertical and rotational system stiffness as recommended in ATC-40 (1996).....	96
Fig. 4.12	Lateral spring distributions in <i>BNWFShallow</i> mesh generator.....	97
Fig. 4.13	Bearing capacity distributions available in <i>BNWFShallow</i> mesh generator.....	97
Fig. 4.14	Comparison of experimental and numerical simulation of rocking shallow foundation: (a) moment-rotation response and (b) settlement-rotation response. Experimental dataset: KRR02-S21 (Parameters: Centrifuge, Sand, small footing, $FS_v = 3.0$ ).....	98
Fig. 4.15	Comparison of experimental and numerical simulation of rocking shallow foundation: (a) moment-rotation response, (b) settlement-rotation response, and (c) lateral base displacement versus pseudo-time. Experimental dataset: KRR02-S38 (Parameters: Centrifuge, Sand, large footing, $FS_v = 6.2$ ).....	99
Fig. 4.16	Comparison of experimental and numerical simulation of rocking shallow foundation: (a) moment-rotation response and (b) settlement-rotation response. Experimental dataset: KRR03-S18 (Parameters: Centrifuge, Clay, small footing, $FS_v = 2.8$ ).....	100
Fig. 4.17	Comparison of experimental and numerical simulation of rocking shallow foundation: (a) moment-rotation response, (b) settlement-rotation response, and (c) lateral base displacement versus pseudo-time. Experimental dataset: TRISEE83 (Parameters: One-g, (low density) sand, square footing, $FS_v = 2.0$ ).....	101
Fig. 4.18	Comparison of experimental and numerical simulation of rocking shallow foundation: moment-rotation and settlement-rotation response: (a) Type A footing ( $FS_v = 2.0$ ), (b) Type A footing ( $FS_v = 5.0$ ) and (c) Type B footing ( $FS_v = 5.0$ ) Experimental dataset: Weissing (1979) (Parameters: One-g, and sand).....	102

Fig. 4.19	Comparison of experimental and numerical simulation of rocking shallow foundation: moment-rotation and settlement-rotation response: (a) Experimental response and (b) numerical response. Experimental dataset: Bartlett (1976) (Parameters: One-g, clay, Type B footing and $FS_v = 1.5$ ).....	104
Fig. 4.20	Comparison of experimental and numerical simulation of rocking shallow foundation: moment-rotation and settlement-rotation response: (a) Experimental response and (b) numerical response. Experimental dataset: Bartlett (1976) (Parameters: One-g, clay, Type A footing and $FS_v = 3.0$ ).....	105
Fig. 4.21	Sensitivity of analysis results considering varying end tip resistance $q_i$ : (a) moment-rotation behavior and (b) settlement-rotation behavior (KRR02-S21 Series data).....	106
Fig. 4.22	Sensitivity of analysis results considering varying bearing capacity factors $F_Q$ : (a) moment-rotation behavior and (b) settlement-rotation behavior (KRR02-S21 Series data).....	106
Fig. 4.23	Sensitivity of analysis results considering varying end length $L_{ep}$ : (a) moment-rotation behavior and (b) settlement-rotation behavior (KRR02-S21 Series data)....	107
Fig. 4.24	Sensitivity of analysis results considering varying vertical spring stiffness: (a) moment-rotation behavior and (b) settlement-rotation behavior (KRR02-S21 Series data).....	107
Fig. 4.25	Sensitivity of analysis results considering variations in suction (as a function of total compression capacity): (a) moment-rotation behavior and (b) settlement-rotation behavior (KRR02-S21 Series data).....	108
Fig. 4.26	Sensitivity of analysis results considering varying lateral spring distribution: (a) moment-rotation behavior and (b) settlement-rotation behavior (KRR02-S21 Series data).....	108
Fig. 4.27	Sensitivity of moment-rotation behavior results considering varying lateral spring distributions: (a) fine mesh, (b) medium-fine mesh, and (c) coarse mesh. (KRR02-S21 Series data).....	109
Fig. 4.28	Equivalent linear system approach (after Chopra and Goel 1999): (a) inelastic system bilinear response and (b) determination of equivalent viscous damping due to hysteretic energy dissipation.....	110
Fig. 4.29	Estimation of equivalent damping using experimental M- $\theta$ data.....	111

Fig. 4.30	Effective viscous damping versus maximum footing distortion (settlement normalized by footing length) per cycle: (a) sand data and (b) clay data.....	111
Fig. 5.1	Sign conventions for load and displacements (after Houlsby and Cassidy, 2002)....	129
Fig. 5.2	Failure envelope in $(F_H-F_V)$ plane (after Nova and Montrasio, 1991).....	129
Fig. 5.3	Failure envelope in $(F_H-F_V)$ plane (after Nova and Montrasio, 1991).....	130
Fig. 5.4	Shape of the yield surface in $(V, H, M/2R)$ space (after Houlsby and Cassidy, 2002).....	130
Fig. 5.5	Failure envelope in $(F_V-F_H-F_M)$ space (after Cremer et al., 2001).....	130
Fig. 5.6	Types of loading path preferentially developed during seismic action for a structure with one predominant mode (after Cremer et al., 2001).....	131
Fig. 5.7	Evolution of the loading surface (after Cremer et al., 2001).....	131
Fig. 5.8	Relationship between isotropic and kinematic hardening parameters.....	132
Fig. 5.9	Non-interpenetration criterion (after Cremer et al., 2001).....	132
Fig. 5.10	Non-associative flow rule. External normals of the loading surface and of the plastic potential (after Cremer et al., 2001).....	133
Fig. 5.11	Iso-uplift surfaces and failure criterion in the $(F_M - F_H)$ plane (after Cremer et al., 2001).....	133
Fig. 5.12	Coupling between plasticity and uplift (Cremer et al., 2001).....	134

## LIST OF TABLES

Table 3.1	Centrifuge scale factors for basic parameters .....	62
Table 3.2	Determination of friction angle from vertical load tests .....	62
Table 3.3	Summary of the methods used to determine $c_u$ .....	62
Table 3.4	Test event summary .....	63
Table 3.5	Strength and yield characteristics for standard height horizontal slow cyclic tests.....	64
Table 3.6	Proposed tests for SSG03.....	64
Table 4.1	Details of experimental-numerical specimen results presented.....	89
Table 4.2	Summary of BNWF simulation details for modeled experiments.....	90

# 1 Introduction and Scope of Workshop

One of the major changes in the traditional seismic design procedures adopted in the 1997 *NEHRP Guidelines for the Seismic Rehabilitation of Buildings* (FEMA, 1997) was that by allowing mobilization of the ultimate capacity and rocking behavior of shallow foundations, the ductility demands on structures could be reduced, particularly for shear walls. The related problems of nonlinear foundation interface model development and the predictions of earthquake-induced permanent foundation settlement and structural performance provide analytical challenges to both geotechnical and structural engineers. These challenges form the basis for this project.

During large seismic events soil-foundation interaction associated with heavily loaded shear walls during may produce highly nonlinear behavior. The results available from recent research indicate that moment-rotation hysteresis curves display excellent ductility. Hence, there is a good potential for foundations to dissipate a large amount of energy, thereby reducing ductility demands on the shear wall. Critical side effects of nonlinearity are permanent deformations of the footings. A goal of this PEER research project is to provide tools to allow engineers to account for this nonlinearity and settlement when evaluating the performance of structures with heavily loaded shear walls. The tools will include simple procedures for design codes and more general tools such as finite elements and corresponding mesh generation tools implemented in the PEER computer program OpenSees.

This report summarizes the research findings to date from the PEER multidisciplinary research project on the nonlinear cyclic load-deformation behavior of shallow foundations. The project was initiated in 2000 following the preparation of a background study by Geoff Martin (USC) defining the significance of nonlinear load-deformation behavior and the scope of needed research. Subsequent centrifuge and analytical modeling studies have been conducted at UC Davis (Bruce Kutter, co-PI) and UC Irvine (Tara Hutchinson, co-PI) in 2001 and 2002. The need for comment and input from the PEER research community and practicing professional

engineers to guide continuing research was recognized by the PIs at the end of 2002, leading to the March 2003 “Workshop on Modeling Nonlinear Cyclic Load-Deformation Behavior of Shallow Foundations.”

The background study leading to the initiation of the project is summarized in Chapter 2 of this report. Model testing has been performed over the past two years in the centrifuge at UC Davis to provide quantitative data under realistic combinations of moment, axial, and shear loads on the foundation and realistic confining pressures in the soil. Some of the parameters varied in the experiments are the factors of safety of the foundation with respect to axial loads, the height of application of the cyclic lateral load, and the embedment depth of the foundation. In some experiments, cyclic loads were applied to a shear wall slowly by an actuator. In other tests, the base of the soil container was shaken so that dynamic loads were transmitted through the foundation to a model building structure. Test results to date are summarized in Chapter 3.

Analysis performed to date includes the development of numerical tools for modeling the nonlinear rocking behavior and predicting associated foundation and building settlements, and validating these tools against available experimental data. A main focus is the development of a nonlinear Winkler-type framework for modeling the soil-structure interaction (i.e., using nonlinear springs and dashpots with gapping elements). A single-element “macro-model” based on plasticity theory is also being explored as an alternative method of modeling the soil-foundation interaction. The Winkler-type framework is described in Chapter 4, while the macro-model is described in Chapter 5. The project also includes an explicit effort to integrate the experimental and analytical work into the framework of performance-based engineering.

## 2 Background

The use of the traditional elastic-force-based seismic design procedures for structures obscure a basic understanding of structural performance in terms of levels of damage in a given earthquake. The new NEHRP design guidelines for retrofit of building (ATC 1996, ATC 1997a, 1997b) document alternative nonlinear dynamic response analyses or nonlinear static pushover analyses to better evaluate performance. The simpler nonlinear static pushover procedures modify the traditional approach in several ways. In the case of buildings, the basic demand and capacity parameter for analysis is the lateral displacement of the building.

In a pushover analysis, an increasing monotonic lateral load is applied to the structural model, which includes inelastic load deformation behavior of structural components. The generation of a structural capacity curve (Fig. 2.1) defines the capacity of the building uniquely for an assumed force distribution and displacement pattern. If a building is displaced laterally, its response must lie at a point on this curve. A point on the curve defines a specific damage state for the structure, since the deformation of all of its components can be related to the global displacement of the structure. By correlating this capacity curve to the seismic demand generated by the inertial structural response to a specific earthquake or ground shaking intensity, a point can be found on the capacity curve that estimates the maximum displacement of the building that the earthquake will cause. This is called a “performance point” or “target displacement.” As a first approximation, the displacement corresponding to the elastic earthquake response of the structure may be assumed. The location of the performance point relative to the performance levels defined by the capacity curve indicates whether the performance objective is met. A similar philosophy also applies to the seismic design of bridge structures.

In considering structural behavior, the nonlinear load-deformation behavior of structural components (columns, wall elements, beams, etc.) is defined, and a global model of the

structure is developed to relate total seismic force on a structure to lateral displacement and hence performance or capacity curves. Clearly, in adopting a performance-based nonlinear design approach, the load-deformation characteristics of foundation elements can also play a significant role, particularly in reducing the costs of seismic retrofit. The modeling of nonlinear load-deformation and capacity characteristics of foundation elements and their role and impact on the seismic retrofit of building and bridge structures are central to the theme of this report. Two aspects of foundation nonlinear behavior are of particular significance:

1. The nonlinear load-deformation and capacity characteristics of foundations, and related modeling approaches.
2. The mobilization of the load capacity of foundations to reduce ductility or displacement demands on structural elements and foundation retrofit costs.

The modeling and analysis concepts described below, assume that shallow foundations are founded on competent soils not subject to stiffness or strength degradation under earthquake loading. Soils not subject to either type of degradation will continue to mobilize loads but with increasing deformations after reaching the ultimate capacity. The amount of acceptable deformations for foundations in such soils depends primarily on the effect of the deformation on the structure, which in turn depends on the desired structural performance level. However, it should be recognized that foundation yield associated with mobilization of the ultimate capacity during earthquake loading may be accompanied by progressive permanent foundation settlement during continued cyclic loading. In many cases (depending on initial static factors of safety) this settlement would probably be less than a few inches. In general, if the real loads transmitted to the foundation during earthquake loading do not exceed ultimate soil capacities, it may be assumed that foundation deformations will be relatively small.

One of the major changes in traditional seismic design procedures in the ATC (1990) and ATC (1997a, 1997b) NEHRP building retrofit guidelines is the direct inclusion of geotechnical and foundation material properties in the analysis procedures. In order to accomplish this improvement, the engineer must quantify foundation capacity, stiffness, and displacement characteristics. As discussed by Martin and Lam (2000), the concept of allowing mobilization of the ultimate capacity of shallow foundations during earthquakes represents a major change in conventional foundation design philosophy for static loading but may result in reduced ductility demands on the structure and provide for more reliable

performance evaluations. The related problems of model development and predictions of earthquake-induced permanent foundation displacement provide an analytical challenge to geotechnical engineers, and are discussed further below.

Similar concepts of permitting shallow foundation capacity mobilization and the related problem of settlement determination are being considered and researched in relation to new developments for the Eurocode, as described by Pecker and Pender (2000) and Faccioli et al. (2001).

## **2.1 NONLINEAR STIFFNESS AND CAPACITY MODEL CONCEPTS**

The objective of the force-displacement relationships for foundations is to allow the structural engineer to incorporate the foundation characteristics into an earthquake response analysis model. Consider the spread footing shown in Figure 2.2 with an applied vertical load ( $P$ ), lateral load ( $H$ ), and moment ( $M$ ). The soil characteristics are often modeled as uncoupled translational springs and a rotational spring, each characterized by a linear elastic stiffness and a plastic capacity. More common, however, is the use of a Winkler spring model acting in conjunction with the foundation structure to eliminate the rotational spring, as shown in Figure 2.3. Also the Winkler model can capture more accurately the progressive mobilization of plastic capacity during rotational rocking behavior, as discussed below. Note that the lateral action is normally uncoupled from the vertical and rotational action. The conversion to Winkler springs, however, may require consideration that rotational stiffness could differ substantially from vertical stiffness.

While it is recognized that the load-deformation behavior of foundations is nonlinear, because of the difficulties in determining soil properties and static foundation loads for existing buildings, together with the likely variability of soils supporting foundations, an upper- and lower-bound approach to defining stiffness and capacity of foundations is often suggested (as shown in Fig. 2.4) to permit evaluation of structural response sensitivity. This approach has been adopted in the NEHRP building retrofit guidelines. An uncoupled elastic-plastic stiffness representation is the simplest to use analytically. However, more refined coupled or uncoupled nonlinear models can be utilized if the availability of soil properties and analysis methods and the importance of the project warrant their use.

Many foundation systems are relatively stiff and strong in the horizontal direction, due to passive resistance on the sides of footings or basement walls, and friction beneath footings and floor slabs. Comparisons of horizontal stiffness of the foundation and the structure can provide guidance on the need to include horizontal foundation stiffness in demand or capacity analyses. In general, foundation rocking has the most influence on structural response. Slender shear wall structures founded on strip footings, in particular, are most sensitive of the effects of foundation rocking. In combining structural and foundation elements in a global system model, various assumptions may be made by structural engineers, as illustrated in Figure 2.5, for a simple combined shear wall and frame structure. In some cases, grade beams or slabs may provide strong horizontal linkage of footings, providing additional axial or rotational linkage.

Assuming that shallow footing foundations may be represented by an embedded rigid plate in an elastic halfspace, classical elastic solutions may be used to compute the uncoupled elastic stiffness parameters illustrated in Figure 2.2. Solutions developed by Gazetas (1991) are often used, as described in ATC (1996).

One of the difficulties in using the elastic solutions is the appropriate choice of an equivalent linear shear modulus, due to the dependence of shear modulus on cyclic shear strain amplitudes. To overcome this difficulty, the ATC retrofit guidelines use values based on average shear wave velocities in foundation soils, empirically reduced by factors that are a function of peak design ground accelerations. Although such uncertainty is reflected in an upper- and lower-bound approach, estimates of ultimate foundation capacity are often more significant in controlling earthquake-induced displacements, where full foundation capacity is mobilized.

## **2.2 MOMENT-ROTATION CAPACITY CONCEPTS**

The effects of yield, rocking, and uplift of rigid footings under earthquake-induced moment loading on potential reductions in ductility demand of buildings was recognized and discussed by Taylor and Williams (1979) and Taylor et al. (1981). The concept was introduced that rotational yield could be allowed to occur under earthquake loading without serious detriment to vertical load-bearing capacity, and that under suitable conditions, induced vertical settlements could be small. It was further postulated that footing yield may

be a preferable mechanism for dissipating energy than yield of columns at base level. The importance of modeling rocking of shear wall foundations as a means of energy dissipation has also been discussed by Pauley and Priestley (1992), who acknowledge that the satisfactory response of some structures in earthquakes can be attributed only to foundation rocking. The importance of modeling rocking for bridge piers on footings or for single-column bridge bents is discussed by Priestley, Seible, and Calvi (1996).

The concept of allowing footing yield and uplift of footings has been introduced into the NEHRP guidelines for the retrofit of buildings (ATC 1997a, 1997b). The concept is illustrated in Figure 2.6, where a footing foundation is envisaged as supported by a series of elastic Winkler springs, each having a load capacity of  $q_c$  / unit area.

In the absence of moment loading, the vertical load capacity of a rectangular footing of width  $B$  and length  $L$  is:

$$Q_c = q_c BL \quad (2.1)$$

This assumes that  $q_c$  is constant over the footing area, which is a reasonable assumption for a cohesive soil. For rigid footings subject to moment and vertical load, contact stresses become concentrated at footing edges, particularly as uplift occurs. The ultimate moment capacity,  $M_c$ , is dependent upon the ratio of the vertical load stress,  $q$ , to the assumed constant vertical stress capacity,  $q_c$ . Assuming that contact stresses are proportional to vertical displacement and remain elastic up to the vertical stress capacity,  $q_c$ , it can be shown that uplift will occur prior to plastic yielding of the soil when  $q/q_c$  is less than 0.5, (that is, the factor of safety  $F_v$  is greater than 2). If  $q/q_c$  is greater than 0.5 ( $F_v$  is less than 2), then the soil at the toe will yield prior to uplift. In general the moment capacity of a rectangular footing may be expressed as:

$$M_c = \frac{LP}{2} \left( 1 - \frac{q}{q_c} \right) \quad (2.2)$$

$$= \frac{LP}{2} \left( 1 - \frac{1}{F_v} \right) \quad (2.3)$$

where  $P$  is the vertical load,  $q$  is  $\frac{P}{BL}$ ,  $B$  is the footing width, and  $L$  is the footing length in direction of bending.

The nonlinear moment-rotation behavior generated by yield and uplift corresponding to this model is discussed in detail by Bartlett (1976), and is illustrated graphically in the shear wall example described below.

### 2.3 ROCKING BEHAVIOR OF SHEAR WALLS

One of the most frequently encountered problems in seismic rehabilitation is the analysis of a shear wall or braced frame supported upon spread footings. The relationship of the vertical load, overturning moments, and soil properties, and their effect on stiffness and energy dissipation is discussed by Bartlett (1976). The following discussion and illustrative example of the effects of earthquake-induced rocking response of shear walls, is extracted from Comartin et al. (1994) and the NEHRP *Guidelines* (ATC 1997b).

Figure 2.7 illustrates the general relationship between overturning moment and base rotation for a wall that is allowed to uplift and/or accommodate compression yielding in the supporting soil medium. This rocking behavior has several important consequences on the seismic response of the structure. First of all, rocking results in a decrease in stiffness and lengthening of the fundamental period of the structure. This effect is amplitude dependent and therefore highly nonlinear. The result is generally a reduction in the maximum seismic response as previously noted. Depending on the ratio of initial bearing pressure to the ultimate capacity of the soil, significant amounts of energy may be dissipated by soil yielding. This behavior can also result in increased displacement response of the superstructure and permanent foundation displacements.

The illustrative example below, demonstrates through an analysis the effects of foundation uplift and soil yielding on the inelastic response of a relatively tall concrete shear wall acting in conjunction with a concrete frame (Fig. 2.8). The building is an existing eight-story structure founded on spread footings. The underlying soils materials are late Pleistocene alluvial and terrace deposits consisting of stiff to very stiff clay and sandy clay, and dense gravelly silty sand strata. A preliminary linear analysis indicated extremely high bearing pressures beneath the shear wall due to seismically induced overturning moments.

The nonlinear model of the structure included springs representing the stiffness and strength of the soil beneath the shear wall, and led to the foundation stiffness and capacity curves shown in Figure 2.9. These springs were preloaded with the effect of vertical loads from the structure but uplift was allowed if the preload was overcome by rotation. A lateral load, distributed vertically in accordance with that predicted by the elastic model, is applied in steps. This technique is essentially that of a static pushover test. The damage state of the structure was evaluated from the capacity spectrum at incremental levels of lateral deformation.

Rocking and compressional soil yielding initiate early in the response of the structure. In fact it was found that over two-thirds of the deformation demand of the design response spectrum was absorbed in the foundation soils materials. As a consequence, the inelastic demand on the shear walls was very small and within acceptable limits for life-safety performance goals for the structure as a whole. The stiffness and strength of the soil were varied by factors of 67% and 150% in an effort to test the sensitivity of the analysis results to these parameters. The behavior was not significantly affected, leading to the conclusion that the response is most sensitive to nonlinear rocking itself rather than exact soil properties.

These results have strikingly different implications on a structural rehabilitation strategy than does the linear analysis. The foundation rocking effectively protects the shear walls from large inelastic demand. Modification to the walls and their foundations is not necessary. However, the resulting large lateral movement of the structure could cause undesirable shear failure in some of the columns of the concrete frame. This leads to the conclusion that the columns should be retrofitted to provide greater shear strength by jacketing or other techniques to provide increased confinement. In contrast, the linear analysis might indicate that a relatively expensive retrofit of the walls and footings is warranted. Perhaps more significantly, the linear analysis masks the potential problem with the columns.

The rocking behavior of shear walls and its influence on structural response is the focal point of current PEER experimental and analytical research on shallow foundation behavior as described in Sections 3, 4, and 5 of the report. Related experimental studies, theoretical simulations, and interface model development conducted in the past by others are discussed further below.

## **2.4 EVALUATION OF DEFORMATIONS AND SETTLEMENT DUE TO MOMENT YIELD AND MODEL CONCEPTS**

In allowing plastic yield of footings during earthquake-induced cyclic loading, the question of the magnitude of accumulated settlement induced by the static vertical load is clearly of design concern. This question and the desire to validate the simple nonlinear model previously described led to a series of 1g models based on yielding Winkler spring assumptions, and footing tests on both sands and clays at the University of Auckland, New Zealand, which are documented by Bartlett (1976), Wiessing (1979), and Taylor et al., (1981). While it is difficult to extrapolate such model tests to prototype field conditions, the test results generally were consistent with the simple theory in terms of moment-rotation behavior, as summarized below. Also, where static factors of safety were greater than three, test results suggested that induced settlements could be tolerable, say, of less than a few inches. Clearly, results are very dependent on the magnitude of design earthquake and do not include additional contributions to settlement (particularly in the case of sands) that may arise from earthquake wave propagation in underlying soils. That is, analyses assume that settlement is primarily due to inertial loads on foundations from structural response.

Similar large-scale 1g and tests and related modeling studies have been conducted in Italy in an attempt to address the question of moment-rotation behavior and settlement in greater depth, and are described by Faccioli et al. (2001). Presently available finite element or finite difference computer codes coupled with appropriate nonlinear soil constitutive models provide the means for examining the problem in greater detail and provide the means for simplification to equivalent uncoupled or coupled “spring” footing interface models for structural codes. Existing experimental data and theoretical models are summarized in the section following. The experimental databases provide a valuable resource for examining theoretical models suitable for linking with structural response computer codes.

### **2.4.1 Experimental Studies**

#### ***2.4.1.1 One-g Model Tests***

One-g model experiments on spread footing rocking conducted at the University of Auckland, New Zealand, are described by Taylor et al. (1981). The soil container was 1.3 m

square and 0.6m deep. The footing size was 0.50 m × 0.25 m. Two types of footings were used: the first with the central rocking axis parallel to the long side of the footing (Type B). The vertical load was applied by transferring lead weights with hanger rods passing through holes in the concrete floor. To apply cyclic rocking displacement, a vertical frame was fixed to the footing and was moved by a loading arm attached to its upper end. This arm was connected to an adjustable crank on the drive unit mounted on the reaction wall. Harmonic rocking motion of adjustable amplitude was applied to the footing at a frequency of 0.5 Hz. The instrumentation system consists of a load cell in the loading arm to determine the applied moment, and two displacement transducers (LVDTs), one at each end of the footing to measure vertical displacements. Figure 2.10 shows a photograph of the test apparatus. Representative results on a saturated clay (49 kpa shear strength) for initial static factors of safety of 1.5 and 3.0 are shown in Figure 2.11. As expected the accumulated settlements associated with soil yield, were larger for the lower factor of safety. In all cases where static factors of safety were greater than 3, the test results suggested that settlements could be tolerable, say, of less than a few inches.

Similar large-scale 1g cyclic loading experiments have been conducted in Italy as part of the European Project TRISEE (3D Site Effects and Soil-Foundation Interaction in Earthquake and Vibration Risk Evaluation) and are described by Faccioli et al. (2001). A sketch of the experimental equipment is shown in Figure 2.12. Foundations were 1 m × 1 m and were tested under cyclic moments for dense (85% R.D.) and loose (45% R.D.) sand soil conditions. Representative test results are shown in Figure 2.13.

#### ***2.4.1.2 Centrifuge Model Tests***

The above model tests were conducted in soil tanks under 1g loading conditions. However such model tests have similitude limitations when conducted at small scales or have difficulty in achieving yield conditions at lower factors of safety when conducted at near full scale due to load constraints. The use of centrifuge models overcomes these constraints. Zeng and Steedman (1998) and Garnier and Pecker (1999) describe successful centrifuge tests on model footings subjected to seismic loading conditions. The use of centrifuge model tests to study the influence of rocking and soil yield under moment loading on the behavior of shear walls forms part of the PEER research program described in Chapter 3.

## 2.4.2 Theoretical Simulation Using FLAC

A finite difference computer model suitable for studying the problem of the nonlinear moment-rotation behavior of footings has been presented by Yan and Martin (1999). The model utilizes the computer program FLAC (ITASCA 1995) and a multiple yield surface nonlinear constitutive model capable of simulating cyclic loading behavior. The laboratory tests results described by Taylor et al. (1981) were used as a check on the model performance. Typical analysis results for the rotation controlled cyclic moment tests of varying amplitude are shown in Figures 2.14 and 2.15, for a model footing (0.5x0.2m) on clay soil (shear strength 45 kPa). Results for  $F_v = 1.5$  and 3.0 were in general agreement with laboratory test data. Footing uplift is clearly evident for the case where  $F_v = 3$ .

## 2.4.3 Nonlinear Interface Models for Structural Computer Codes

Finite element or FLAC-type modeling as described above provide valuable approaches to understand the mechanics of yielding and rocking under moment loading. However, for analyses of the seismic response of structures to include footing interaction, the use of interface elements able to replicate the behavior demonstrated by physical experiments or theoretical finite element models, are more useful for practical applications.

A nonlinear gapping interface element suitable for such applications is described by Martin, Yan, and Lam (1997) and Lam (2000). Figure 2.16 shows the concept behind the so-called spring element originally developed to simulate nonlinear hysteretic and potential gapping behavior of pile footings. The element comprises a set of elasto-perfectly-plastic subelements in parallel. The basic algorithm in the spring element allows the flexibility to represent any form of nonlinear hysteretic and potential gapping behavior of pile footings. The element comprises a set of elasto-perfectly-plastic subelements in parallel. The basic algorithm in the spring element allows the flexibility to represent any form of nonlinear strain hardening backbone curve, including the ability to capture unsymmetric curve shapes. A variety of gapping elements are also available, enabling capture of the uplift behavior.

The application of the spring element to study the influence of nonlinear and gapping behavior of bridge abutments on the seismic response of bridges has been described by Martin et al. (1997). More recently, the spring element has been implemented in the DRAIN

3DX structures analysis program by Fenves (1992) to study the influence of nonlinear moment response of piled bridge footings on the ductility demands on bridge columns. The results of quasi-static cyclic loading analyses on such footings conducted for these analyses are shown in Figures 2.17–2.19. It is of interest to note that the results of sensitivity studies showed that settlements would be less than a few inches if initial factors of safety were greater than 2 to 3, as was the case for footing tests described by Taylor et al. (1981).

For studying the behavior of footings under moment loading, individual Winkler springs would be represented by spring elements, with the nonlinear gapping elements in the model being appropriately chosen to simulate conditions representative of results from experimental model tests, or FLAC or finite element analyses.

As discussed by Faccioli et al. (2001), an alternative and promising interface model to capture coupled nonlinear response of a soil–shallow foundation system and a superstructure, including the ability to capture permanent displacements, was developed by Paolucci (1997). In this model, the material or geometrical (uplift) nonlinearities occurring at the soil–foundation interface are concentrated in three elements (horizontal, vertical, and rocking displacements) described by elasto-plastic constitutive laws as shown in Figure 2.20. In the elastic range, spring and dashpot coefficients are calculated from standard formulas (e.g., Gazetas 1991). When the yield surface is reached, perfectly plastic flow (no hardening) with a nonassociated flow rule is assumed. This model has recently been further refined by Cremer et al. (1999) to account for foundation uplift.

## **2.5 SUMMARY**

Representation of shallow foundation stiffness by elastic parameters has been the past focus of attention for shallow foundation soil–foundation–structure interaction analyses, and is the approach most cited in existing seismic design codes or guidelines. Such an approach is designed to primarily examine the effect of period shift on force demands. However, for performance-based design of structures, a significant design issue is that of the influence of capacity mobilization of shallow foundations under structural inertial loading, particularly under rocking modes.

The forces induced in buildings or bridges by the response to earthquake ground motion are limited by the stiffness and capacity of foundation systems. In the case of

shallow footings, rocking or uplift provides limiting mechanisms and a source of energy dissipation, and hence use of traditional elastic force-based analysis, can lead to unrealistically high foundation forces. Retrofit to avoid exceeding moment capacity may transfer energy-dissipating mechanisms to the structure and could lead to excessive retrofit cost.

New retrofit guidelines in the United States document nonlinear analysis methods, where displacements are used as a measure of performance. These methods require engineers to establish nonlinear load-deformation characteristics of foundations and allow mobilization of the ultimate capacity during earthquake loading, albeit the effects of induced progressive settlement need to be considered. Studies to date of moment-rotation relationships for rigid footings (assuming elastic-plastic Winkler spring support) show the following general trends:

1. If the static factor of safety is greater than 2, the footing separates from the soil (uplift) before yield occurs on the compression side. If the factor of safety is less than 2, the soil yields plastically before uplift occurs.
2. For factors of safety of 3 or less, computer simulations show good agreement with model experimental results. For factors of safety of less than 2, large hysteretic loops able to dissipate considerable energy are generated, albeit significant settlement may result.
3. For factors of safety greater than 2–3, tests and theoretical results suggest that settlements may be tolerable.
4. Analytical studies to date incorporating the nonlinear- and capacity-related moment and rocking behavior of footings in structural response analyses have shown potential benefits to structural ductility demands.

To reinforce the performance-based deformation approach being adopted in seismic design codes, it is clear that an improved understanding of the nonlinear and capacity deformation behavior of shallow footings is needed, particularly for retrofit analyses. Both new experimental data and modeling approaches are required to enable practical design approaches to be developed with some degree of confidence. This critical need has also been identified by researchers in Europe, responsible for the development of the Eurocode.

To address the above needs, the PEER research plan is focusing on

1. The influence of nonlinear deformation and moment capacity on the rocking behavior of shallow footings supporting shear walls.

2. The development of an experimental database for both sands and clay foundation soils using centrifuge testing at UC Davis to simulate earthquake loading on shear wall structures supported by strip footings.
3. The development and integration of nonlinear Winkler-type spring models (as an interface foundation model) into the PEER structural analysis program OpenSees, and subsequent verification using the centrifuge test results. (UC Irvine research project)
4. The development of a single-element “macro-model” as an alternative interface modeling method. (UC Davis research project)
5. The evaluation of structural response parametric analyses using the above models to determine the effects of nonlinear response on structural ductility demands.

Development progress is described in the report Chapters 3, 4, and 5.

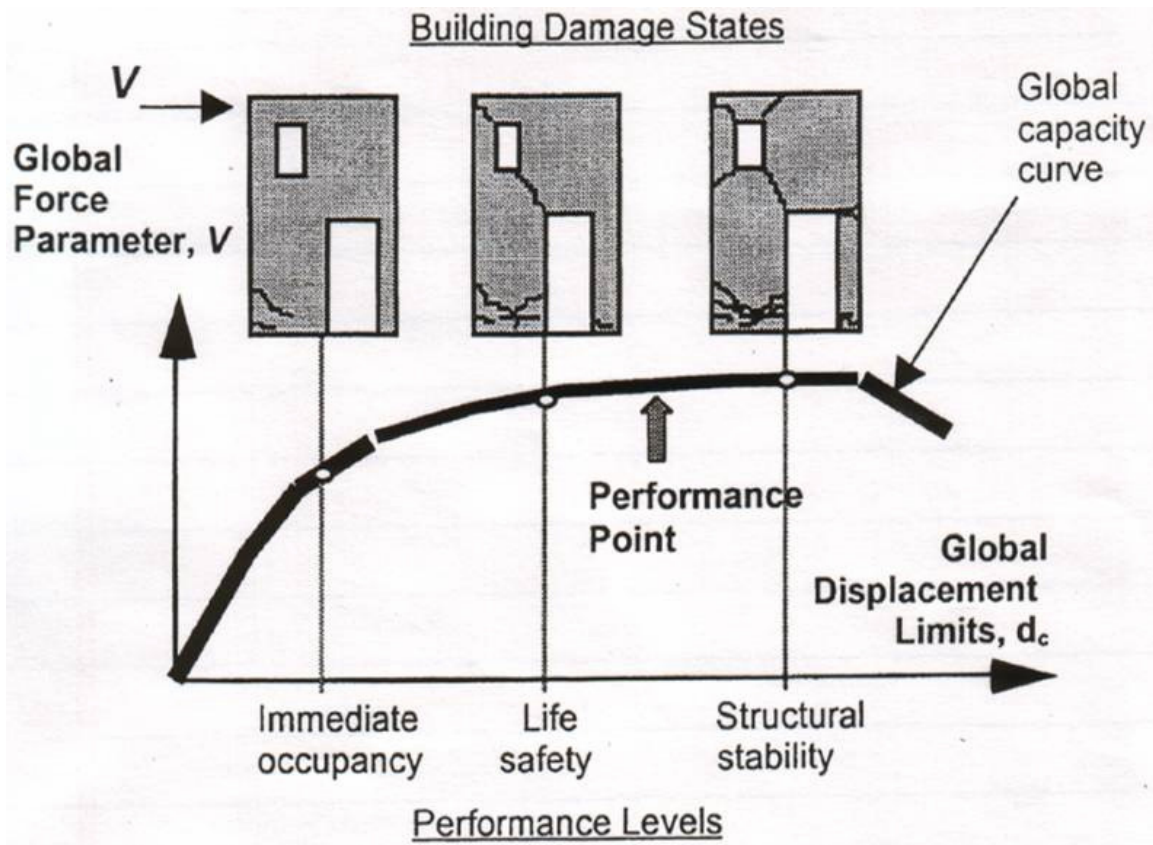


Fig. 2.1 Building capacity and global displacement capacities for various performance levels (after Shapiro et al., 2000)

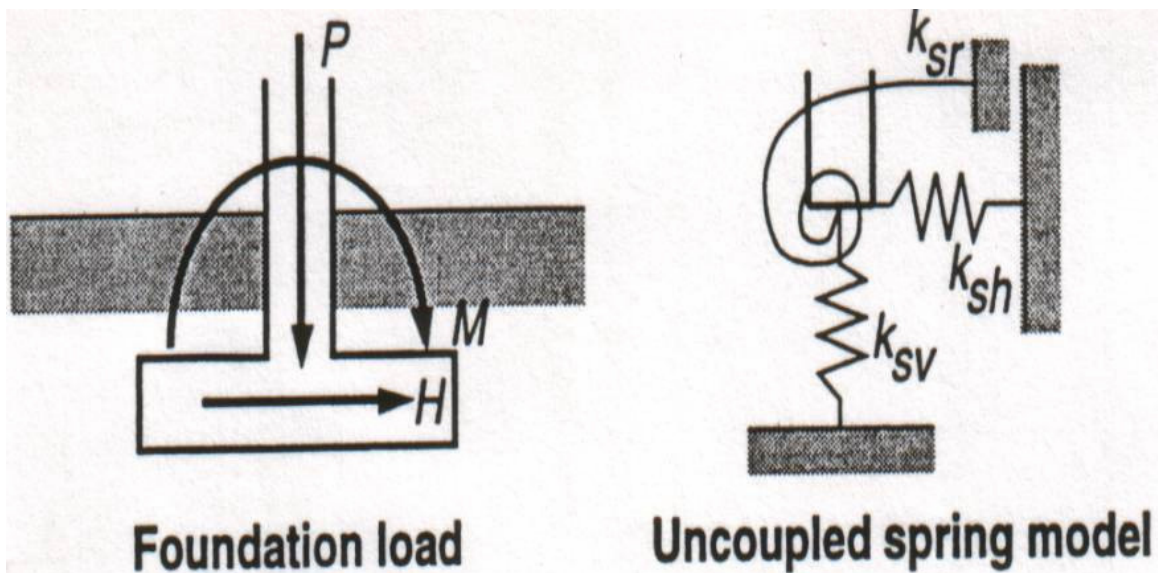
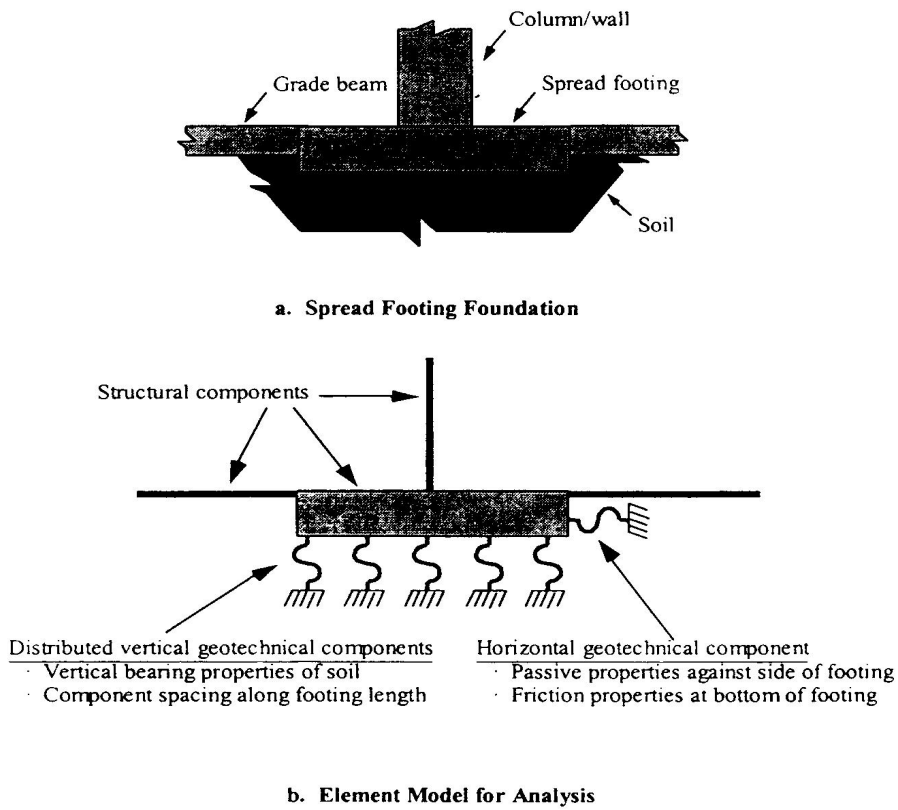
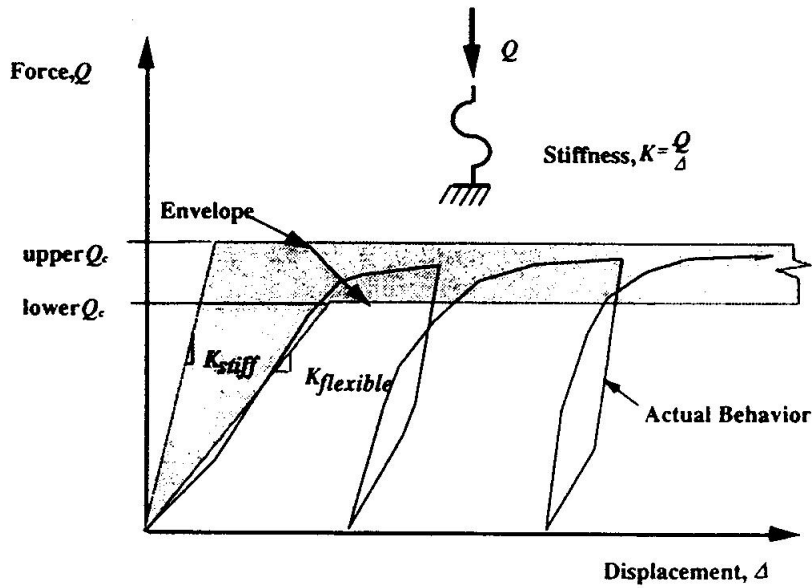


Fig. 2.2 Uncoupled elasto-plastic spring model for rigid footings



**Fig. 2.3 Shallow foundation model (ATC 1996)**



**Fig. 2.4 Basic force-displacement envelope for geotechnical components (ATC 1996)**

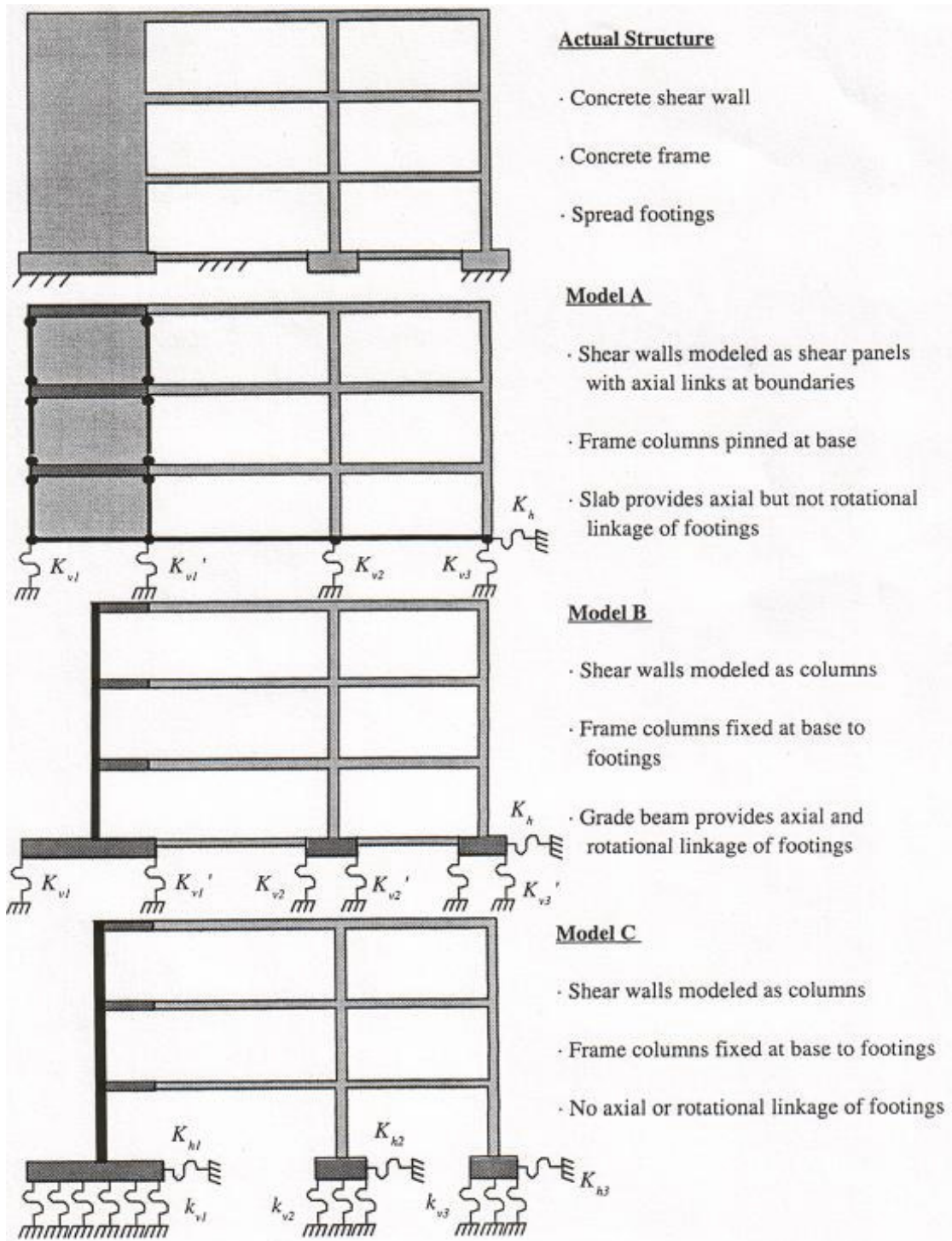
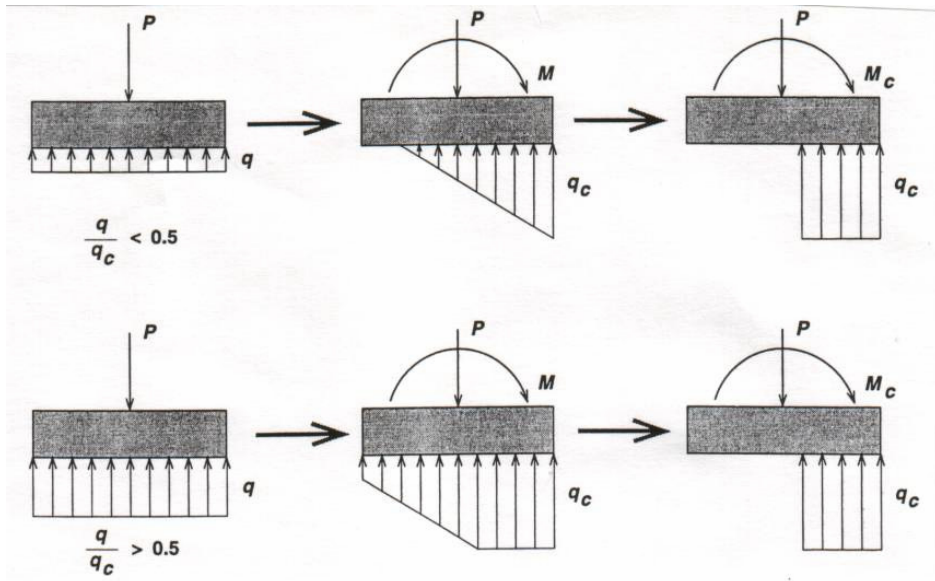
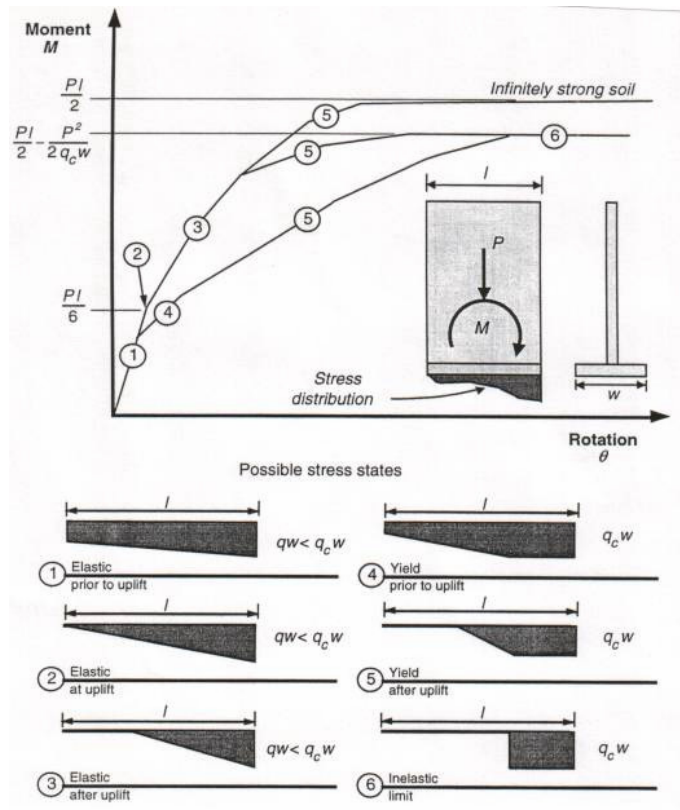


Fig. 2.5 Global and foundation modeling alternatives (after ATC, 1996)



**Fig. 2.6 Idealized concentration of stress at edge of rigid footings subjected to overturning moment (after ATC, 1997a)**



**Fig. 2.7 Rocking of shear wall on strip footing (after ATC, 1997b)**

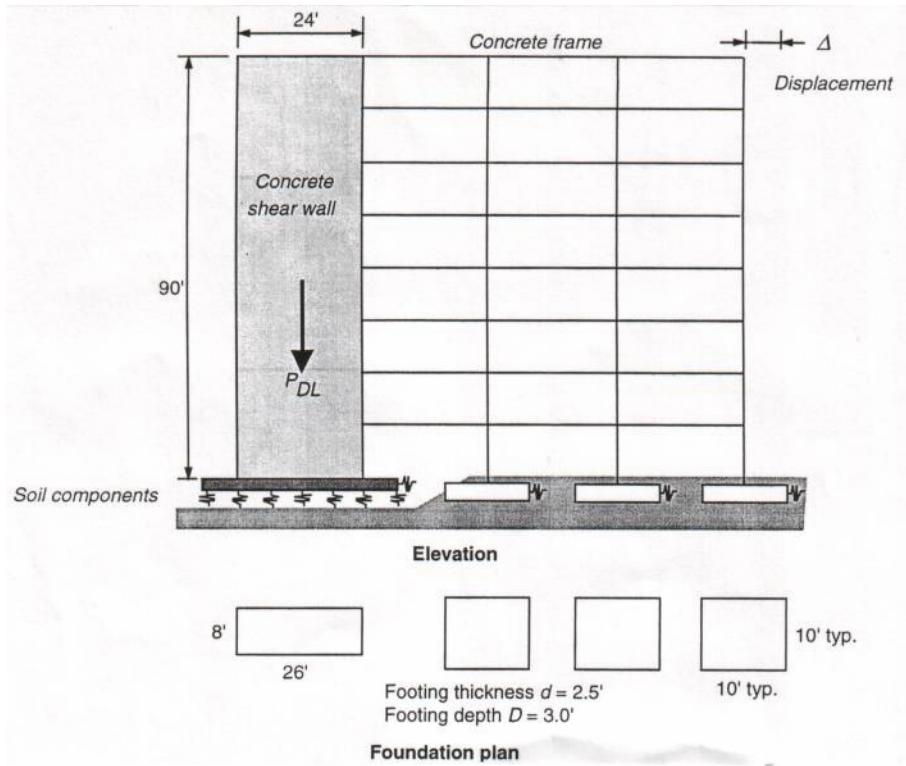


Fig. 2.8 Shear wall and frame example (after ATC, 1997b)

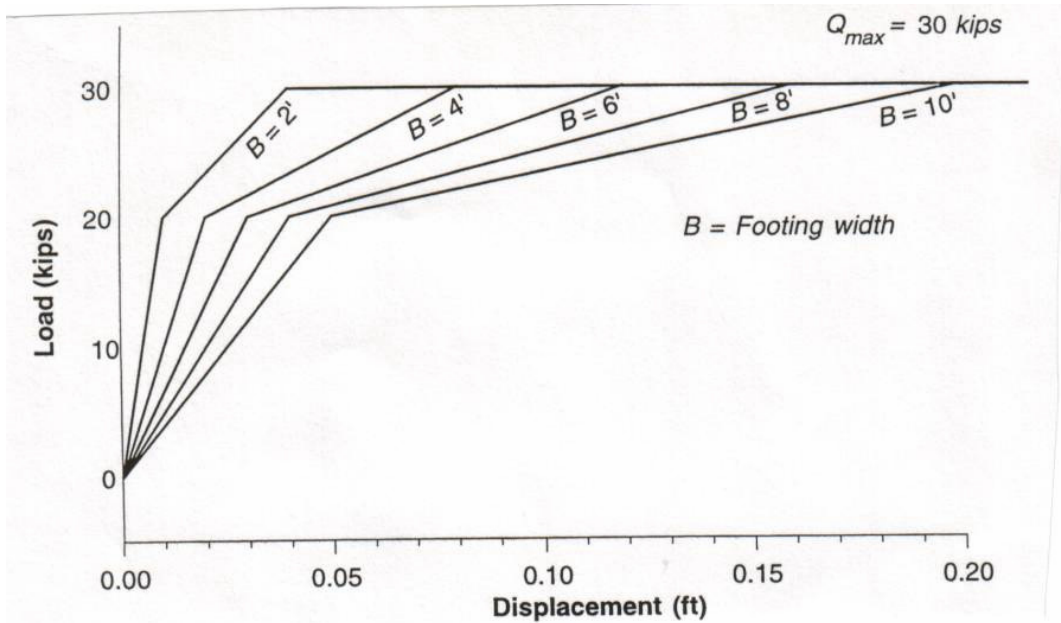
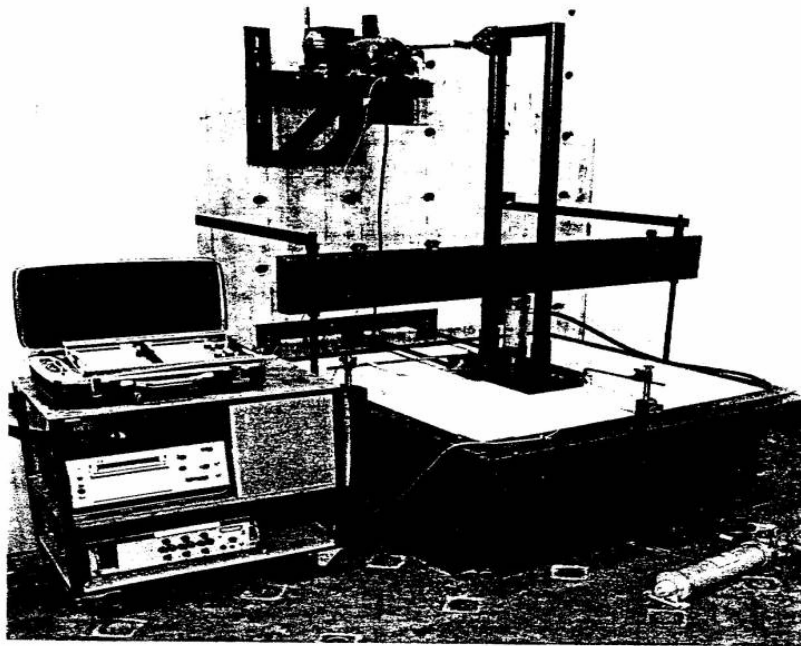
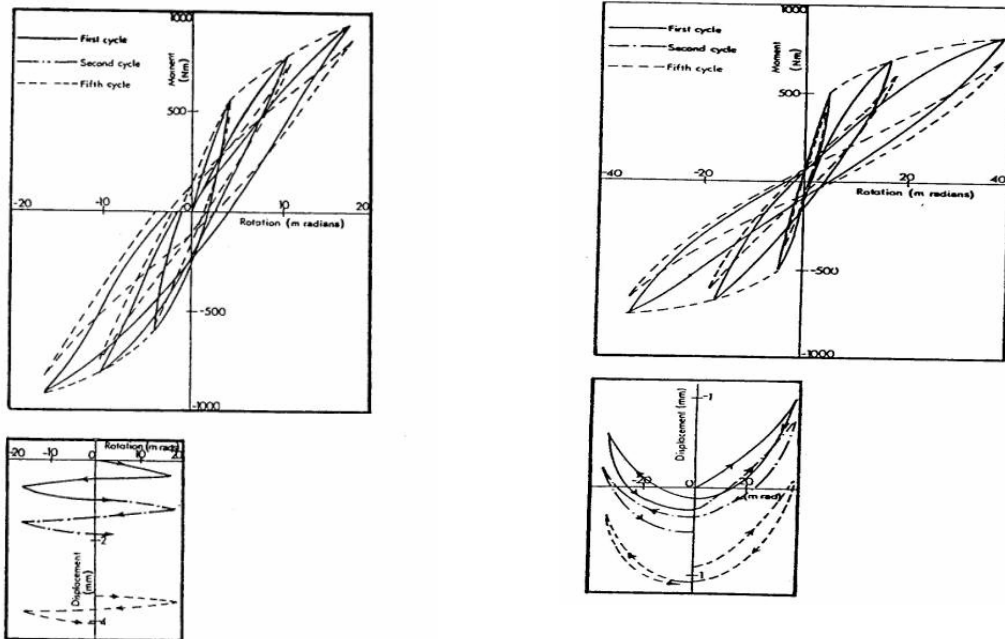


Fig. 2.9 Foundation stiffness and capacity of footing (after ATC, 1997b)



**Fig. 2.10** Experimental apparatus: The motor unit attached to the wall at the top of the picture rocks the footing via the vertical frame



Measured behavior of Type B footing on clay:  
experimental result for  $F_v = 1.5$

Measured behavior of Type B footing on clay:  
experimental result for  $F_v = 3.0$

**Fig. 2.11** Representative results from the University of Auckland Tests (after Taylor et al., 1981)

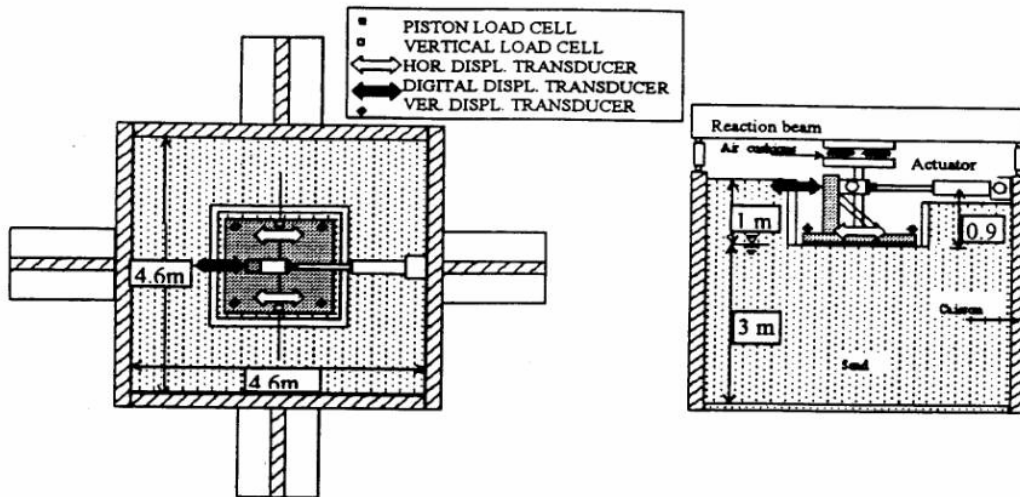
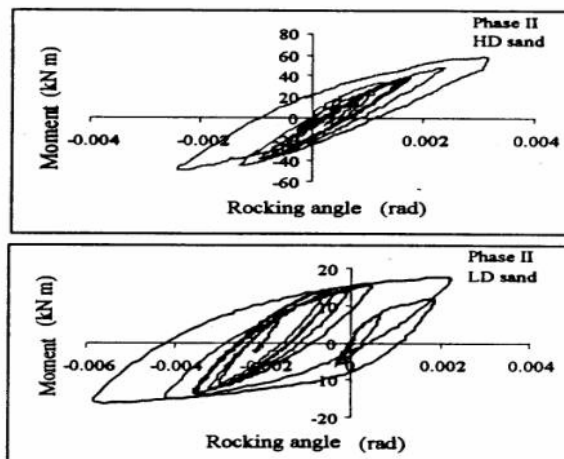
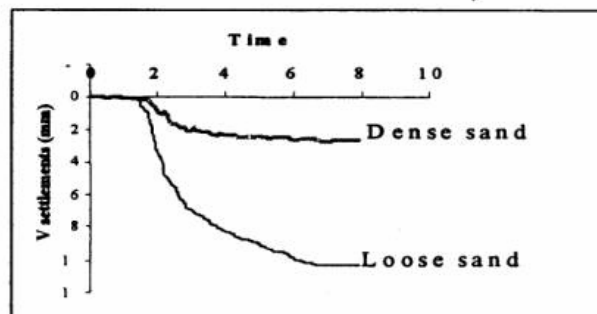


Fig. 2.12 Scheme of the experimental setup (after Faccioli, 2001)



Phase II: Overturning moment vs. rocking for HD and LD conditions



Phase II: Vertical displacement of the foundation

Fig. 2.13 Representative test results (after Faccioli, 2001)

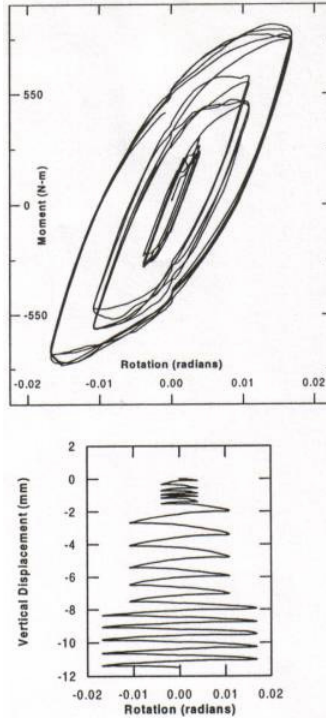


**Fig. 2.14 Simulated behavior of Type B footing on clay:  $F_v = 1.5$**

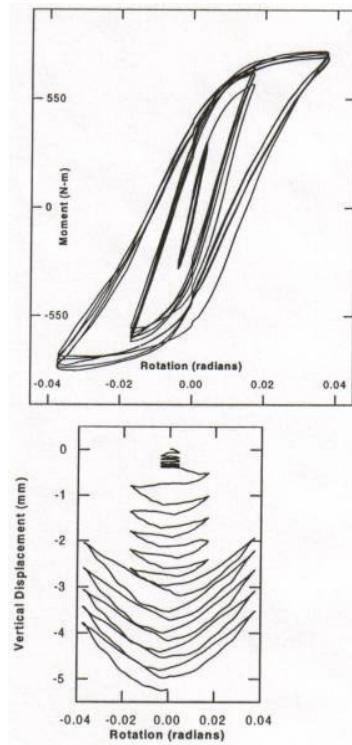


**Fig. 2.15 Simulated behavior of Type B footing on clay:  $F_v = 3.0$**

### 3 Centrifuge Model Tests

Physical modeling of the nonlinear load deformation behavior of shallow foundations has been performed at the UC Davis Center for Geotechnical Modeling (CGM) on the facility's 9.1-m radius centrifuge. The centrifuge spins a container of soil at a high centrifugal acceleration, increasing the gravity level on the model. This effectively increases the self-weight of the model to make the stresses in the model equal to the stresses in the prototype. For example, a 1-m deep layer of sand spinning at an acceleration of 20g, will have the same self-weight stresses as a 20-m deep layer subject to 1g. Since soil strength is dependent on confining stress, the centrifuge is a useful tool to increase the accuracy of geotechnical model tests. Table 3.1 presents scaling laws for selected quantities.  $N = 20$  is the scaling factor used for the majority of tests done here.

Three general types of loading were applied to the models: *dynamic* and *slow cyclic lateral loading*, and *axial loading*.

1. Dynamic events were produced by a 1-D servo-hydraulic shaker table mounted on the centrifuge platform. The actuator can be programmed to apply to the base of the model container various ground motions, such as step waves, controlled tapered cosine waves, and scaled motions recorded from actual earthquake events.
2. Slow cyclic events used a small hydraulic actuator that directly applied packets of sinusoidal displacement (approximately 0.01 Hz cycles) to the shear walls. The actuator applied horizontal loads at different elevations to control the relative amounts of foundation sliding or rotation.
3. For axial load tests, the same actuator was used to apply cyclic or monotonic axial (vertical) loading to the footings.

The test program to date has studied the effects of various parameters on the load-deformation behavior of the footings: factor of safety of the footing, footing embedment, soil density, soil type, and the height of the building.

At the time of this report there are four publications that directly involve the results of the test progression. Three data reports describe the work done by Rosebrook and Kutter (2001a, b, c) for her three centrifuge test series: KRR01, KRR02, and KRR03. They include information on test setups, procedures and preliminary results. Rosebrook's published master's degree thesis was based on the analysis of these tests and the organization of centrifuge test data archives. Two recently completed tests (SSG02 and SSG03) will have accompanying data reports by March 2003.

A standardization of nomenclature used for all test series is described as follows:

s: vertical displacement (settlement)

u: horizontal displacement (sliding)

$\theta$ : rotation

V: vertical load (weight)

H: horizontal load

M: rotational moment

In addition, corresponding to each displacement, rotation, load and moment is its normalized value. Any normalized displacement or rotation is denoted with the letter "U." Any normalized load or moment is denoted with the letter "F." The subscript of the parameter determines its type. For example, the parameter " $F_v$ " is a normalized vertical load (or weight) and " $U_v$ " is a normalized vertical displacement (or settlement). The parameter " $F_M$ " is a normalized applied moment (whether slow cyclic or dynamic) and " $U_M$ " is the corresponding normalized rotation of the building with respect to the bottom center of the footing. Figure 3.1 illustrates these parameters with the schematic of a displaced footing.

$$\begin{aligned}
 U_v &= \frac{s}{L} & U_H &= \frac{u}{L} & U_M &= \theta & & (3.1) \\
 F_v &= \frac{V}{V_{MAX}} & F_H &= \frac{H}{V_{MAX}} & F_M &= \frac{M}{V_{MAX}L} & F_{S_v} &= \frac{V_{MAX}}{V}
 \end{aligned}$$

where L is the length of the footing and  $V_{MAX}$  is the vertical load corresponding to a factor of safety of 1.0.  $V_{MAX}$  is determined by averaging the friction angles back-calculated using a conventional bearing-capacity equation (Section 3.3.1) using results of vertical load tests on

model footings in the centrifuge. The factor of safety with respect to vertical bearing failure is termed “FS<sub>v</sub>.”

### **3.1 SUMMARY OF MODEL TESTS**

#### **3.1.1 Overview**

To date, there have been five series of tests, each uniquely contributing to the overall scope of the project. A series involves one container that houses many individual tests. The majority of tests were conducted on sand foundations. In one series, a clay layer was consolidated on top of a dense sand layer. The footing and shear wall are modeled using either steel or aluminum parts.

#### **3.1.2 Configuration of the Structures**

Walls were tested in either a “double-wall” or “single-wall” configuration. In the first three series of tests (KRR01–KRR03), all buildings were modeled in a double-wall configuration to make a stable self-supporting structure. Two aluminum walls were placed side by side and rigidly attached by an aluminum “floor.” Figure 3.2a shows a schematic of a typical double-wall test. In comparing results from double-wall and single-wall tests in this report, we always report loads and structure masses on a “per footing” basis; if there are two footings, the building mass is divided by two to enable comparison of the building mass per footing. In the double-wall tests during cyclic loading, the structure was observed to accumulate transverse tip (out of the plane of loading); in some tests, at later stages of loading, the tip proceeded until the structure began to rub on the support beams used to measure the displacement of the structures. This introduced friction, which was small but not negligible. Rosebrook (2001) developed a procedure to remove the measured friction from the measured data in tests KRR01–KRR02.

The fourth and fifth series of tests (SSG02-SSG03) utilized a single-wall footing configuration for slow cyclic tests (Fig. 3.2b). Lateral support was provided by Teflon<sup>®</sup> pads to prevent tipping in the transverse direction and to guide the walls in a vertical plane. The single-wall configuration was considered superior because it conserved space in the model container and minimized the frictional resistance due to rubbing on the support beams. Figure 3.3 shows a side view of the model container with typical wall and footing configurations.

### 3.1.3 Soil Properties

KRR01, KRR02, SSG02 and SSG03 all featured sand soil foundations. For each series, the soil foundation was placed by air-pluviating roughly 20 cm of a uniform fine sand (Nevada Sand,  $D_{50} = 0.15$  mm) into a 1.75 m x 0.90 m x 0.53 m rigid container. The relative density,  $D_r$ , of the sand was controlled by the fall height and flow rate of the sand particles. Table 3.2 gives approximate  $D_r$  values for each of the series. The values have some uncertainty because the sand may vary in density at different parts of the container. Sand at the edges of the container may have the tendency to be in a looser state than the sand in the middle of the container because the walls act as obstacles, preventing some particles from free falling from their fully designated height. Kinetic energy may be lost to friction between the sand particles and the wall surface, so compaction may not be as high as intended. The values reported in Table 3.2 are calculated from direct mass and volume measurements of the container and sand. The method was calibrated by pluviating sand from a known height and flow rate into a box with a known volume and mass. The  $D_r$  was calculated based on the void ratio of the pluviated sand relative to the experimental maximum and minimum void ratios of Nevada Sand from Woodward-Clyde (1997). For each series, a friction angle,  $\phi$ , was back-calculated from vertical load tests using the conventional bearing-capacity equation (Eq. 3.4). Along with  $D_r$ , Table 3.2 also reports these friction angles. Figure 3.4 shows the six vertical bearing-capacity tests from KRR01, KRR02, SSG02, and SSG03 and illustrates the method used to determine  $V_{MAX}$  for each.

In test series KRR03 a clay layer was consolidated on top of a dense sand layer. A stratum of Bay Mud was consolidated to a thickness of 8.5 cm (model scale) prior to spinning and saturation of the model was conducted in flight. The undrained strength of the clay,  $c_u$ , was determined in a variety of ways. Rosebrook and Kutter (2001c) made hand Torvane measurements at each station before and after each test over the course of the series. Cored samples were also taken upon completion of the test series and tested for strength in unconfined compression.

Torvane test results varied between about 120 and 75 kPa. Rosebrook states difficulty in administering these tests because of limited access within the model container. Torvane tests should only be considered as a good index, not an accurate measure of shear strength.

The cored samples (all taken after the last test) tested in unconfined compression report very consistent results. All three samples had a maximum vertical stress between 125 and 150

kPa. The undrained strength of the clay is defined as one half of the maximum vertical stress in unconfined compression. In this case  $c_u$  is determined to be about 70 kPa.

Undrained strength can also be estimated with an empirical approach. The Shansep procedure referenced by Ladd (1991) assumes that strength normalizes with consolidation pressure.

$$c_u = \sigma'_{vo} S(OCR)^m \quad (3.2)$$

where  $\sigma'_{vo}$  is the initial effective stress at the center of the clay layer,  $S$  is the normally consolidated value of  $\frac{c_u}{\sigma'_{vo}}$ ,  $OCR$  is the over consolidation ratio of the clay layer  $\frac{\sigma'_p}{\sigma'_{vo}}$ , and  $m$  is the strength increase exponent ( $\approx 0.8$ ).

Assuming that the water table is at the bottom of the 85mm clay layer and  $\gamma = 17 \text{ kN/m}^3$ , and the top sand layer is 13 mm thick with  $\gamma = 16 \text{ kN/m}^3$ , the effective stress varied between 20.8 and 33.1 kPa at the top and bottom of the clay layer.  $S$  was assumed to be 0.3 based on experience with this Bay Mud.  $\sigma'_p$  was taken from the original maximum consolidation in the laboratory = 370 kPa. Using this method,  $c_u$  was determined to be approximately 66 kPa.

From vertical load-bearing-capacity tests performed at the beginning and end of the test series (Stations AW and CE, (Rosebrook and Kutter 2001c)), the ultimate vertical bearing capacity was 577 kPa and 536 kPa. For footing length (2.67 m) and width (0.686 m) the shape factor and bearing-capacity factor for the bearing-capacity equation are taken as 1.05 and 5.14, respectively. The back-calculated values for  $c_u$  are 107 and 99 kPa.

Table 3.3 is a summary of all methods of determining  $c_u$  and the corresponding range of values reported by each. The Torvane values may be unreliable because of the variability. However, they are the only values that are taken at various stages of the test, and they suggest a trend of strength decrease with time. Unconfined compression tests may be inaccurate because of disturbance during sampling and the potential for swelling in the time required to stop the centrifuge and take the core samples. The strength measured in bearing-capacity tests on the centrifuge is expected to be enhanced due to consolidation of the clay under the footing attributed to the weight of the superstructure. The Shansep method was used to estimate shear strength in the free field, away from the footings, and the cored samples were also taken a significant distance from the footings; thus these methods do not include the strength increase

due to consolidation under the building weight. With consideration to all of the above factors, all of the various shear strength measurement results follow a consistent pattern. We recommend that the most accurate method for determining  $c_u$  is from the back-calculation of the vertical load tests. It provides a direct measure of bearing capacity in the 20g environment and includes the effect of consolidation stress of the footing. From this method, then, the recommended strength for analysis of the footings is the average of that measured in the two bearing-capacity tests:  $c_u = 103 \pm 10 kPa$ .

### 3.1.4 Instrumentation and Data Processing

Instrumentation for dynamic events consisted of both accelerometers and linear potentiometers (LPs). Accelerometers were attached both vertically and horizontally (in the direction of shaking) on the shaker manifold, in the sand layer and on the building models themselves. Output readings were double integrated to determine dynamic displacement time histories. LPs directly produced position information, and were used to determine the permanent displacement of the footings. The high-frequency information from the accelerometers was combined with the low-frequency information from the potentiometers to accurately quantify the deformation over the full range of frequencies. A special procedure was also developed to process the displacement data to produce displacement time histories that accounted for large deformations and the movement of the walls relative to the LP supports. Slow cyclic events utilized potentiometers only. Each single wall had two vertical and two horizontal LPs. Three are sufficient to define the motion of the wall as a plane, while the fourth was intended for redundancy. A load cell recorded the applied actuator loads on the walls. Figures 3.5 a–f are various photos taken directly from the SSG02 test series.

### 3.1.5 Summary of All Tests Conducted

Table 3.4 is a comprehensive summary of the tests performed to date. It describes the factors that were varied over the last five series (KRR01, KRR02, KRR03, SSG02, SSG03). Two *Soil Types* were used. Nevada sand is a fine, uniformly graded sand, used for most centrifuge applications. *Soil Strength* provides a strength parameter relevant to the soil type used.  $D_r$  is the relative density of a coarse material.  $C_u$  is the undrained strength of a fine-grained, clayey soil.

*Event Type* describes one of the three tests performed on the specific model: vertical slow cyclic, horizontal slow cyclic, or dynamic. *Static F.S.* is the factor of safety with respect to bearing failure associated with each test. It was determined by taking the ratio of the ultimate vertical load (calculated from the vertical slow cyclic events) to the actual load caused by the mass of the wall. *Footing Area* was varied from small (0.97 m<sup>2</sup>, prototype) to large (4.84 m<sup>2</sup>). *Embedment Depth* is how far below the surface of the soil the bottom of the footing was placed (in prototype units) at the beginning of the test. *Load Height* describes the general elevation of the horizontal actuator load application for slow cyclic events and the center of gravity from the bottom of the footing for dynamic events. “Standard” means that the actuator elevation was approximately 4.5 m (prototype) from the bottom of the footing, and “low” means the actuator load was approximately 1.0 m from the bottom of the footing. *Wall Type* describes the relative weight and configuration of each shear wall. An aluminum wall in a double configuration was used for all of the first three tests. This wall was dubbed “Standard Weight.” In SSG02 and SSG03 a lighter aluminum wall and heavier steel wall were used to vary the factor of safety associated with bearing failure. Some tests involving sand were first treated with WD40 at the surface (prior to testing) to provide a small cohesion to the soil to preserve the footing imprint as the building settled and to prevent the dry cohesionless sand beside the footing from falling underneath the footing. The use of WD40 is indicated in the *Oil or No* column.

### **3.1.6 Time Histories of Input**

Figures 3.6a and 3.6b are example plots of time history input motions and instrument responses for a slow cyclic test and dynamic test, respectively. The majority of slow cyclic tests featured the same frequency content, amplitude progression, and number of sine wave packets. Packets were generally sets of three repeated sine waves at the same amplitude and frequency. The first packet of a particular test was very small in amplitude (on the order of +/- 1 mm, model scale). Proceeding sets doubled in amplitude until a relatively large displacement was reached. Previous tests done by Bartlett (1976) suggest that large yielding rotations that lift the footing from the foundation soil tend to reduce the stiffness of the system. Smaller input motions were repeated after large rotations caused yielding to determine the effect of this phenomenon. Some larger slow cyclic events included a superimposed sine wave input motion. This was achieved by adding a small-amplitude, high-frequency sine wave to a larger-amplitude, smaller-frequency

sine wave. The result was data that illustrated small load-unload stiffness relationships at various points in the large hysteretic stiffness pattern.

For dynamic tests, an input motion was applied to the base of the model container in the form of a tapered cosine wave. Mono-frequency waves started at very small amplitudes and increased with each cycle, subjecting the model to increasingly more intense motion. Events were repeated six or seven times, each with larger input amplitudes than the event before. Horizontal accelerometers, placed at three locations on each wall (top, middle, and bottom), captured the response of the buildings. Figure 3.6b shows the time history of the horizontal base, soil, and structure accelerations for one dynamic test. It also shows the building moment time history.

### **3.2 DATA REPORTS**

Data reports for each test series can be found on the CGM website <http://cgm.engineering.ucdavis.edu/research/projects/krr/>. The reports include a detailed description of the test setup and instrumentation specific for each series; output data file names associated with each test; example MathCAD worksheets used to process, filter, smooth, and convert model data into useful prototype units; and plots of processed data. Plots include relations between moment-rotation, settlement-rotation, and acceleration time histories for each test.

Data were collected from instruments at a sampling frequency appropriate for each test (approximately 10 Hz for slow cyclic and 2000 Hz for dynamic events). Each sampled value was recorded, in volts, to a data file where a column was reserved for each instrument. Associated with each test was an instrument channel gain and location list, which provides information about the relative location of each instrument on the structure and calibration specifics. These lists were used to convert the raw output files into scaled prototype engineering dimensions of displacement, load, and acceleration. Once converted, data were filtered or smoothed to eliminate any undesired high-frequency noise. All plotted relationships of moment, rotation, shear force, sliding displacement, and settlement were associated with the center point of the bottom of each footing. Displacement data of three LPs were needed to relate the instrument locations to the center of the footing using geometric relations. Applied moments were calculated as the product of the horizontal load on the building and the perpendicular

distance between the footing bottom and the applied load plus a correction for the p- $\Delta$  effect (the creation of an additional moment caused by the rotation of a building and therefore an eccentric center of gravity). The load for slow cyclic tests was applied at the contact point of the actuator and the shear wall. The applied moment,  $M$ , for dynamic tests was computed by:

$$\mathbf{M} = \mathbf{I}\boldsymbol{\alpha} + m \mathbf{a}_{cg} h_{cg} + m \mathbf{g} \Delta \quad (3.3)$$

where  $\mathbf{I}$  is the structure's moment of inertia about its center of gravity,  $\boldsymbol{\alpha}$  is the angular acceleration of the structure,  $m$  is the mass of the structure,  $\mathbf{a}_{cg}$  is the horizontal acceleration at the center of gravity, and  $h_{cg}$  is the height of the center of gravity relative to the bottom of the structure footing. The term " $m \mathbf{g} \Delta$ " corrects for the p- $\Delta$  effect.  $\mathbf{g}$  is the vertical centrifugal acceleration and  $\Delta$  is the horizontal eccentricity of the center of gravity, relative to the bottom center of the footing.

Included in this report are sample plots of moment-rotation, settlement-rotation, shear force-sliding and sliding-rotation for different parameters that were varied in the experiments, such as FS, embedment, height of push, footing length, and static/dynamic (Figs. 3.7a–i). Figure 3.7a shows the results for test SSG02\_test# 3a, which is a surface footing with a factor of safety of about 6.7, laterally loaded at a height of 4.9m from the base of the footing (standard height). Figures 3.7b–c show the results of another test, which is similar to the one shown in Figure 3.7a except the loading height. The later tests were loaded at a lower height (about 1.16m from the base). Comparison of Figures 3.7a and Figures 3.7d–3.7e shows the effect of the factor of safety on the behavior of footing (FS = 6.7 and FS = 3.3). Figures 3.7f–g show the results of an embedded footing test, which was subjected to standard height lateral push (with a higher factor of safety, FS = 8.4, due to embedment,  $d = 0.7\text{m}$ ). The effect of embedment can be seen by comparing Figure 3.7a and Figures 3.7f–g. Figure 3.7h shows the results for a dynamic test, which includes three tapered cosine wave shaking events (SSG03\_test# 8c, d and e). This is an embedded double-wall-type test, but all the results shown in the plot are "per footing values." Time histories of settlement, rotation, and lateral sliding at the base of the footing during the shaking events are shown in Figure 3.7i.

### 3.3 DATA ANALYSIS

The goal of this analysis is to provide logical comparisons of certain soil-structure-interaction properties based on physical modeling. A great deal of information can be extrapolated from the plots mentioned in Section 3.2 (Fig. 3.7). Four parameters were selected to characterize the response of the footings to the cyclic and dynamic loads:

$M_{MAX}$  = the maximum moment capacity

$H_{MAX}$  = the maximum horizontal shear force capacity

$\theta_y$  = the rotation associated with yield

$k_{Me}$  = the small-strain rotational stiffness of the foundation

In order to determine these parameters, a “backbone” curve is constructed connecting the extreme points of each cycle in a plot of moment (M) versus rotation ( $\theta$ ) (Fig. 3.8). The maximum moment is considered to be the peak value of moment. To determine the rotation associated with yield, a line is drawn tangent to the initial slope of the backbone curve. The rotation associated with yield is considered to be at the intersection of this tangent line and the maximum moment line. The small strain rotational stiffness is the slope of the tangent to the initial portion of the backbone curve. Table 3.5 lists these parameters for several tests.

#### 3.3.1 Effect of Vertical Load F.S. on Maximum Moment and Shearing Behavior

The factor of safety associated with vertical loading was defined, as usual, as the ratio of the vertical load capacity for concentric pure vertical loading to the static vertical load. Vertical load capacities were calculated using the friction angles back-calculated from vertical bearing-capacity tests. The axial load capacity was directly measured in the experiments for several footing geometries, as indicated in Figure 3.4. Capacity,  $V_{MAX}$ , was considered to be at the intersection of the initial tangent stiffness line and the “residual” tangent line. Based upon the capacity measured axial load tests, the friction angle of the sandy deposits was back-calculated using the conventional bearing-capacity equation:

$$q_{ult} = cN_{cs}d_c + qN_{qs}d_q + 0.5 g B N_{\gamma}s_{\gamma}d_{\gamma} \quad (3.4)$$

where  $c$  is the cohesion,  $q$  is the overburden pressure at the level of the footing-soil interface,  $N_c$ ,  $N_q$ , and  $N_\gamma$  are the conventional bearing-capacity factors, and the  $s$  and  $d$  parameters represent the associated shape factors and depth factors proposed by DeBeer (1970), Hansen (1970), and Hanna and Meyerhof (1981). For dense and loose sand specimens, the cohesion was assumed to be zero. Rosebrook (2001) performed direct shear tests on the sand to investigate the effect of using WD40 cohesion; the cohesion due to the WD40 was on the order of 2% of the peak strength and this was considered to be negligible. The resulting back-calculated friction angles ranged between 36 and 43 for loose and dense sand specimens. For footing geometries that were not subject to axial load tests, the back-calculated friction angle was used to calculate the bearing capacity.

It should be noted that the determination of the vertical load capacity and hence the corresponding friction angle involve some subjective judgment. If a footing is guided and forced to penetrate directly into the soil, the load-displacement relationship in frictional soil tends to increase significantly as penetration increases. If a footing is free to rotate as it is pushed into the soil, the resistance will often reach a peak, followed by a load decrease. Thus the load-bearing capacity depends on the fixity.

It should be pointed out that in footing design, a conservative (low) value of friction angle is typically used by engineers to compute factor of safety. In our case, the factor of safety is based upon our best estimate, not a conservative estimate of the capacity. It may not be conservative to assume low friction angles for the soil if the yielding of the foundation is desirable as an energy-dissipation mechanism.

Figure 3.9 relates the maximum moment and the inverse of the factor of safety ( $1/FS_v = V/V_{MAX}$ ) with respect to bearing failure associated with each test. The moment is normalized by the ultimate bearing capacity of the soil and footing width. The expected trend is a parabola anchored at (0,0) and (1,0) and is centered about  $1/FS = 0.50$  (Cremer et al. 2001) and equation 2.3 presented in Chapter 2. In Chapter 4, the analysis of footing response using “Beam on nonlinear Winkler foundations (BNWF)” concepts is presented. The parameters chosen for the BNWF analysis method produced reasonable predictions of moment capacity. However, the experimental data points predominantly lie to the left of  $1/FS = 0.50$  ( $FS > 2$ ), which makes it difficult to see a clear peak in Figure 3.9. More tests would be needed to verify the behavior at lower factors of safety. However,  $FS < 2$  is not the typical case, and it turned out to be difficult

to construct the models for  $FS < 2$ . One reason for this difficulty was that the model structures tended to be very unstable for  $FS < 2$  without some lateral support.

Settlement was not accounted for in the calculation of  $FS_v$ . As a building settles, the amount of overburden increases, which would increase its factor of safety due to an increase in bearing capacity. With this in mind, all of the points would shift to the left, the heavier tests shifting more because of higher settlement. However, the maximum vertical load,  $V_{MAX}$ , was determined by pushing a footing, rigidly connected to the actuator arm, into the soil until failure, which was also at some depth below the soil surface. This correction would shift the points back toward their original position. Figure 3.10 shows the maximum shear force normalized by the maximum vertical force versus  $FS_v$  for the same tests. Again, the trend shown by available data is expected, but more information would be needed to verify the parabolic trend for low factors of safety.

### **3.3.2 Verification of a Three-Dimensional Failure Surface**

Ideally, three principal driving forces can define the capacity of a soil-structure system in a planar system: moment, shear, and axial load. Given any two of these external loads on a shallow footing, the capacity for the third can be estimated. Cremer et al. (2001) assumed that the three-dimensional envelope created by the variations of these factors is an ellipsoid. The horizontal slow cyclic test in clay and sand allow a plot of two pairs of these points in moment/shear space given that their factors of safety are equal (i.e., they have the same vertical axial load). The groundwork for the models is outlined in Chapter 5 of this report, but a plot is shown here with two theoretical failure envelopes in moment/shear space: one for sand ( $FS = 6.7$ ) and one for clay ( $FS = 2.8$ ) (Fig. 3.11).

### **3.3.3 Settlement-Rotation Relationships**

If engineers begin to account for the nonlinear soil-foundation interaction, it must be understood that a footing tends to accumulate vertical settlement as the moment and shear loads are cycled. During horizontal slow cyclic tests, loading was usually applied in packets of three cycles of a given amplitude, followed by three more cycles with a larger amplitude. The permanent displacement in a packet of cycles of similar amplitude was divided by the number of cycles in

that packet to compute the amount of settlement per cycle of a given rotational amplitude. Figure 3.12 is constructed from select tests of varying  $FS_v$ . The horizontal axis represents the rotation  $\theta$  for a given packet of cycles (slow cyclic tests) or averaged values of similar rotational amplitudes (dynamic tests). The vertical axis is the normalized vertical settlement,  $U_v$ , per cycle of that rotation demand. A family of curves may be determined based on the specific  $FS_v$  of each test. Plots shown in Figure 3.12 are chosen from slow-cyclic and dynamic data from the KRR and SSG series, as well as from experimental 1g data from Weissing (1979). For the slow cyclic tests, there is a very consistent trend that the normalized settlement  $U_v$ , decreases as the factor of safety increases. The trends are also fairly consistent with a limited amount of published data from experiments performed by others. There is also an apparent trend that the settlement in dynamic tests is significantly larger than the settlement in slow cyclic tests. A significant portion of this difference is attributed to the free-field settlement of the ground due to the dynamic ground shaking.

### 3.3.4 Slow Cyclic vs. Dynamic Events

Although the dynamic events modeled in these tests represent more closely the actual mechanics of seismic activity, the control of the building response is difficult in dynamic tests. In a dynamic test, during a large shaking pulse when the soil foundation yields, the building tends to be isolated from the ground acceleration and the soil nonlinearity absorbs a lot of the shaking energy. Slow cyclic events allow more precise control and measurement of rotational and sliding forces and displacements.

To analyze the dynamic events, a procedure was developed to calculate the dynamic inertial forces due to the mass and moment of inertia of the walls from the corresponding accelerations. The dynamic displacements were obtained from the accelerometer records and superimposed on the static data obtained from displacements. This new procedure worked well but involves more sophisticated processing and carefully selected filters to separate noise from the signals.

The data show that the moment-rotation relationships for slow cyclic and dynamic tests are quite similar. Figure 3.13 shows a dynamic data trend line (i.e., backbone curve) superimposed on a slow cyclic moment-rotation plot for the same building type after Rosebrook (2001) and recent tests. This suggests that the two agree very well and that slow cyclic

evaluation may be appropriate for simulating dynamic events. The settlement per cycle of loading observed in the dynamic tests tended to be greater than that observed in the slow cyclic tests. Much of the difference is attributed to the free-field settlement caused by the ground shaking. There is also some ambiguity in determining the number of cycles in a dynamic test because there were some small high-frequency cyclic rotations superimposed on the predominant frequency of footing rotation. The high-frequency cycles were not counted when computing the settlement per cycle. Perhaps the contributions of high-frequency components also add to the settlement in dynamic tests.

### **3.4 CONSIDERATIONS IN PLANNING FUTURE EXPERIMENTS**

At least one more model test series is planned, which will include testing of approximately eight more footing configurations. One of these will include static vertical loading. The models will use the single-footing configuration for all slow cyclic tests and one or two dynamic tests.

We will test at least one footing with a lower factor of safety. While  $FS < 2$  for axial loading only (neglecting moment and shear loads) is uncommon in practice, these low FS tests will be valuable for verification of the theoretical BNWF and macro-element modeling described in later chapters.

In order to verify the analysis procedures, it would be valuable to continue to investigate different load paths. In the slow cyclic tests so far, we have loaded the foundations only with cyclic horizontal loads. In the dynamic tests, there must have been some cyclic vertical loads associated with dynamic settlement or uplift, but these forces have not been well characterized in the tests so far. In September 2004, a vertical-horizontal biaxial shaker will also be available on the large centrifuge. At that time, it may be valuable to investigate how vertical ground shaking affects the moment-rotation response.

Neglecting the vertical oscillations due to dynamic settlement and footing uplift, a real shear wall building under horizontal ground shaking may approximately have constant vertical load, while the horizontal load,  $H$ , is varied. The height of application ( $h$ ) of the cyclic horizontal load depends on the height of the building. We have investigated walls where  $h/L$  is approximately 1.8 and 0.4. However, we have completed only two tests with the lower load height. At low heights, the deformation was dominated by sliding, while at the larger height, the deformation was dominated by rotation as can be seen in Figure 3.7. Perhaps selection of an

intermediate load height would provide an interesting coupling of the two deformation mechanisms.

Thinking in (V, H, M) load space, selection of the load height effectively controls the ratio of M/H. Loading at constant h means that the moment, M, is proportional to the horizontal load, H. It may be interesting from a practical point of view to study cases where M is out of phase with H. If a shear wall is attached to a moment frame, there is a possibility that the moment frame would apply a vertical load to the shear wall as it settles or uplifts. Thus the effect of cyclic vertical loads that depend on the vertical displacement of the shear wall relative to the moment frame might be an important practical problem. For verification of analysis methods, it may be desirable to apply cyclic inclined forces as well. A series of dynamic analyses of a moment frame building supported by a shear wall could provide the basis for selection of reasonable, more general, load paths that would be appropriate for future tests.

Some effort should also be dedicated to providing a better explanation of the differences in foundation settlement observed in slow cyclic tests and in dynamic tests. It would be valuable to further investigate the mechanism of building “settlement per cycle” during dynamic tests. Present data indicate that total settlements during dynamic shaking are much greater than they are in slow cyclic tests. We believe that much of the difference between settlements in static and dynamic tests is that the building settlements are superimposed on the free field settlements. However, the contribution of higher-frequency low-amplitude dynamic oscillations superimposed on low-frequency large-amplitude oscillations also needs to be considered.

So far, we have investigated only surface footings and footings embedded to depths of less than or equal to the footing width. Deeper embedment would greatly increase the horizontal load capacity of the footing relative to the moment capacity.

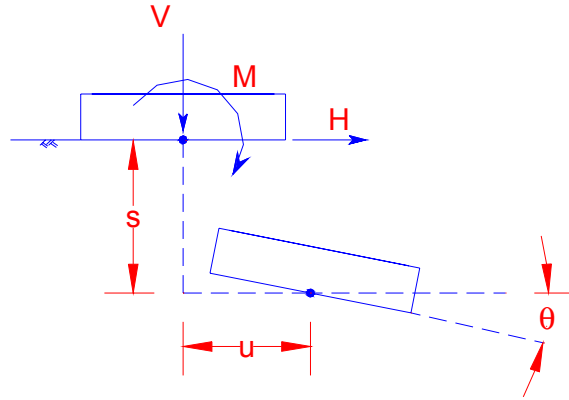
Our most recent proposal to PEER was to develop a two-degree of freedom multi-axial loading system. Using this system, the load height or inclination of the load could be varied during a test on one building, thus permitting data to be obtained for more than one load path for a given building configuration. For example, a cyclic horizontal load could be applied followed by an increase in the vertical load and then another series of cyclic horizontal loads. Or, the inclination of the load at a particular station could be varied in different loading packets. Thus more information could be obtained from each building; however the behavior observed in one packet of loading may be tainted by damage caused in previous loading packets.

Table 3.6 provides the beginnings of a table of proposed building and testing parameters planned for test SSG04.

### **3.5 SUMMARY AND MAJOR FINDINGS**

The research, to date, has effectively modeled shear walls and their shallow foundations on moderately dense sandy soil to produce seismic response data for varying realistic factors of safety.

1. There is great potential for the soil beneath a footing to dissipate a large amount of energy during dynamic loading. The moment-rotation relationships enclose a large area, and for the dry sand and stiff clay tested to date, the moment-resistance does not decay significantly with amplitude or number of cycles. The data have shown that the backbone of the moment-rotation curve and the hysteresis curves are similar for dynamic and slow cyclic loading tests.
2. The disadvantage of using a footing to dissipate energy is that the footing may experience permanent settlement, sliding, and rotation. These permanent deformations continue to accumulate with the number of cycles of loading, though the rate of accumulation of settlement decreases as the footing embeds itself.
3. An attempt was made to compare a normalized settlement per cycle as a function of the amplitude of the cyclic rotation. The relationship appears fairly consistent for tests in the present study as well as for tests performed by other researchers. The settlements tend to increase as factor of safety decreases and as the amplitude of rotation increases in a consistent pattern. Building settlements due to dynamic shaking are larger than the building settlements during slow cyclic tests for a given amplitude of rotation. Much of the difference appears to be due to free-field settlements, but this point needs further investigation.
4. The observed failure envelopes in moment-axial load space, and moment-shear load space seem reasonably consistent with empirical and theoretical envelopes proposed by others.



**Fig. 3.1 Nomenclature for force and displacement parameters associated with a displaced footing**

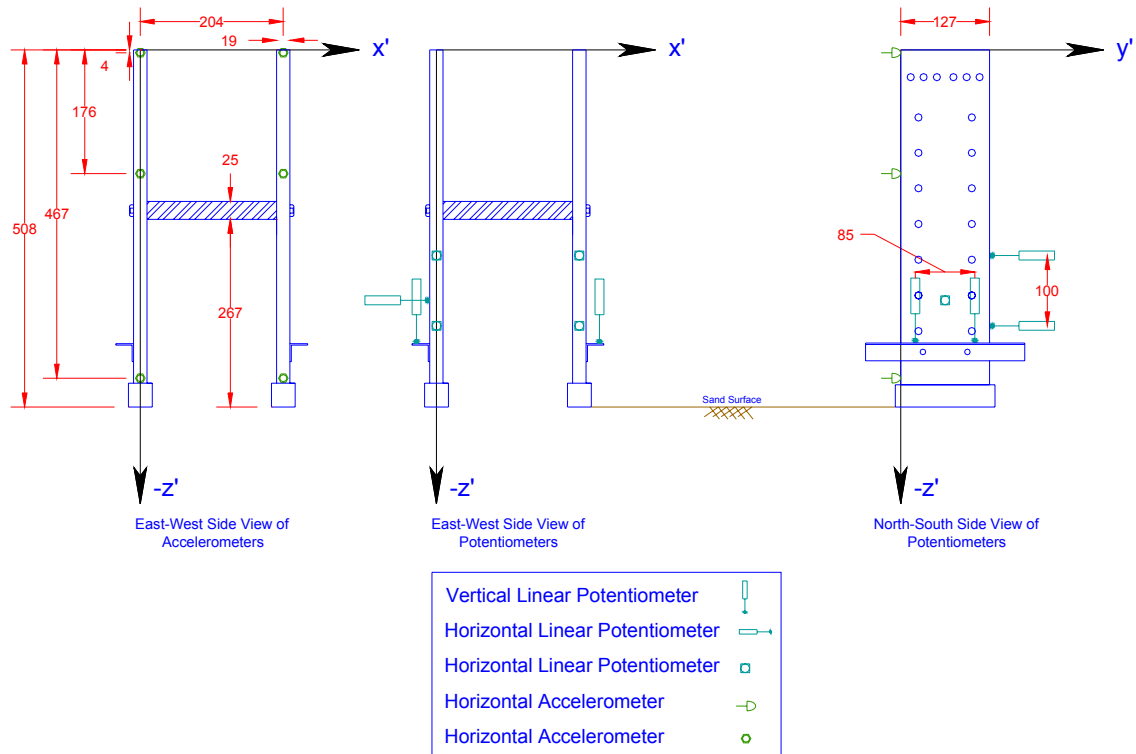


**Fig. 3.2a** Two views of structure and footing used for a double-wall test. Displacement transducers and actuator locations are also indicated. All dimensions are in model scale millimeters.

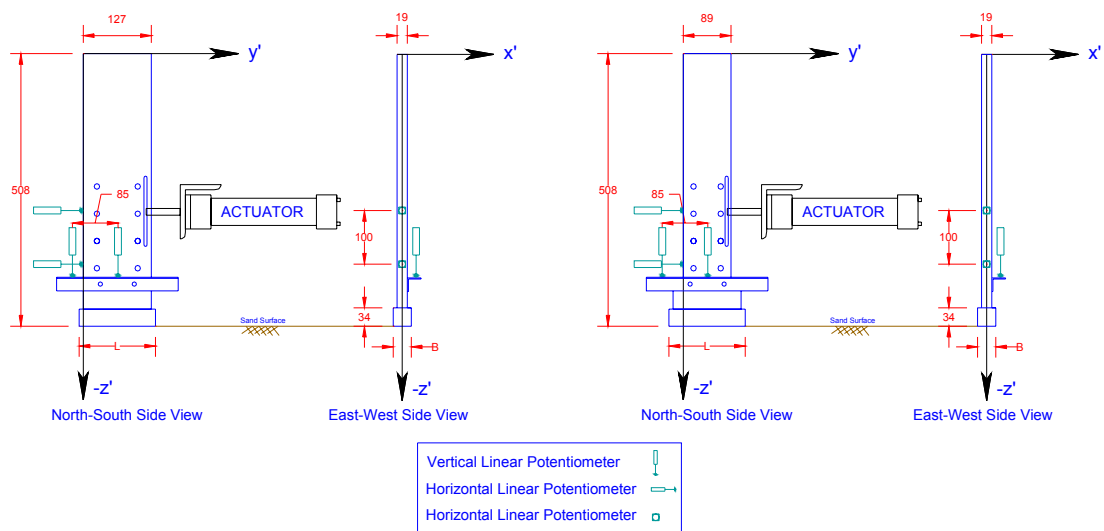


**Fig. 3.2b** Two views of standard weight shear wall made of aluminum (left) and heavy shear wall made of steel (right) used in single-wall tests. Displacement transducers and actuator locations are also indicated. All dimensions are in model scale millimeters.

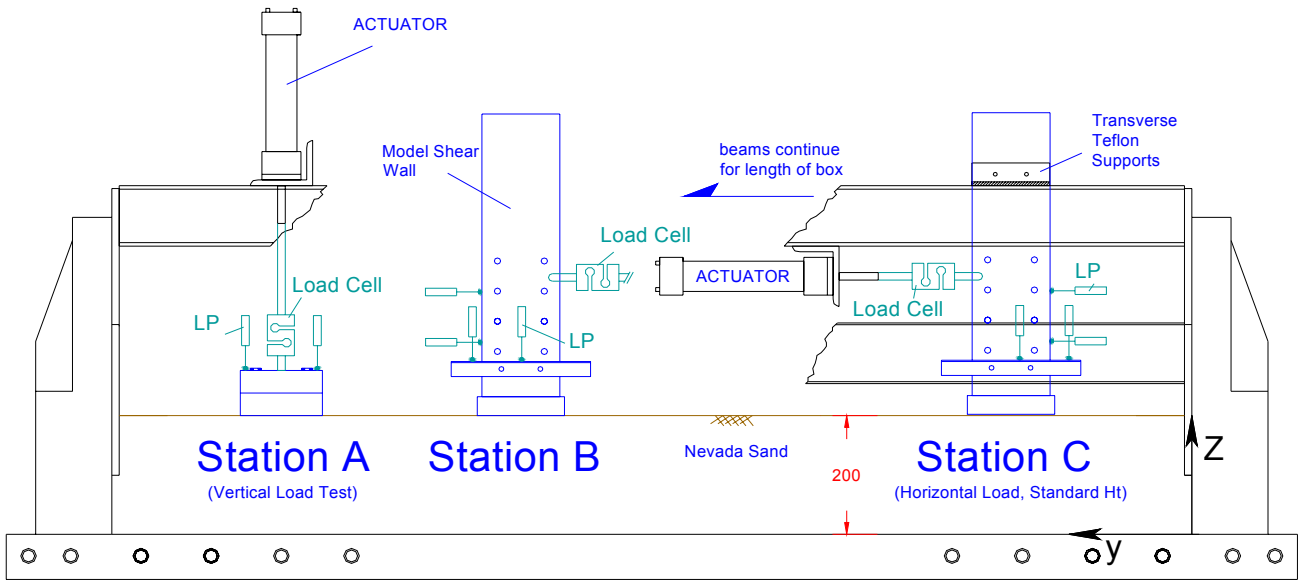
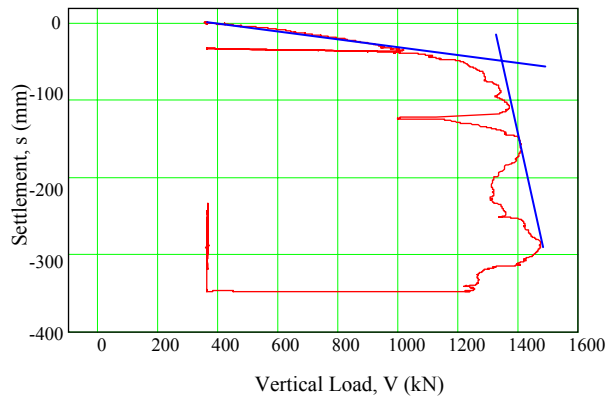
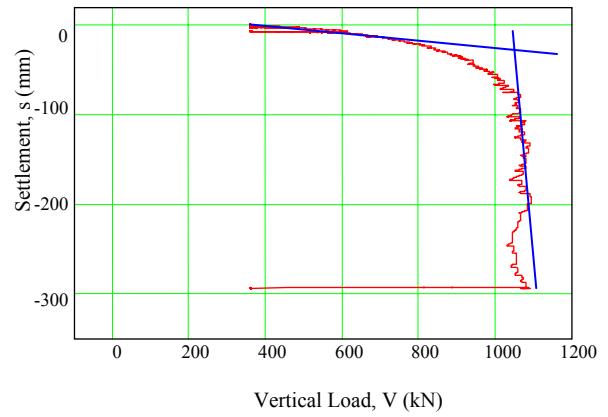


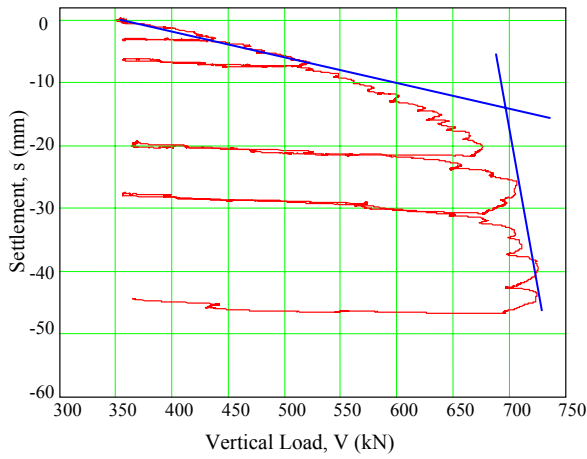
**Fig. 3.3 Side view of model container with selected wall and footing locations with typical instrument configuration for slow cyclic tests.**



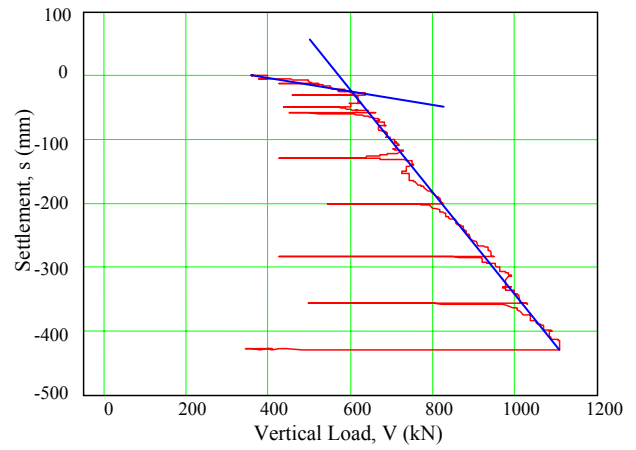
(a)



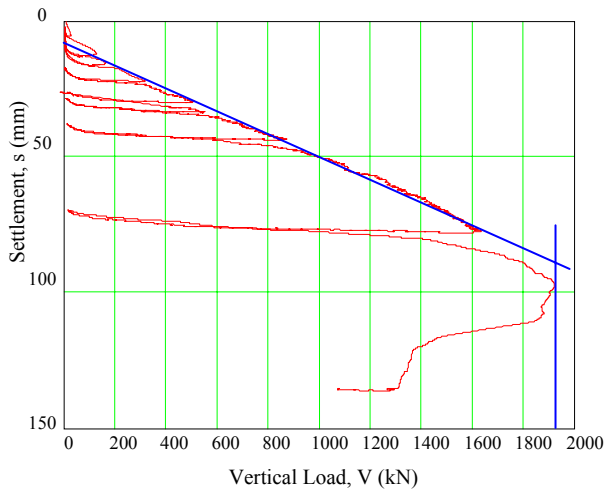
(b)



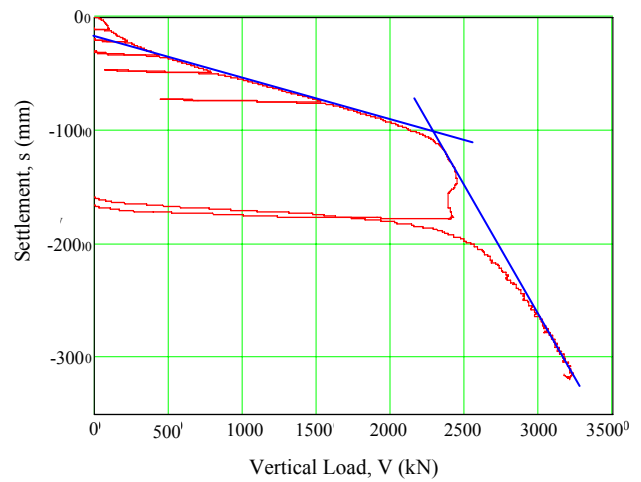
(c)



(d)

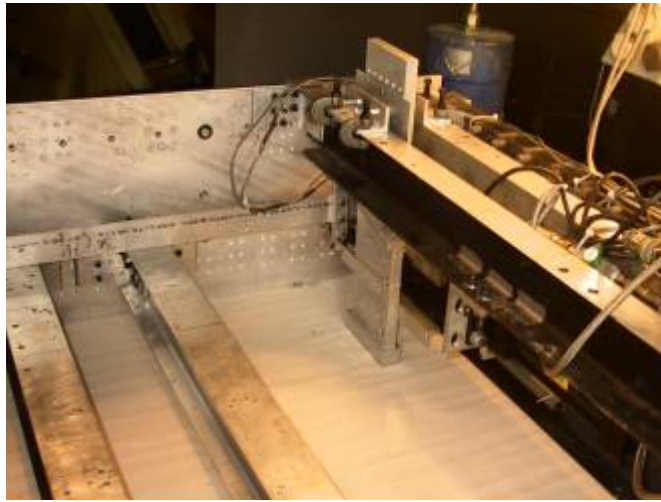


(e)



(f)

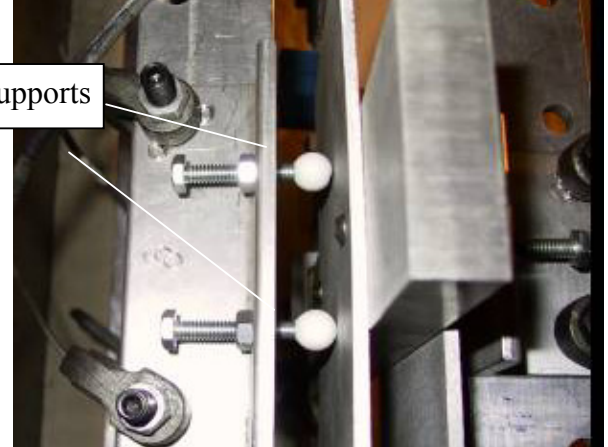
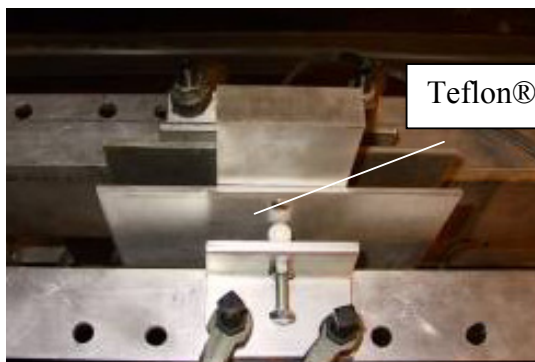
**Fig. 3.4 Load vs. settlement plots from slow cyclic vertical load tests for (a) KRR01-S2, (b) KRR01-S25, (c) KRR01-S31, (d) KRR02-S54, (e) SSG02 and (f) SSG02**



(a)

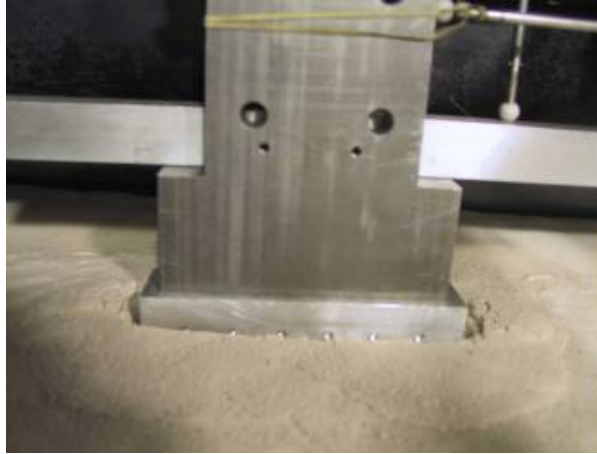


(b)



(c)

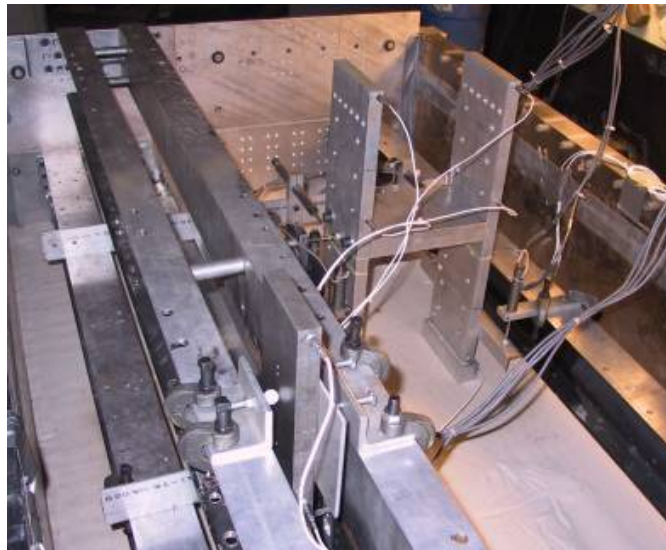
**Fig. 3.5 (a) Slow cyclic single aluminum wall ready for testing; (b) low horizontal slow cyclic test arrangement, aluminum wall; (c) teflon pads provide support to the single-wall system, restricting movement in the transverse direction**



(d)



(e)



(f)

**Fig. 3.5—Continued** (d) settlement and soil wedge failure after standard height horizontal slow cyclic test with heavy (steel) wall; (e) footing imprint preservation after horizontal slow cyclic test with sand surface pretreated with WD40 (f) dynamic test configuration with single steel wall (foreground) and double aluminum wall (background)

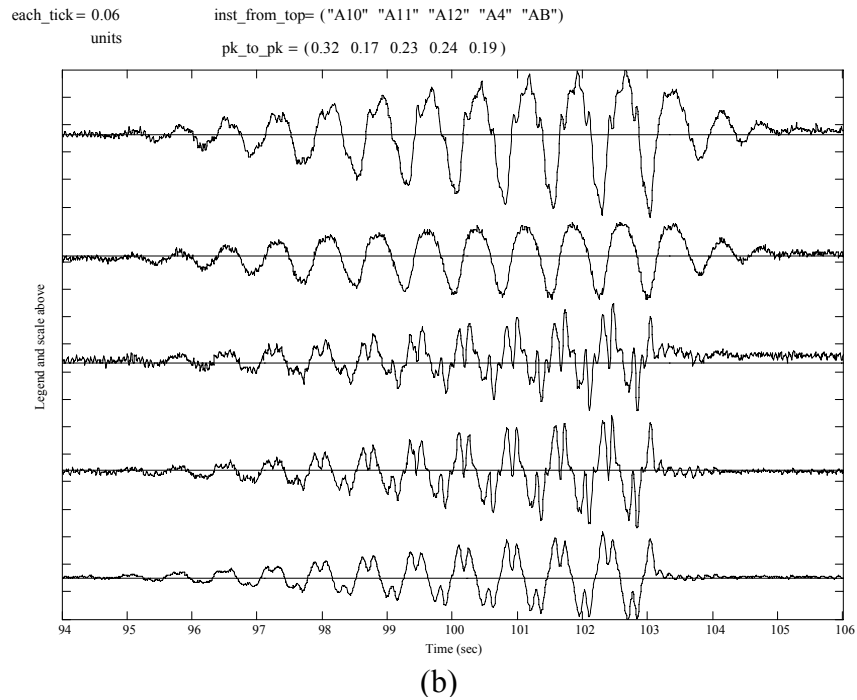
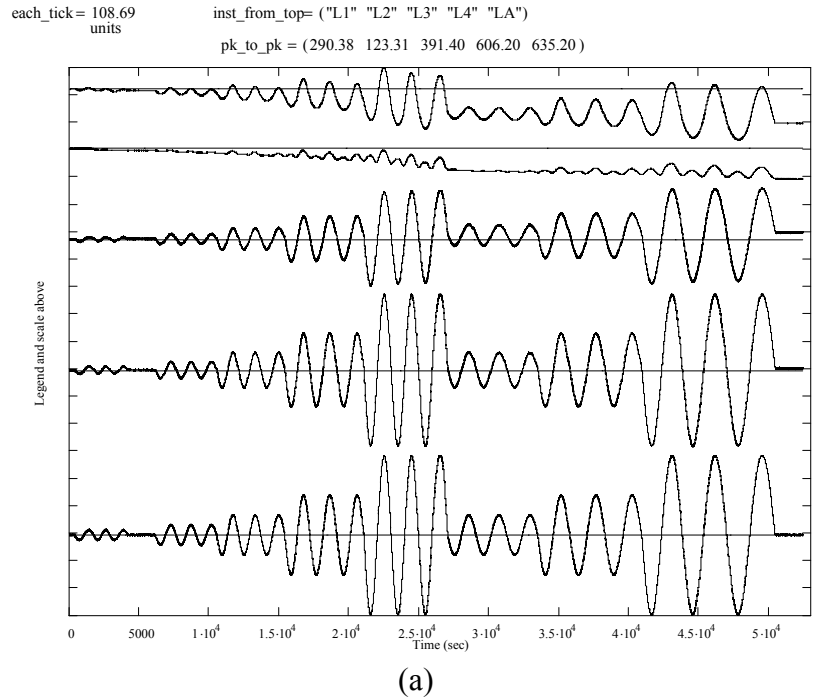


**Fig. 3.6 (a)Time histories of a horizontal slow cyclic test input motion (bottom), two horizontal potentiometer positions (middle) and two vertical potentiometer positions (top). SSG02, test#3a and (b) acceleration time histories of a dynamic test input base motion (bottom), middle of soil deposit (2<sup>nd</sup> from bottom) and response of footing, middle and top part of structure. SSG02, test#9e.**

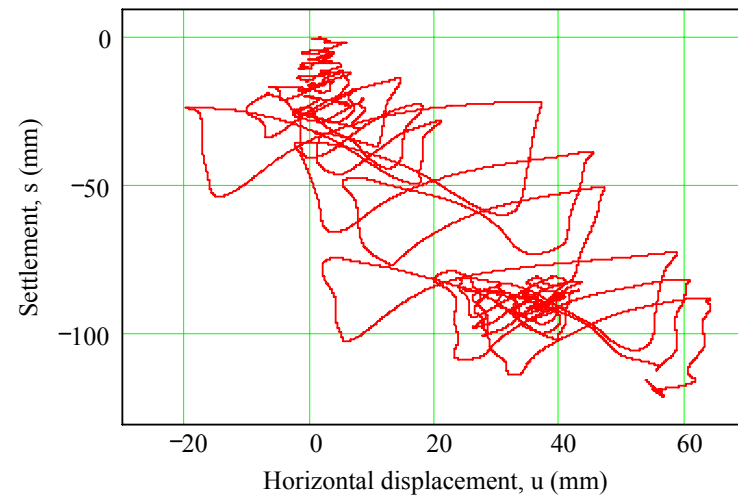
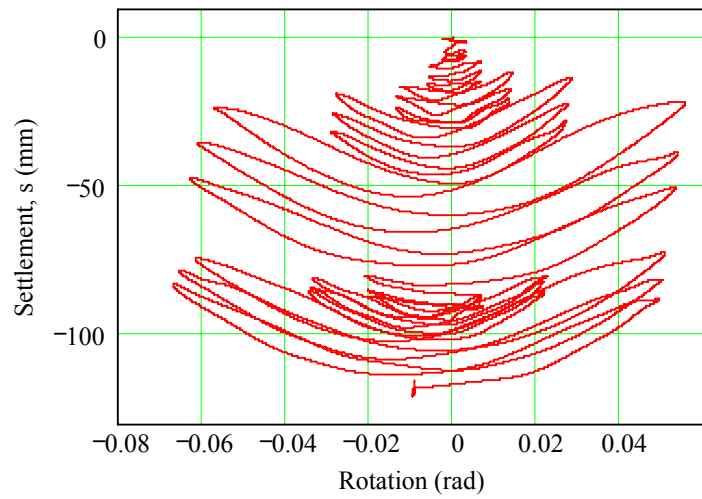
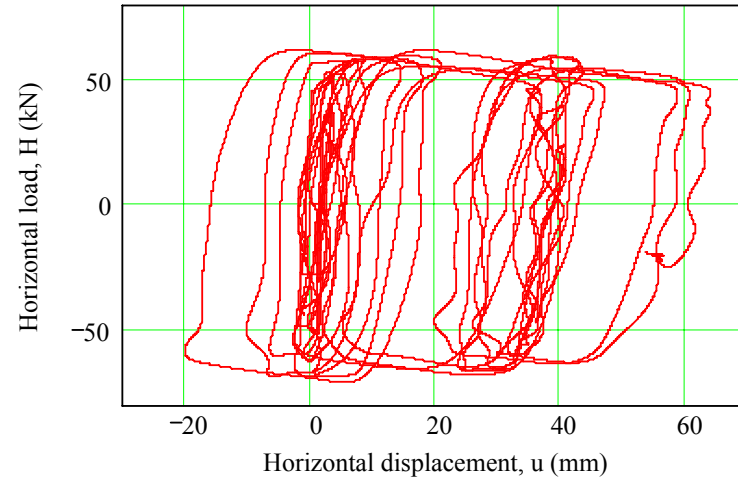
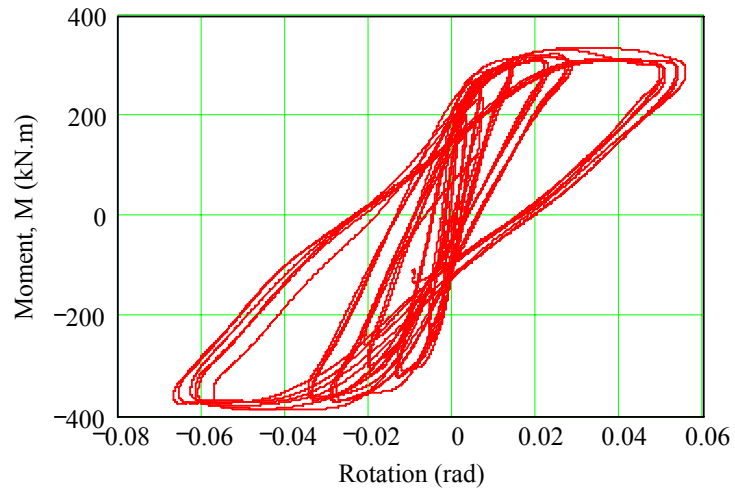


**Fig. 3.7 (a) Data from test SSG02, test#3a, FS = 6.7, embedment = 0.0m, load height = 4.9m, footing length = 2.84m**

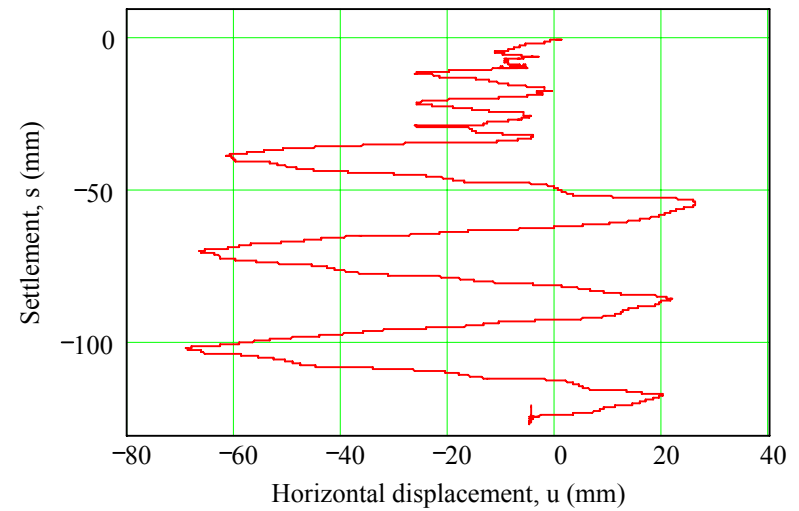
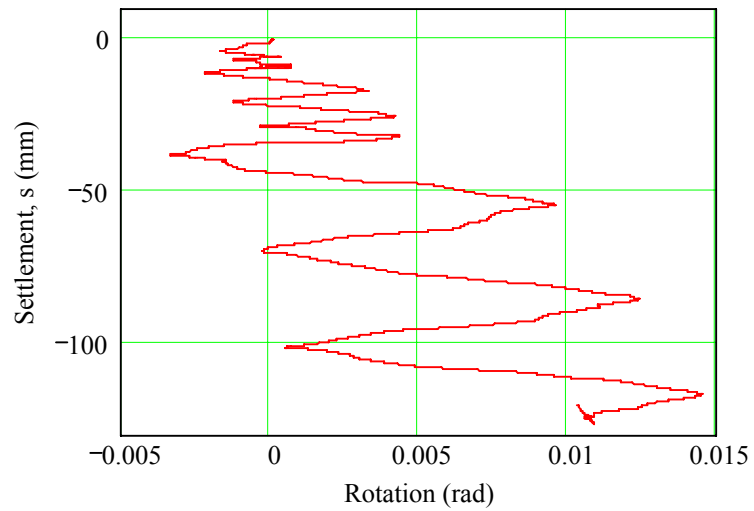
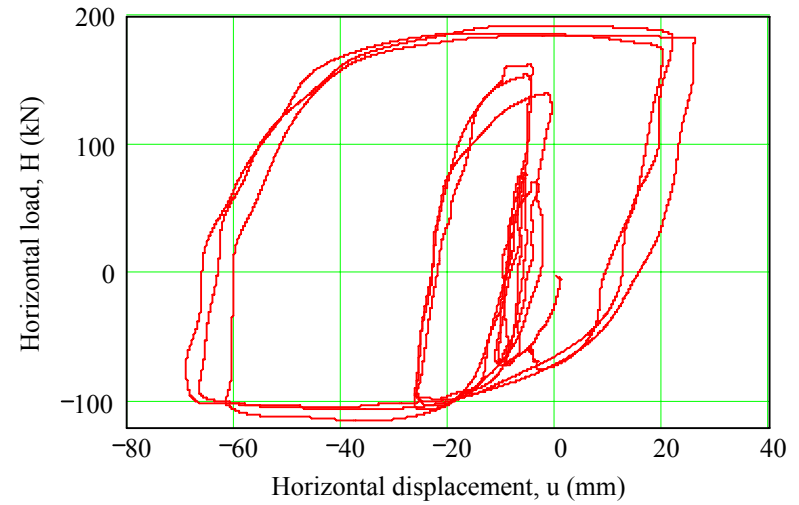
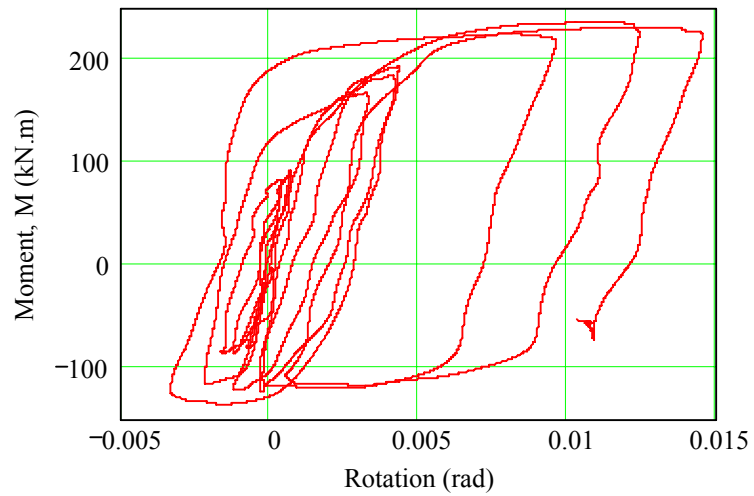


**Fig. 3.7—Continued (b) Data from test SSG02, test#6a, FS = 6.7, embedment = 0.0m, load height = 1.16m, footing length = 2.84m**

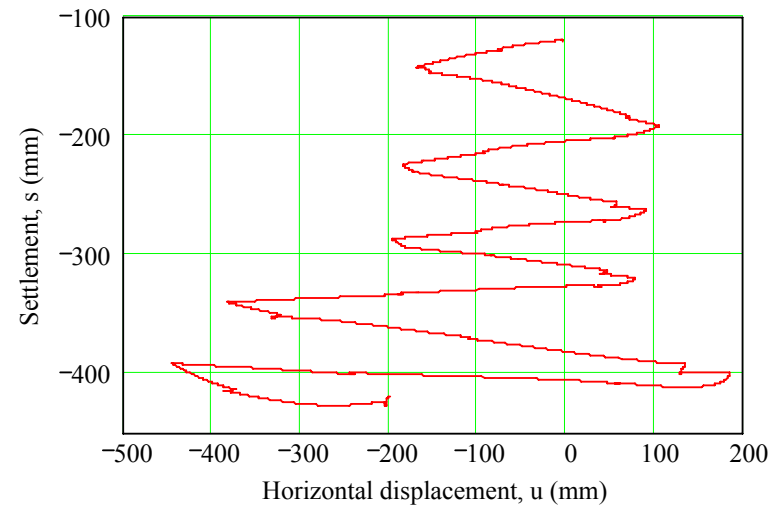
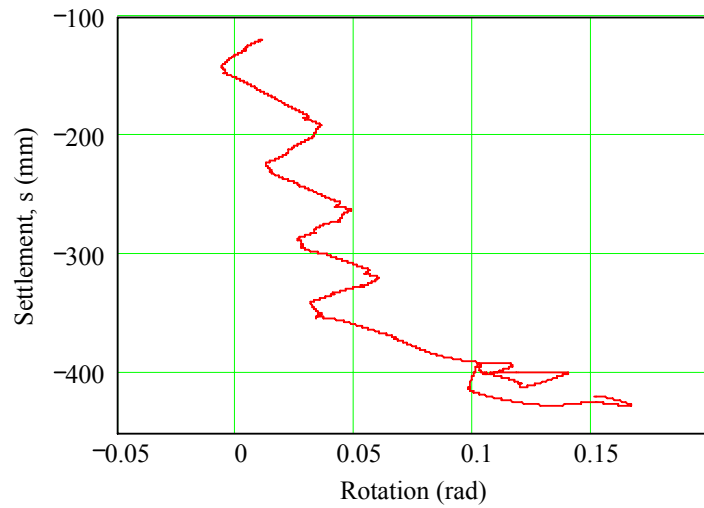
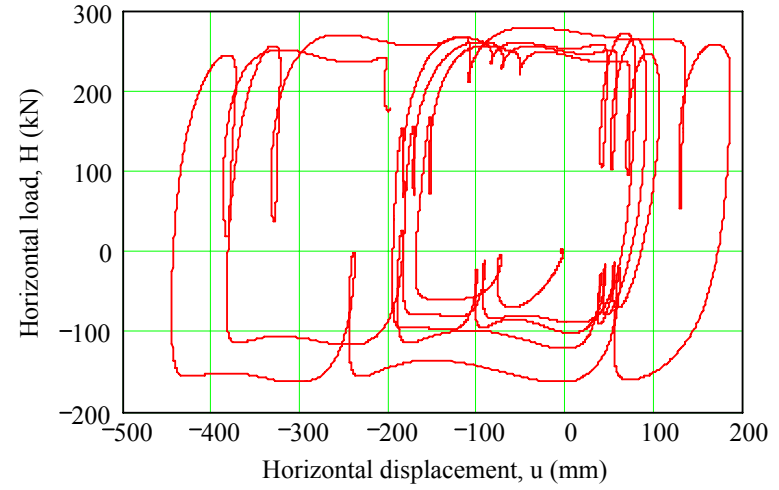
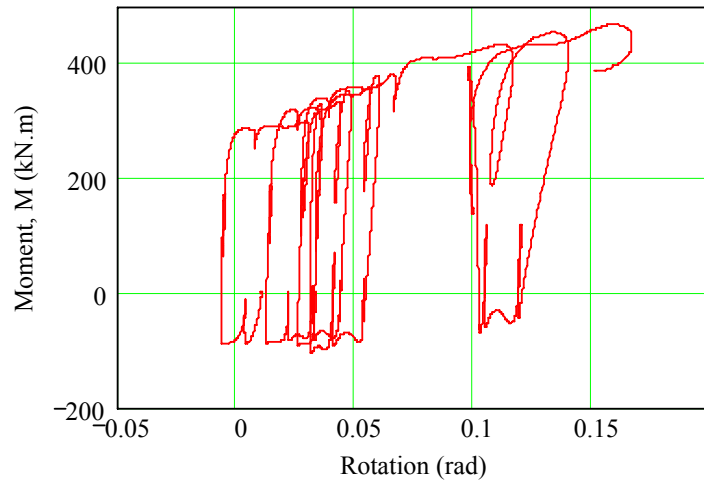


**Fig. 3.7—Continued (c) Data from test SSG02, test#6b, FS = 6.7, embedment = 0.0m, load height = 1.16m, footing length = 2.84m**

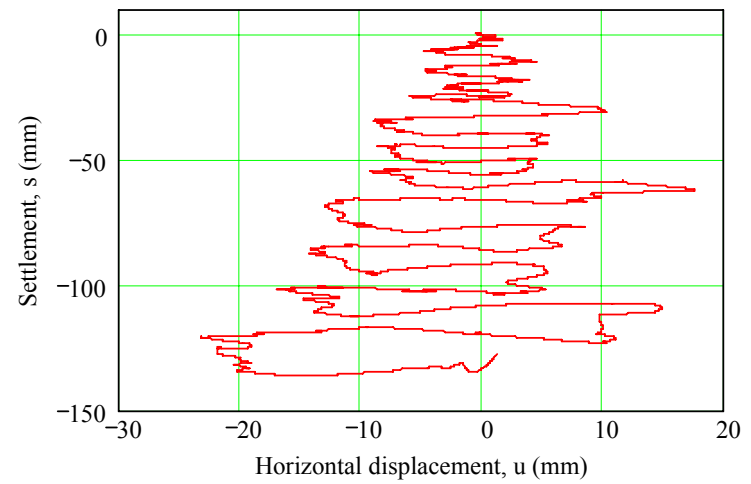
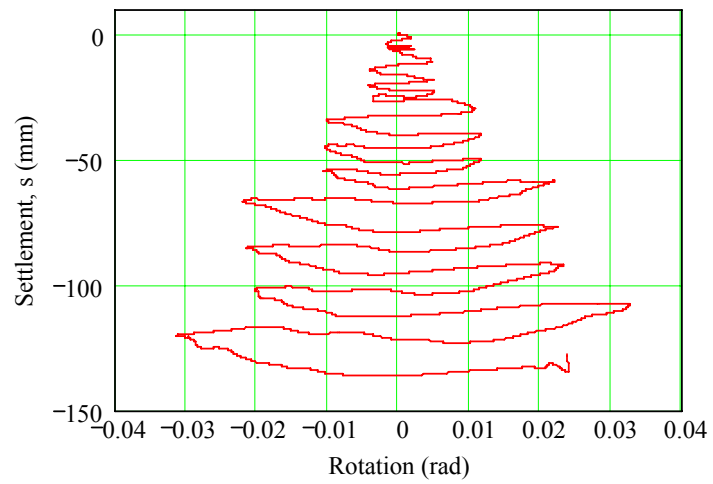
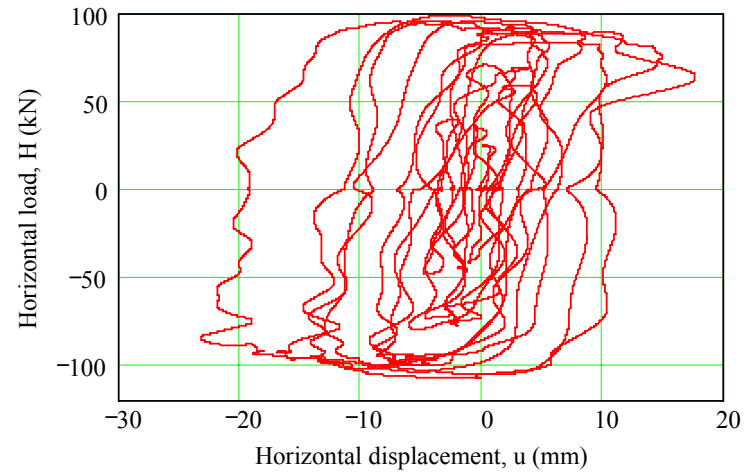
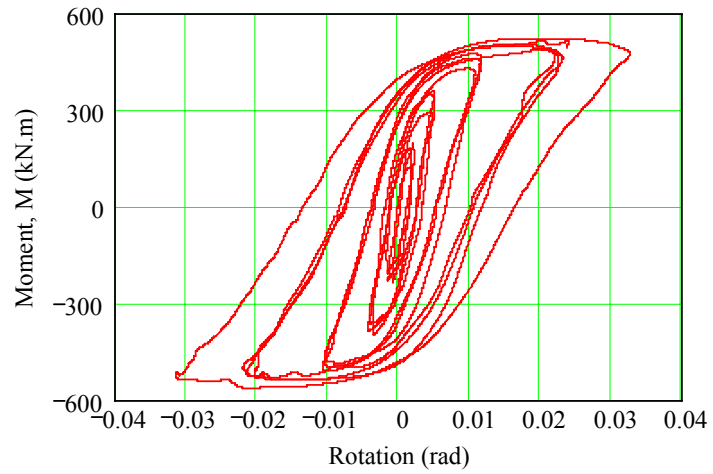


**Fig. 3.7—Continued (d) Data from test SSG02, test#5a, FS = 3.3, embedment = 0.0m, load height = 4.82m, footing length = 2.84m**

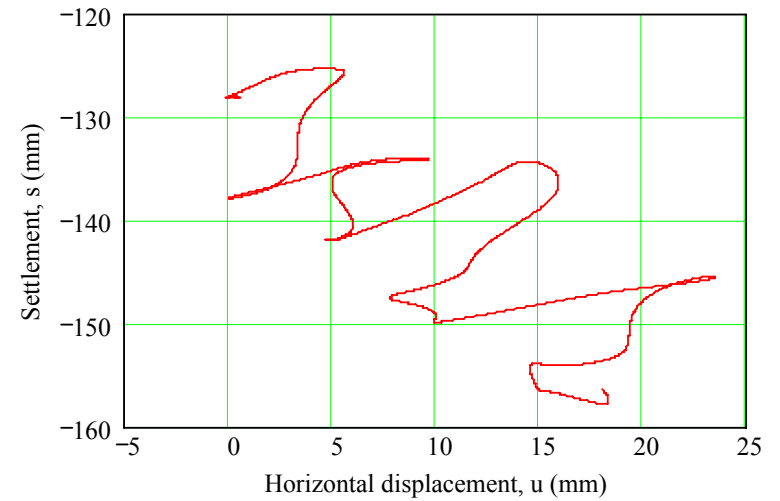
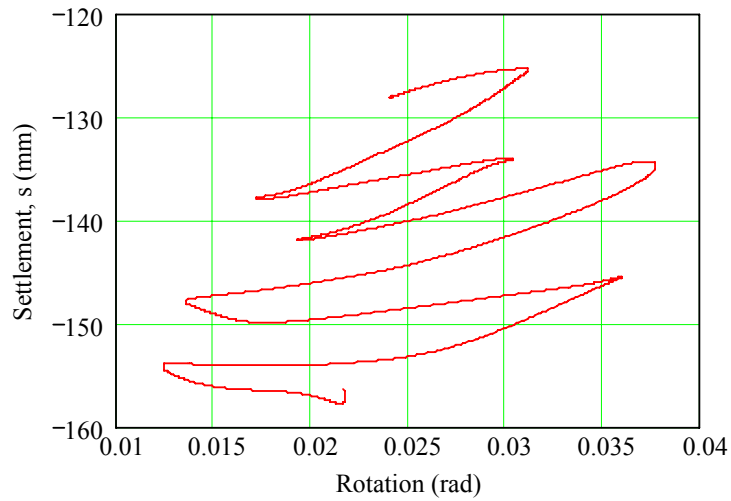
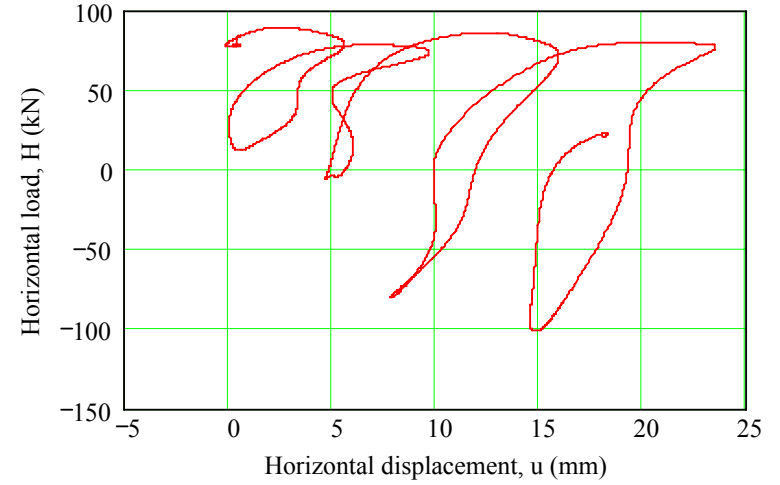
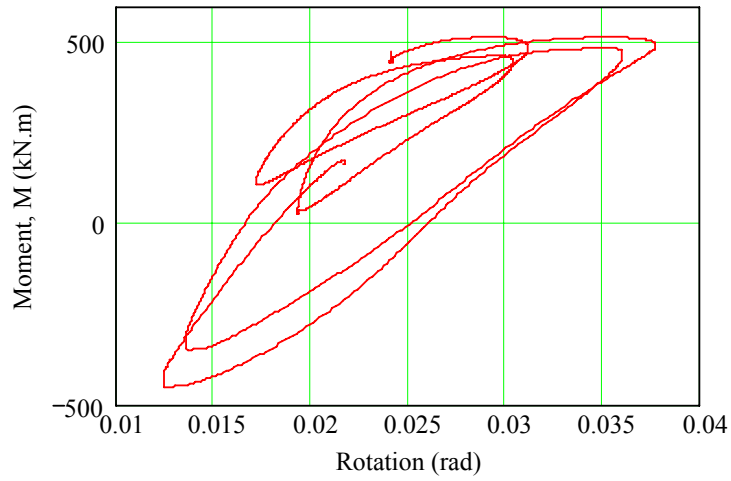


**Fig. 3.7—Continued (e) Data from test SSG02, test#5b, FS = 3.3, embedment = 0.0m, load height = 4.82m, footing length = 2.84m**

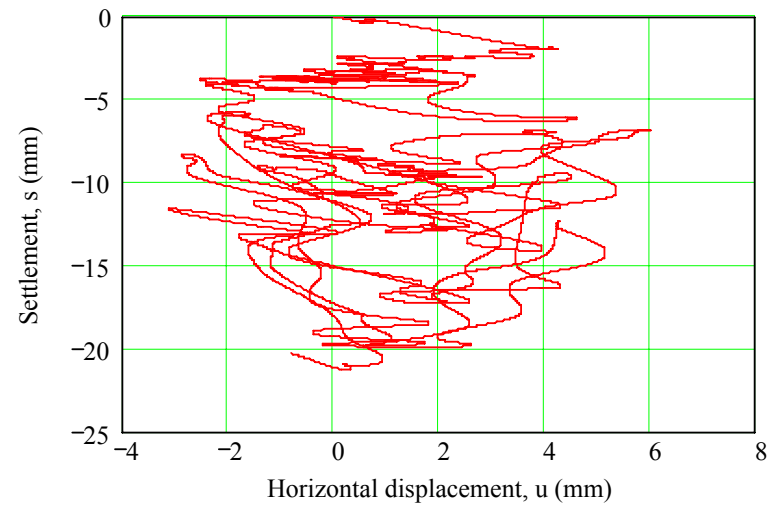
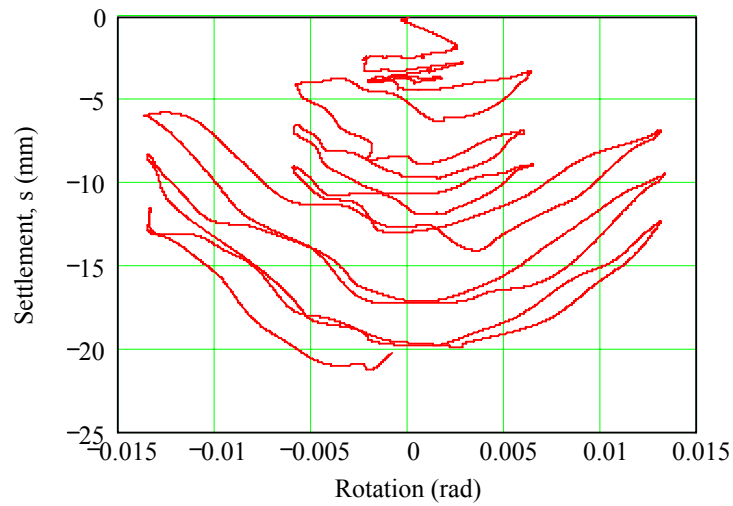
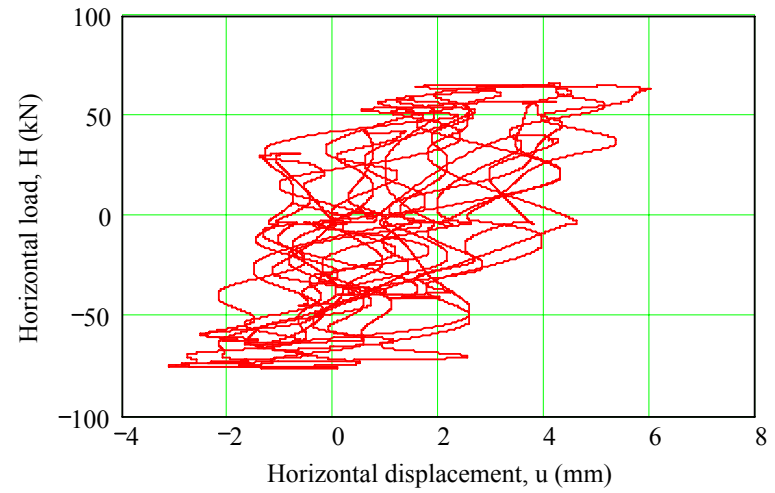
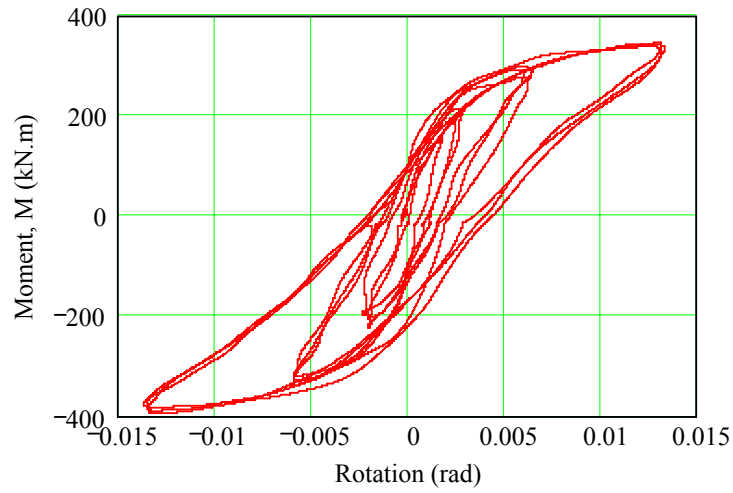


**Fig. 3.7—Continued (f) Data from test SSG03, test#2a, FS = 8.4, embedment = 0.7m, load height = 4.96m, footing length = 2.84m**

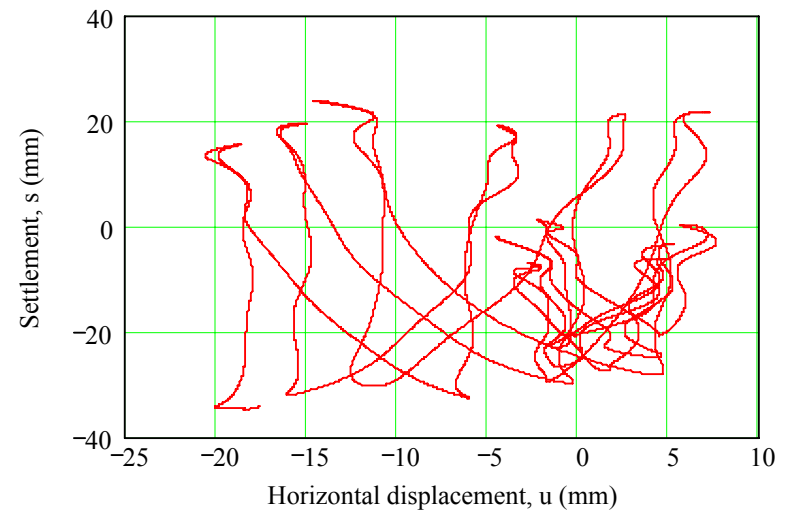
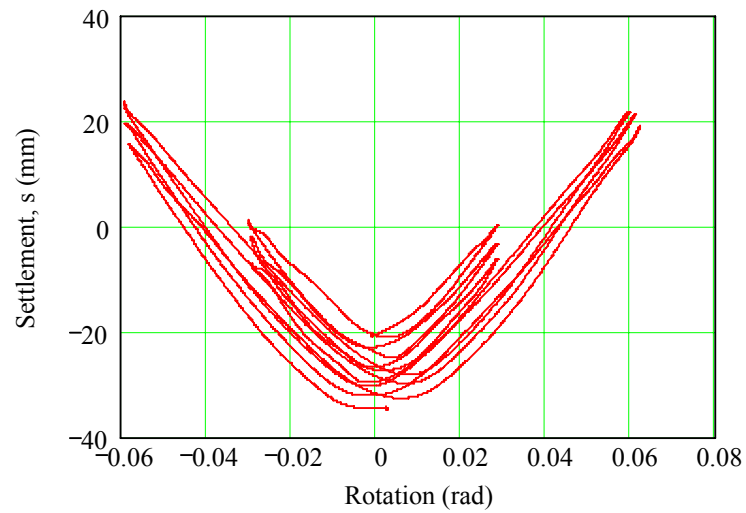
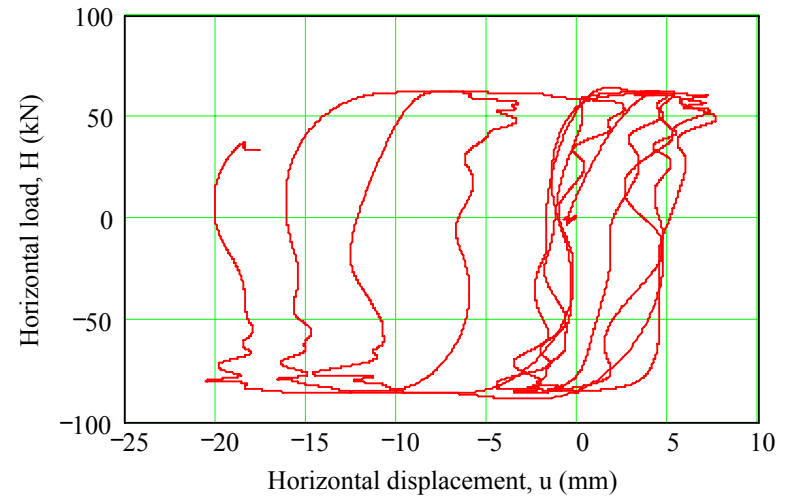
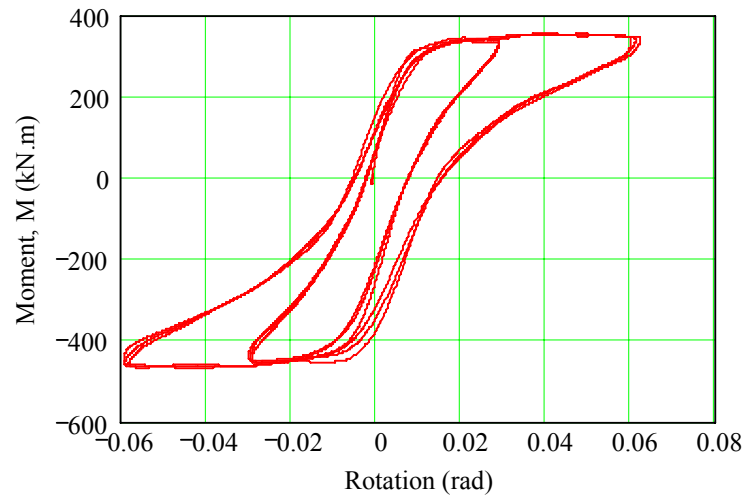


**Fig. 3.7—Continued (g) Data from test SSG03, test#2b, FS = 8.4, embedment = 0.7m, load height = 4.96m, footing length = 2.84m**

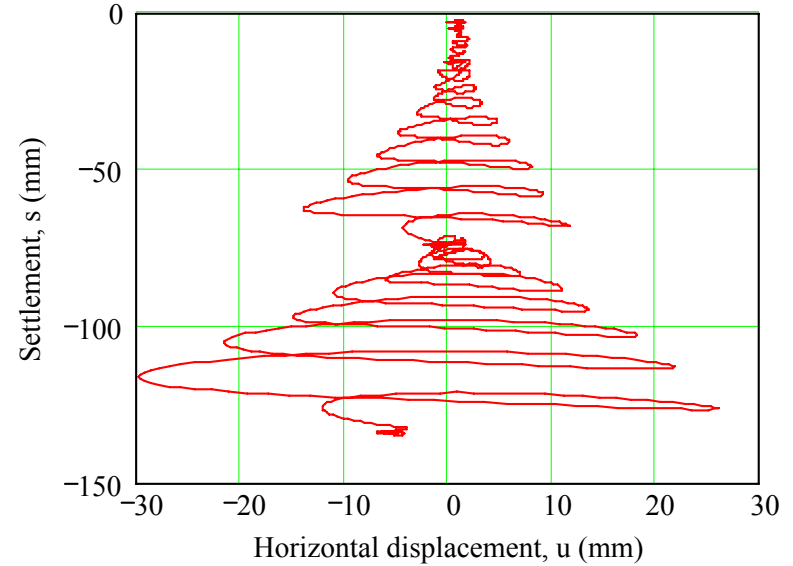
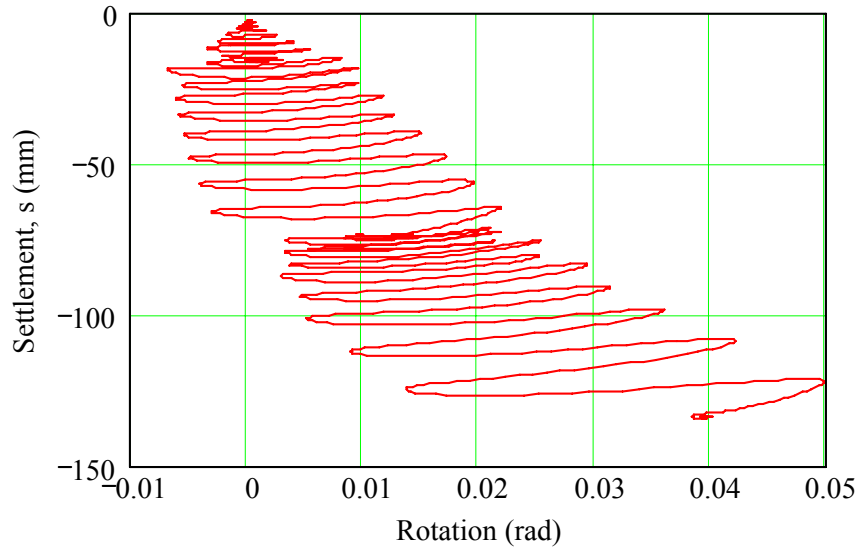
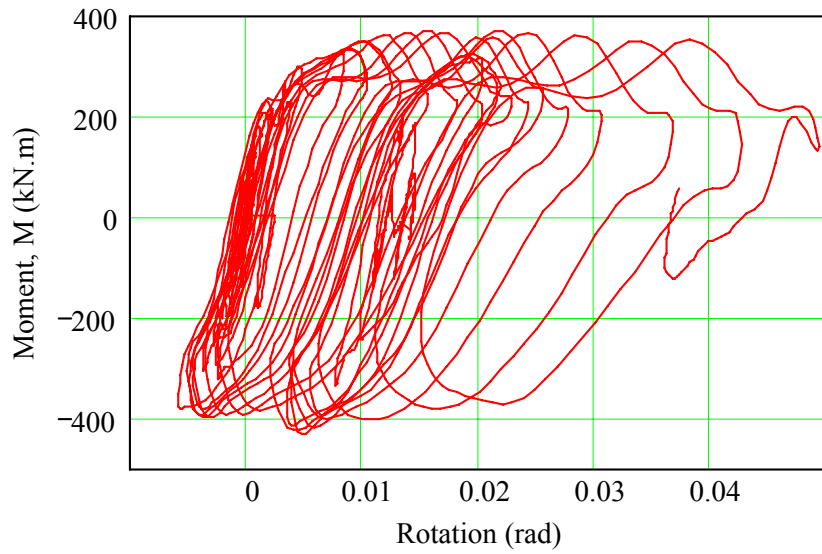


**Fig. 3.7—Continued (h) Data from test SSG03, test#8c, d, and e, FS = 6.7, embedment = 0.7m, footing length = 2.84m**

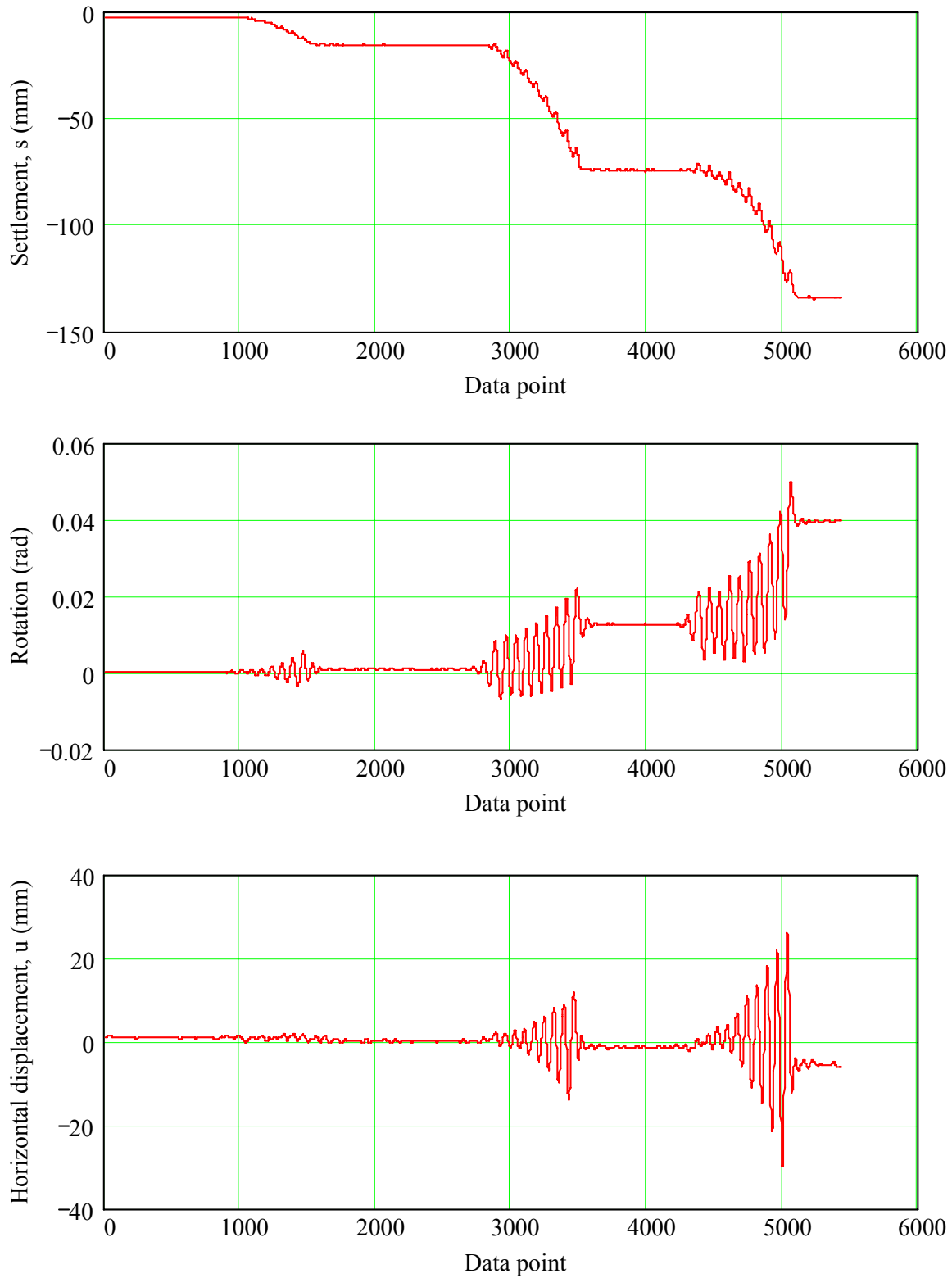


**Fig. 3.7—Continued (i) Time histories of settlement, rotation and horizontal displacement; SSG03, Dynamic tests, test#8a,b and c**

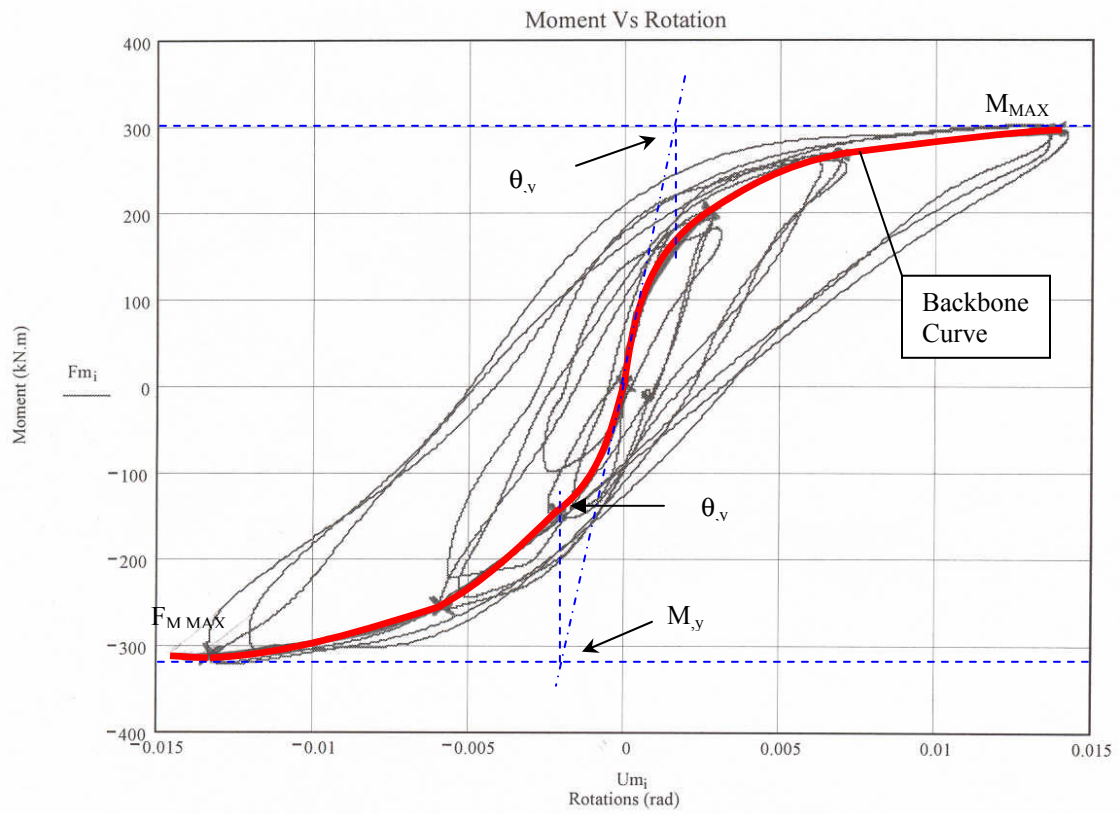


**Fig. 3.8 Determination of maximum moment, yield moment, and yield rotation from the development of a backbone curve in a moment-rotation plot. SSG02 test#3a**

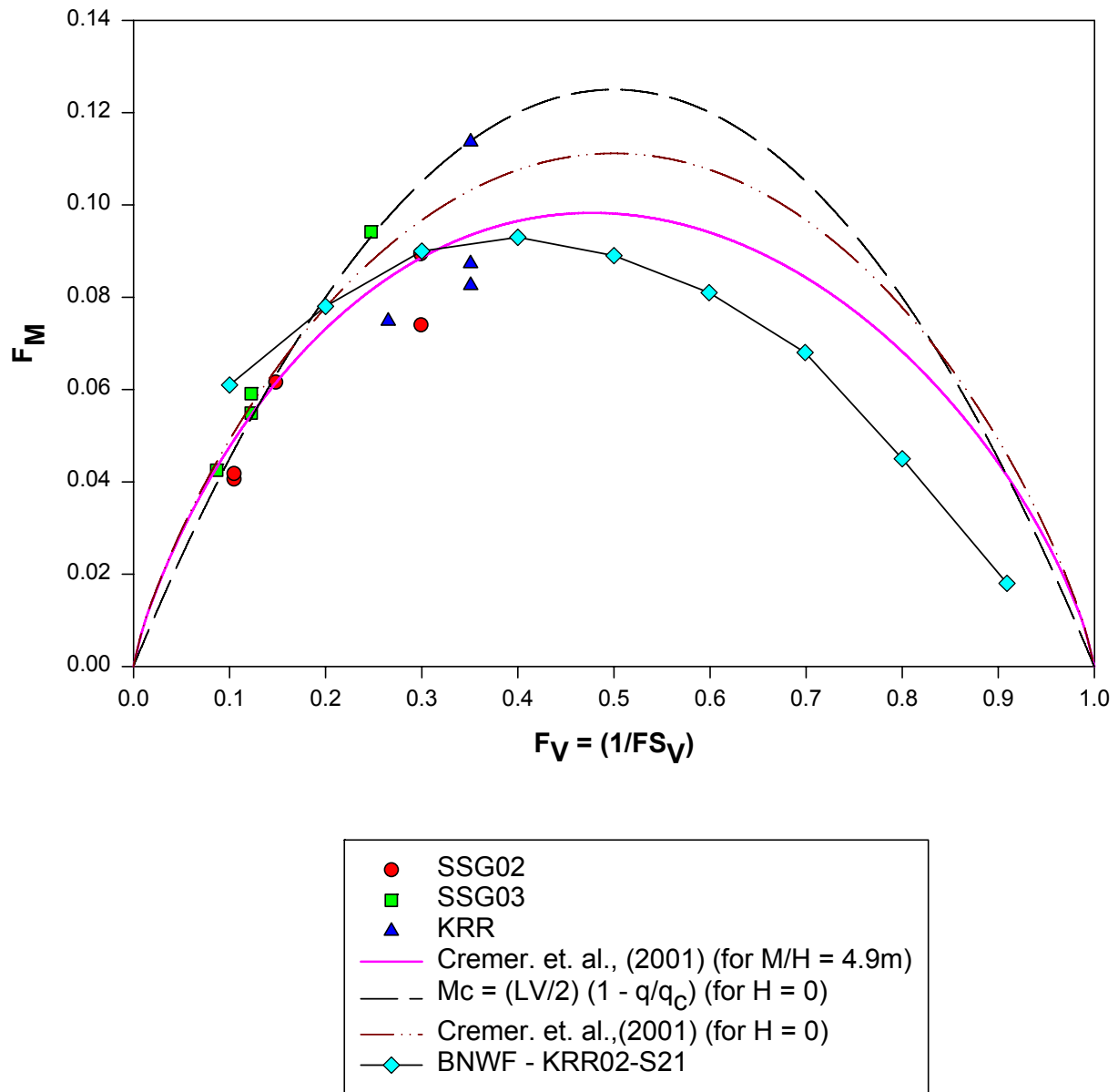


**Fig. 3.9 Maximum moment failure envelope from current test series and other theoretical surfaces**

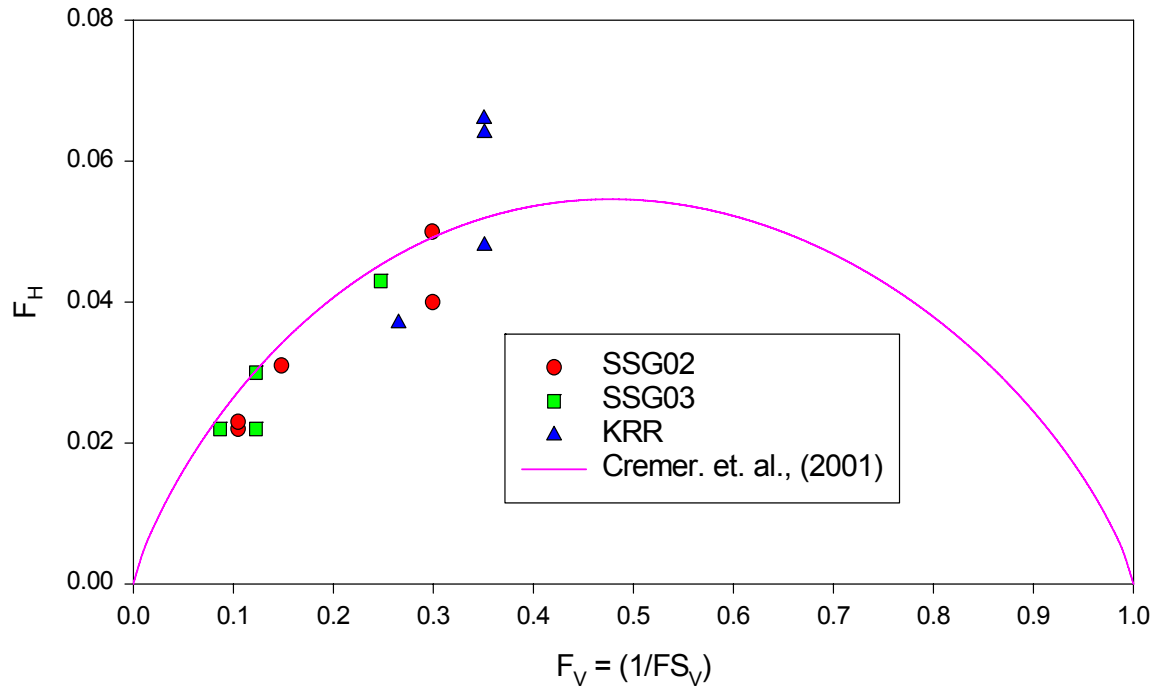


**Fig. 3.10 Maximum shear load failure envelope from current test series and theoretical parabolic surface after Cremer et al. (2001)**

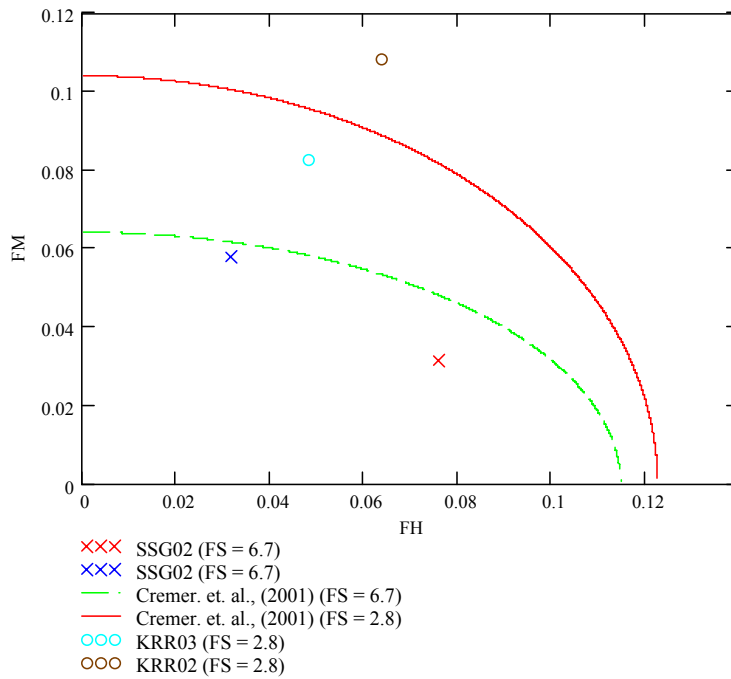


**Fig. 3.11 Elliptical cross sections of the failure envelope in constant V planes**

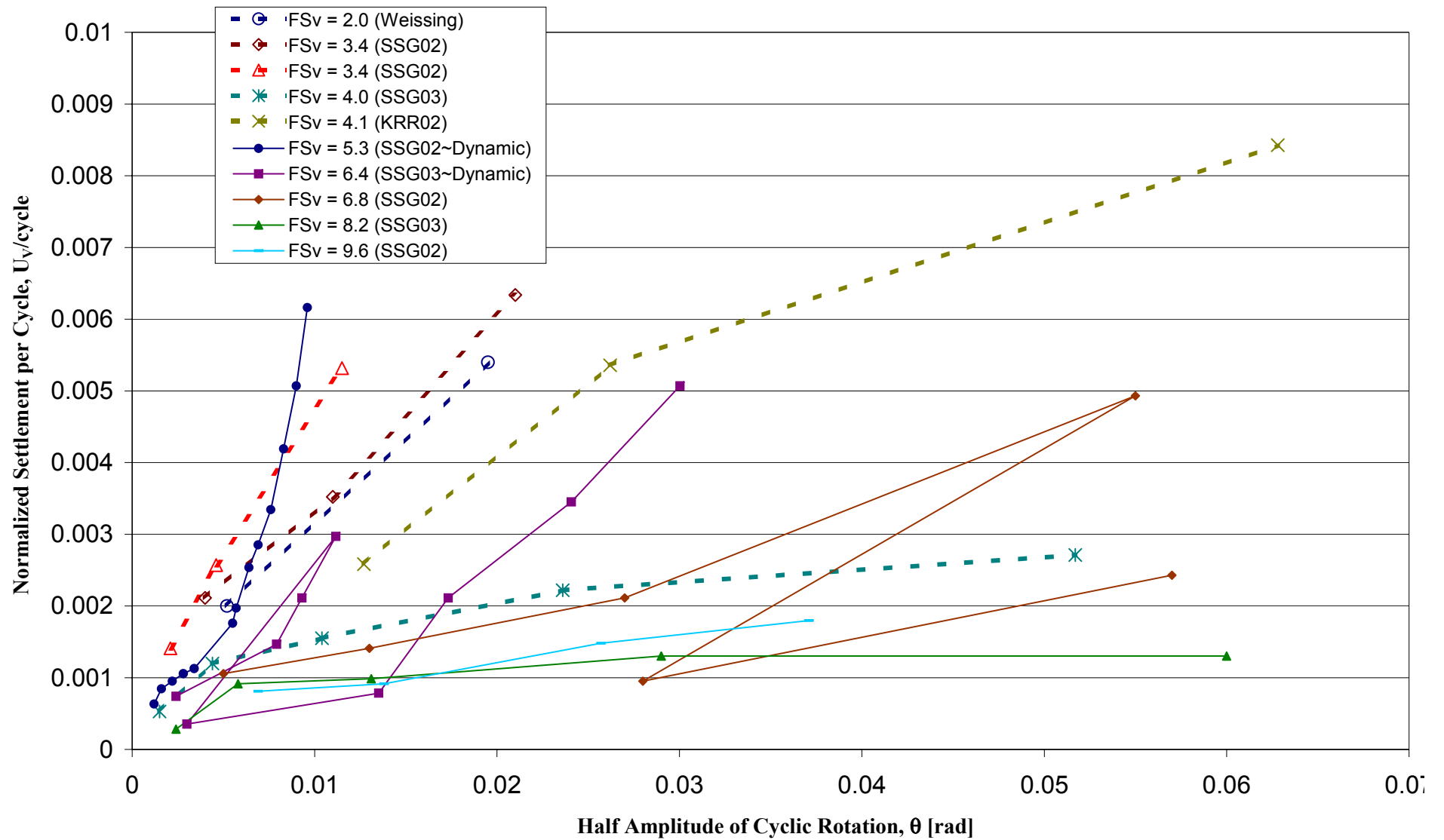
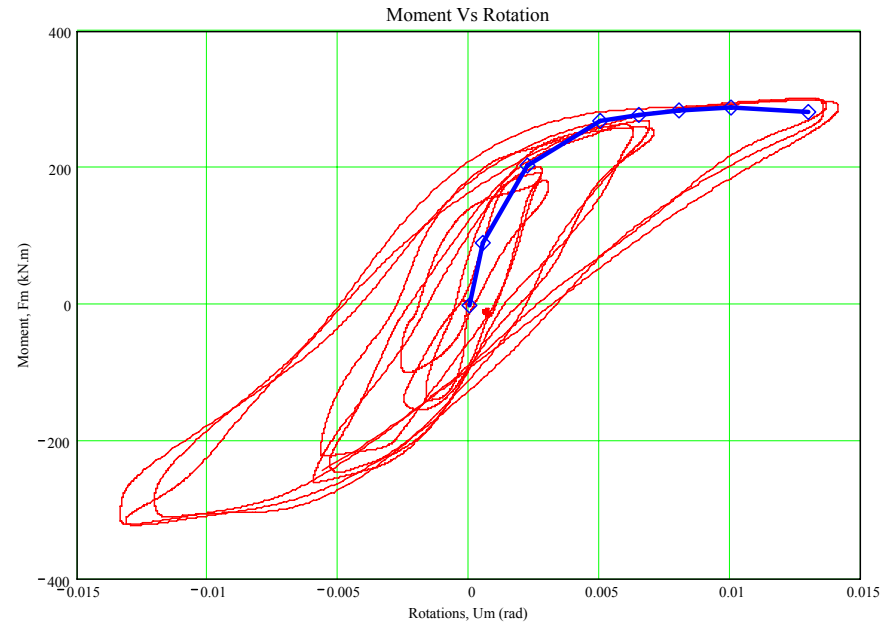
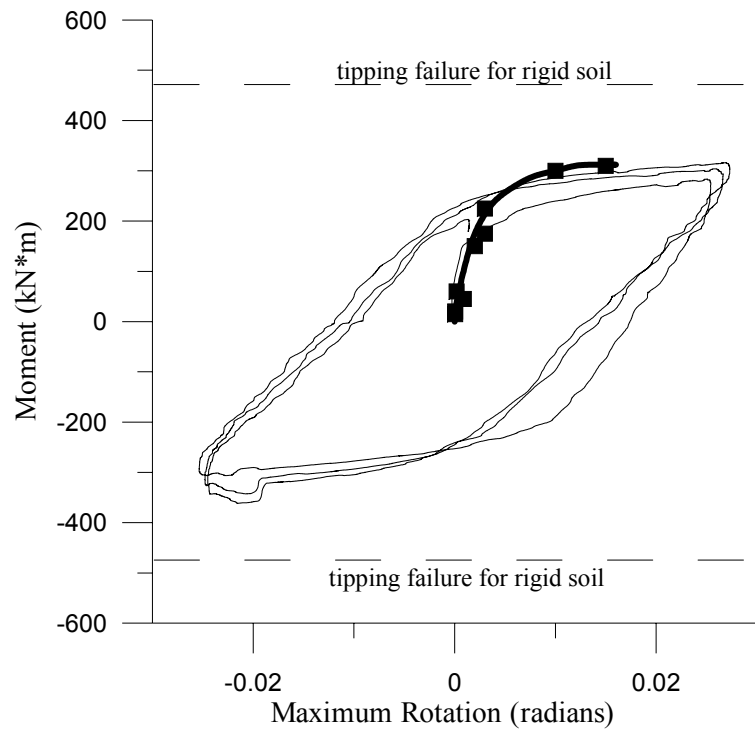


Fig. 3.12 Relationship between normalized settlement per cycle and half-amplitude cyclic rotation



**Fig. 3.13 Comparison of dynamic data trend line with slow-cyclic moment-rotation. KRRO02, test KRR02-S21 after Rosebrook, 2001 (left) and SSG02, test#3a (right).**

**Table 3.1 Centrifuge scale factors for basic parameters**

Parameter	Symbol	Scale Factor
Acceleration, Gravity	a,g	N
Density	$\rho$	1
Length	L	1/N
Mass	M	1N <sup>3</sup>
Force	F	1/N <sup>2</sup>
Stress, Strength	$\sigma,s$	1
Strain	$\epsilon$	1
Time (Dynamic)	t	1/N
Frequency	f	N

**Table 3.2 Determination of friction angle from vertical load tests**

Test Name	D <sub>r</sub>	B [m]	Emb [m]	V <sub>MAX</sub> [kN]	$\phi$ [deg]
K01_S2	80%	0.686	0.30	1350	37.7
K01_S25	60%	0.686	0.30	1050	36.6
K01_S31	80%	0.381	0.30	700	39.8
K02_S12	60%	0.686	0.00	600	36.8
SSG02	80%	0.690	0.00	1920	42.3
SSG03	80%	0.690	0.70	2320	37.0

**Table 3.3 Summary of the methods used to determine c<sub>u</sub>**

Method	Cu min [kPa]	Cu max [kPa]	Comments
Torvane	75	120	Strength decreases w/ time
Unconfined Compression	63	75	Possibly low due to disturbance and swelling before sampling and
SHANSEP	66	73	Does not include stress of footing. Uncertainty in water table
Back Calc. From Vert. Load Test	99	107	Includes effect of consolidation stress of footing

**Table 3.4 Test event summary**

Test Series	Soil Type	Soil Strength ( $\phi$ or $c_u$ ) <sup>1</sup>	Event Type <sup>2</sup>	Static FS <sub>v</sub>	Footing Length (m)	Footing Width (m)	Embed Depth [m]	Load Height [m]	Wall Type	Oil or No?
KRR01	Dry Sand (D <sub>r</sub> = 60%~80%)	$\phi = 37.7^\circ$	VSC	3.8	2.672	0.686	0.3	n/a	Double, Std Wt.	no
			HSC	3.8	2.672	0.686	0.3	Standard	Double, Std Wt.	no
		$\phi = 36.7^\circ$	HSC	3.0	2.672	0.686	0.3	Standard	Double, Std Wt.	no
			VSC	3.0	2.672	0.686	0.3	n/a	Double, Std Wt.	no
			VSC	3.0	2.672	0.686	0.3	n/a	Double, Std Wt.	no
			VSC	3.0	2.672	0.686	0.3	n/a	Double, Std Wt.	no
		$\phi = 39.8^\circ$	VSC	2.0	2.540	0.381	0.3	n/a	Double, Std Wt.	no
			Dynamic	6.2	3.944	1.080	0.3	n/a	Double, Std Wt.	no
		$\phi = 36.7^\circ$	Dynamic	2.8	2.672	0.686	0.3	n/a	Double, Std Wt.	no
			Dynamic	2.4	2.672	0.686	0.3	n/a	Double, Std Wt.	no
			Dynamic	2.4	2.672	0.686	0.3	n/a	Double, Std Wt.	no
		$\phi = 37.7^\circ$	Dynamic	1.3	2.540	0.381	0.3	n/a	Double, Std Wt.	no
Dynamic	3.0		2.672	0.686	0.3	n/a	Double, Std Wt.	no		
Dynamic	1.3		2.540	0.381	0.3	n/a	Double, Std Wt.	no		
KRR02	Dry Sand (D <sub>r</sub> = 60%)	$\phi = 36.7^\circ$	VSC	1.6	2.672	0.686	0	n/a	Double, Std Wt.	yes
			VSC	1.6	2.672	0.686	0	Standard	Double, Std Wt.	yes
			HSC	4.1	3.944	1.080	0	Standard	Double, Std Wt.	yes
			HSC	1.6	2.672	0.686	0	Standard	Double, Std Wt.	yes
			Dynamic	1.6	2.672	0.686	0	n/a	Double, Std Wt.	yes
			Dynamic	4.1	3.944	1.080	0	n/a	Double, Std Wt.	yes
KRR03	Bay Mud underlain by Sand (D <sub>r</sub> = 90%)	$c_u = 103$ kPa	VSC	2.8	2.672	0.686	0	n/a	Double, Std Wt.	n/a
			HSC	2.8	2.672	0.686	0	Standard	Double, Std Wt.	n/a
			HSC	2.8	2.672	0.686	0	Standard	Double, Std Wt.	n/a
			VSC	2.8	2.672	0.686	0	n/a	Double, Std Wt.	n/a
			Dynamic	2.8	2.672	0.686	0	n/a	Double, Std Wt.	n/a
			Dynamic	4.8	3.944	1.080	0	n/a	Double, Std Wt.	n/a
SSG02	Dry Sand (D <sub>r</sub> = 80%)	$\phi = 42.3^\circ$	VSC	n/a	2.840	0.690	0	n/a	Single Footing	no
			HSC	6.8	2.840	0.690	0	Low	Single, Std Wt.	no
			HSC	6.8	2.840	0.690	0	Standard	Single, Std Wt.	no
			HSC	9.6	2.840	0.690	0	Standard	Single, Light Wt.	no
			HSC	3.4	2.840	0.690	0	Standard	Single, Heavy Wt.	no
			HSC	9.6	2.840	0.690	0	Standard	Single, Light Wt.	no
			HSC	3.4	2.840	0.690	0	Standard	Single, Heavy Wt.	yes
			Dynamic	3.4	2.840	0.690	0	n/a	Single, Heavy Wt.	yes
			Dynamic	5.3	2.840	0.690	0	n/a	Double, Std Wt.	yes
SSG03	Dry Sand (D <sub>r</sub> = 80%)	$\phi = 37.0^\circ$	VSC	n/a	2.840	0.690	0.7	n/a	Single Footing	yes
			HSC	1.1	2.840	0.690	0	Low	Single, Heavy Wt.	yes
			HSC	8.2	2.840	0.690	0.7	Standard	Single, Std Wt.	yes
			HSC	8.2	2.840	0.690	0.7	Standard	Single, Std Wt.	yes
			HSC	4.0	2.840	0.690	0.7	Standard	Single, Heavy Wt.	yes
			HSC	11.5	2.840	0.690	0.7	Standard	Single, Light Wt.	yes
			Dynamic	4.0	2.840	0.690	0.7	n/a	Single, Heavy Wt.	yes
			Dynamic	6.4	2.840	0.690	0.7	n/a	Double, Std Wt.	yes

<sup>1</sup>See section 3.1.3 for determination of  $\phi$  and  $c_u$

<sup>2</sup>HSC: Horizontal Slow Cyclic

VSC: Vertical Slow Cyclic

**Table 3.5 Strength and yield characteristics for standard height horizontal slow cyclic tests**

KRR01 & KRR02

Station	m [kg] (model)	V (kN)	M <sub>MAX</sub> [kN-m]	M <sub>y</sub> [kN-m]	θ <sub>y</sub> [rad]	V <sub>MAX</sub> [kN]	H <sub>max</sub> [kN]	L [m]	FS <sub>v</sub>	1/FS <sub>v</sub>	V <sub>max</sub> *L [kN-m]	M <sub>MAX</sub> /V <sub>MAX</sub> L	H <sub>MAX</sub> /V <sub>MAX</sub>	Stiffness, k [M <sub>MAX</sub> /θ <sub>y</sub> ]
01-FE	4.56	358	270	n/a	n/a	1350	50	2.672	3.8	0.27	3607.2	0.075	0.037	n/a
02-AE	4.56	358	300	n/a	n/a	600	60	2.672	1.7	0.60	1603.2	0.187	0.100	n/a
02-CE	6.23	489	480	n/a	n/a	1394	92	3.944	2.9	0.35	5497.936	0.087	0.066	n/a

SSG02

Station	m [kg] (model)	V (kN)	M <sub>MAX</sub> [kN-m]	M <sub>y</sub> [kN-m]	θ <sub>y</sub> [rad]	V <sub>MAX</sub> [kN]	H <sub>max</sub> [kN]	L [m]	FS <sub>v</sub>	1/FS <sub>v</sub>	V <sub>max</sub> *L [kN-m]	M <sub>MAX</sub> /V <sub>MAX</sub> L	H <sub>MAX</sub> /V <sub>MAX</sub>	Stiffness, k [M <sub>MAX</sub> /θ <sub>y</sub> ]
B	3.62	284	312	148	0.0018	1920	60	2.64	6.8	0.15	5069	0.062	0.031	173333
D	2.56	201	206	112	0.0012	1920	42	2.64	9.6	0.10	5069	0.041	0.022	171667
E	7.31	574	453	283	0.0033	1920	96	2.64	3.3	0.30	5069	0.089	0.050	137273
F	2.56	201	212	118	0.0017	1920	44	2.64	9.6	0.10	5069	0.042	0.023	124706
G	7.32	574	375	221	0.0020	1920	77	2.64	3.3	0.30	5069	0.074	0.040	187500
J	4.6	361	--	--	--	1920	--	2.64	5.3	0.19	--	--	--	--

SSG03

Station	m [kg] (model)	V (kN)	M <sub>MAX</sub> [kN-m]	M <sub>y</sub> [kN-m]	θ <sub>y</sub> [rad]	V <sub>MAX</sub> [kN]	H <sub>max</sub> [kN]	L [m]	FS <sub>v</sub>	1/FS <sub>v</sub>	V <sub>max</sub> *L [kN-m]	M <sub>MAX</sub> /V <sub>MAX</sub> L	H <sub>MAX</sub> /V <sub>MAX</sub>	Stiffness, k [M <sub>MAX</sub> /θ <sub>y</sub> ]
C	3.62	284	336	169	0.0025	2320	52	2.64	8.2	0.12	6124.8	0.055	0.022	134400
D	3.62	284	362	194	0.0022	2320	69	2.64	8.2	0.12	6124.8	0.059	0.030	164545
E	7.31	574	577	278	0.0014	2320	100	2.64	4.0	0.25	6124.8	0.094	0.043	412143
G	2.56	201	260	180	0.0017	2320	50	2.64	11.5	0.09	6124.8	0.042	0.022	152941

**Table 3.6 Proposed tests for SSG03**

Type of Test	Weight of the Wall	Push Height	Static FS <sub>v</sub>	Embedment
Horizontal SC	Heavy	Low	3.0	3B
Horizontal SC	Heavy	Middle	3.0	3B
Horizontal SC	Heavy	Middle	1.5	B
Multi-Axial SC	Standard	--	--	--
Multi-Axial SC	Standard	--	--	--
Multi-Axial SC	Standard	--	--	--
Dynamic	Standard	--	--	--
Dynamic	Standard	--	--	--
Vertical SC	n/a	n/a	n/a	--

## 4 Nonlinear Winkler-Based Modeling

### 4.1 INTRODUCTION

Perhaps the most popular method used in design practice when modeling soil-foundation interaction (SFSI) is the beam-on-nonlinear-Winkler-foundation (BNWF) approach. The BNWF generalization originates from Winkler's (1867) early representation of the physical soil medium, which assumes a system of discrete, closely spaced independent linear elastic springs as shown in Figure 4.1. Such an approach assumes that a lateral reaction in the soil  $q$  per unit length at a given distance along the foundation is related only to the foundation deflection  $\delta$  at that distance. Based on this assumption, displacements of the foundation are confined to only the loaded regions of the footing. Heyenti (1946) provided an important extension to this by considering the deformation of the beam element through consideration of its flexibility. This general approach has become popular in the analysis of pile and pile group systems, whereby individual spring elements are simply placed horizontally (rather than vertically) and used to represent the lateral resistance of the soil and the soil-pile interaction forces. In either case (the shallow or deep foundation), the discretely placed springs result in a lack of coupling between individually placed spring elements; however the continuum effect provided by the soil may be implicitly included if the resistance curves are back-calculated from monotonic or cyclic loading experiments.

A predominant challenge with this modeling approach is the determination of the spring properties. In the case of a linear-elastic-spring assumption, the stiffness of the spring, represented by the modulus of subgrade reaction (or coefficient of subgrade reaction)  $k_s$  is required. Reversing the relation, the modulus of subgrade reaction is simply the ratio of the reaction at any point and the settlement produced by the loading at that point. Since the modulus of subgrade reaction is the only parameter idealizing the physical behavior of the soil, special attention must be provided to estimate this parameter. Common methods for determining the

modulus of subgrade reaction include the plate load tests, consolidation tests, triaxial tests, and the California bearing ratio (CBR) test.

Consideration of the nonlinear resistance of the soil and selection of associated parameters for this complicates the Winkler-based modeling efforts. Although nonlinear spring models are extensively used, and the mechanisms describing the observed physical behaviors are somewhat understood, there is no widely accepted analytical procedure for developing static, cyclic, and dynamic spring resistance curves from experimental data. Furthermore, the database from which nonlinear spring curves for sands or clays were developed is surprisingly small. This is particularly true for shallow foundations, where the literature of available experimental data is fairly small.

Physical mechanisms contributing to the overall soil-foundation response may be generalized as components that contribute to the near-field (near-structure) response and components that contribute the far-field (or far from structure) response. Adopting a generalized BNWF approach this allows for a mechanistic model with contributions in the near and far field associated with: (1) an elastic component representing the far-field deformation of the soil, (2) a plastic component representing the yielding of the soil close to the foundation, (3) a closure component that simulates the opening of gaps below the foundation (due to uplifting of the foundation) and (4) a drag component that simulates the transfer of forces along the sides of the foundation (edges of the strip footing for embedded footings for example). The schematic shown in Figure 4.2 adopts the configuration by Boulanger et al. (1999). In this case, closure and drag components are connected in parallel, while the elastic and plastic components are connected in series. Viscous damping on the elastic component may be used to approximate the loss of energy by radiation damping during dynamic loading.

Generally, one may anticipate that a more rigorous model representing any real system with a detailed representation of all observed physical mechanisms would lead to better results of system response. However, the uncertainty in determining the input parameters of the more rigorous model is often contrary to such anticipation. Therefore, the intent of using subgrade-type models has always been to strike a balance between theoretically more rigorous solutions and practicality and ease of use in routine geotechnical engineering practice. By now there are numerous publications discussing BNWF approaches applied to pile or pile-group foundations, correlating parameter selection assumptions in the model development (spring constitutive relations, modeling of gap or drag resistance, solution algorithms, etc.). For shallow foundations,

however, largely due to the limited experimental data, there are fewer Winkler-based numerical studies.

This chapter describes select results from an ongoing portion of this project focused on numerical modeling using Winkler-based concepts to capture the rocking response of shallow strip footings. A broad range of experimental data on rocking shallow foundations is selected from the literature and representative numerical models constructed of the various systems. A goal of this research is to analyze and provide guidance to the parameters of generalized nonlinear spring-type models used in Winkler approaches, which would reasonably capture the salient features of response important for performance-based design methodologies. Experimental systems modeled include centrifuge and 1g tests with a range of design vertical factors of safety from  $FS_v = 1.5\text{--}6.2$ , considering both clay and sand soil mediums. First, brief review of the literature is provided applicable to Winkler-based modeling, including select case histories. Although the concept has been applied, there is still much uncertainty in selection of parameters, appropriate constitutive rules, and modeling approaches. Further, with new numerical platforms, recent experimental data, and an increased interest by design practice for synthesizing modeling approaches, particularly with the move towards performance-based design, a detailed study evaluating BNWF techniques is warranted. This provides an opportunity to study the sensitivity of the modeling approach for capturing rocking response and accrued settlements due to such rocking.

## **4.2 BACKGROUND AND PREVIOUS WORK**

### **4.2.1 Numerical Studies**

There are several publications in the literature describing various Winkler-based approaches used for modeling the rocking response of shallow foundations resting on both elastic and inelastic soil medium, several of which consider the inelastic actions through the effect of uplifting of the foundation. Upon uplifting of the foundation, however, the equations of motion describing the system response become highly nonlinear; thus various researchers have also considered simple symmetric two-spring models to allow for linearization of the system of equations. Such an approach is generally more applicable for rigid structural systems. Descriptions of some of these are provided in this section.

Weissing (1979) used elastic-plastic springs coupled with Coulomb slider elements and subdividing the foundation into finite strips. This work considered two dimensions of loading, modeled after the experimental portion of the work. Elastic-plastic springs were considered to have only compression capacity, while Coulomb slider elements captured the uplifting of the foundation. The results from this numerical study provided good comparison with experimental results for the range of soil-foundations considered [also conducted by Weissing (1979)].

Prior to Weissing's work, Bartlett (1976) completed similar tests on a clay soil, with the same size footings and range of factors of safety. Analytical work was also performed, using a Winkler-based model with elastic-perfectly-plastic springs allowed to uplift. Three out of four tests considered the weak direction of loading, and  $FS_v$  ranged from 1.5–8. Good qualitative comparisons are made between the analytical and experimental results, with the following key observations: general degradation of soil modulus with increasing loading amplitude, the majority of permanent deformation occurs in the first large cycle of a set of similar amplitude cycles, and increasing energy dissipation with increasing rotation.

Psycharis (1982) considered two types of soil modeling using base springs: (1) the two-spring model and (2) the distributed Winkler (system) of springs. Nonlinearity at the foundation interface was considered through three mechanisms: (1) viscous dampers, (2) elastic-perfectly-plastic nonlinear springs, and (3) an impact mechanism allowing dissipation of energy at impact. Comparison of the solutions from theoretical equations developed on the basis of the two spring and distributed spring system were provided using response results from the Milliken Library building and a ground motion recording from the 1971 San Fernando earthquake. The primary conclusion from this numerical study was that a two-spring model was much simpler and provided reasonable enough response results for practical design. In a later publication by Psycharis (1983), a simplified two-spring system is used for studying the response of a multi-story building system.

Chopra and Yim (1985) and Yim and Chopra (1985) present two separate but similar studies evaluating the rocking response of single-degree-of-freedom (SDOF) and multi-degree-of-freedom (MDOF) systems considering uplifting of the foundation (SDOF the former paper, MDOF the latter). In follow-up work by Yim and Chopra (1985), the model was extended to a MDOF system supported on a two-spring dashpot system. The selected system of base supports is shown in Figure 4.3. In each of these studies, the individual spring elements were considered

linear elastic. The resulting moment-rotation envelopes response with different base idealizations are shown in Figure 4.4. A primary conclusion from this work was that foundation flexibility and uplift has little effect on higher modes of vibration, and for a multi-story building structure, these effects can be incorporated only by inclusion in the fundamental mode of response. In the SDOF study, the authors develop simplified expressions for determining the base shear resistance of flexible structures allowed to uplift.

Nakaki and Hart (1987) used discretely placed vertical elastic springs with viscous dampers at the base of a shear wall structure to illustrate the benefits of uplifting of the foundation supporting shear wall systems during earthquake loading. The Winkler springs had zero tension capacity and provided only elastic compressive resistance. The inelastic shear-wall structure was modeled using a nonlinear stiffness degrading hysteretic model. Figure 4.5 shows the schematic of the base spring configuration and the structural model considered. Nonlinear time history analyses were performed on this system considering two different ground motions: (1) a long duration motion from the 1940 El Centro earthquake and (2) a short impulsive-type motion measured at Pacoima Dam. Important findings from this study included the illustration through the numerical results that uplifting of the foundation results in a significant reduction in structural ductility demands when the rocking system has a longer period than that of the fixed base system, as shown in Figure 4.6. It was also observed that the frequency content of the ground motion has a significant effect on the system ductility demand. In addition, in select cases, allowing uplift of the foundation caused greater ductility demands on the structure.

Although through numerical Winkler-based foundation modeling these studies and others were able to reasonably capture the dissipation of energy, few previous works have focused on capturing the ramifications of this. The associated accrued settlement through the cumulative strain development within the soil near to the foundation is an important part of the overall performance-based design of the structure with consideration of the soil-structure system.

#### **4.2.2 Case Studies**

Several interesting case studies have used Winkler-based modeling to better capture structural response, as measured during earthquake events. For example, Rutenberg et al. (1982) presents an analytical study of the response of the Veterans Administration Hospital Building subjected to the 1971 San Fernando Earthquake. Foundation modeling was incorporated using a distributed

nonlinear Winkler spring system. The primary conclusion from this analysis was that the structure performed well in part due to the unanticipated benefits of the nonlinear soil-structure interaction.

Similarly, Wallace et al. (1990) present a case study comparing the numerical and measured response of two shear-wall-type buildings, one subjected to the 1984 Morgan Hill earthquake and the other to the 1987 Whittier earthquake. These structures were instrumented as part of the California Strong Motion Instrumentation Program (CSMIP). Foundation compliance was modeled using ATC 3-06 elastic spring concepts. Poor correlations between measured response and computed response were observed when soil flexibility was ignored in the modeling.

#### **4.2.3 Observations from the Literature Review**

From the previous literature review, it appears there are a number of opportunities and challenges in providing for a suitable base foundation model to capture the shallow foundation rocking behavior. With respect to the Winkler-based approach, issues of model discretization, material model selection, the geometric and loading details, and perhaps the numerical solution scheme, to name a few, become very important. The level of rigor applied and the evaluation of the overall robustness of the numerical model require proper balance in estimation of the important performance measures of the rocking shallow foundation, such as the monotonic and cyclic moment capacity, rotational demand at the base, associated inelastic deformation of the structure, and the cyclic and permanent settlement of the foundation. Each of these parameters is evaluated in the context of the Winkler-based numerical modeling approach in subsequent sections.

### **4.3 OPENSEES IMPLEMENTATION**

The implementation of a Winkler-model for studying these issues has been implemented into the OpenSees (Open System for Earthquake Engineering Simulation <http://opensees.berkeley.edu/>) platform. OpenSees is an open-source numerical modeling platform being developed by the Pacific Earthquake Engineering Research Center (PEER). A variety of elements and material libraries are available as well as a number of solution algorithms implemented for programmers,

developers, and users. The approach adopted is to study the applicability of using the materials and element models readily available in OpenSees. First, suitable material models were considered and subsequently various representative numerical models are constructed of the various physical models reported in the literature, and a best approximation of the measured response is attempted.

#### 4.3.1 One-Dimensional Material Response

A variety of uniaxial material models currently available in OpenSees were evaluated for their applicability to model the shallow-foundation soil-structure interaction, including the effects of uplift. Elastic-perfectly-plastic materials, gap materials, and combinations of general materials are combined with parallel materials, generally hysteretic materials, and a `qzsimple1` material developed by Boulanger et al. (1999). Three observed physical aspects are particularly important to capturing the overall response of the rocking shallow foundation and must be represented in the Winkler-mesh: (1) the footing may uplift on the opposing loading side, (2) soil beneath the footing may yield, and (3) upon continued reversal of loading, settlement may accrue below the foundation. These properties should be represented in the individual material element response.

The *elastic-perfectly-plastic* (EPP) material linearly follows an elastic tangent defined by Young's Modulus  $E$ . At a specified yield strain the material enters the plastic state where further deformations are sustained without an increase in stress. The unloading stiffness is identical to the original loading stiffness. Different yield strains may be assumed in tension and compression. However, the material does not retain permanent deformations and thus may not capture accrued settlements below a rocking foundation. The *elastic-perfectly-plastic-gap* material follows the same behavior as the *elastic-perfectly-plastic* material, with the exception of a defined gap placed in parallel with the EPP response. The gap offsets the starting point of the material behavior beginning with a certain amount of material strain; thus this would be suitable for capturing uplifting on the load reversal side of the foundation. However, this material also does not have strain growth features, which is important for accrued settlement.

A *general hysteretic* material is available, whereby the user specifies two to three points on the compression and tension backbones in order to define a bilinear or trilinear compression and tension backbone curves, respectively. Options are available to define pinching of the hysteresis in the x- or y-direction, damage due to ductility, damage due to energy dissipation, and

degraded unloading stiffness based on ductility. The generalized form of this material is shown in Figure 4.7(a). Combining multiple materials in parallel, as shown in Figure 4.7(b), provides useful for capturing any generalized backbone response. The generality of this material allows one to capture gap growth features as well.

The `qzsimple1` material was recently implemented into OpenSees based on the formulation described in Boulanger et al. (1999). Although this material was implemented to model the behavior of a pile tip under cyclic loading, the mechanisms of local response below the shallow foundation are quite similar. For example, under cyclic loading, the material does not reload until the strain reaches the previous cycle's unloading strain. In this sense the material has a gap that grows with each cycle, such that settlement is cumulative. The element utilizes an elastic, plastic, and gap component in series as generally shown in Figure 4.2. Radiation damping may be modeled through a dashpot placed across the element, where the force in the dashpot is only determined based on the elastic component to avoid excessively large damping forces. The behavior modeled either follows Reese and O'Neill's (1987) relation for drilled shafts in clay or Vijayvergiya's (1977) relation for piles in sand. The material is used with one-dimensional zero-length elements. The inputs to this material are the type of material, clay (1) or sand (2), the ultimate load capacity,  $q_{ult}$ , the displacement at which 50% of the ultimate load is mobilized,  $z_{50}$ , the amount of suction (tension capacity), *suction*, and viscous damping,  $c$ .

The `qzsimple1` material, however, may not be readily found in other platforms, although one may easily reproduce the characteristic curve by placing several general hysteretic materials in parallel. The material behavior of both the parallel hysteretic material and the `qzsimple1` material applied to a single-zero-length, one-dimensional element and subjected to ramped sinusoidal displacement are shown in Figure 4.8. Perhaps the most visible difference between the two materials is the compression unloading, near the transition toward tension mobilization. At this interface, the parallel hysteretic material unloads only until approximately zero strength, while the `qzsimple1` material unloads until mobilization of nominal tension capacity. The former would imply a material with zero resistance through a range of strain accumulation. The latter is more representative of the backside suctioning that immediately occurs upon compression unloading due to the adherence of the soil to the foundation element. The `qzsimple1` material also preserves a slight hardening in tension, whereas the current form of the parallel hysteretic material does not. The advantage of the hysteretic material is its ease of implementation in

design within readily available analysis platforms (e.g., Drain, Perform, etc.). Given their similar nature, the qzsimple1 material is used throughout these analyses.

### **4.3.2 Determination of Winkler Spring Properties**

The primary parameters to be determined for the system of springs below the foundation are the stiffness, ultimate bearing capacity, and the strain at yielding. More specifically, however, it will be important to determine the appropriate distribution of stiffness and bearing below the foundation to individual springs, since this will influence the response of the system as a whole. The following sections address the selection of stiffness of the system for consideration in Winkler spring systems.

#### ***4.3.2.1 Vertical and Rotational Spring Stiffness***

Stiffness of the Winkler springs is an important characteristic of the material model that must be specified to a reasonable degree of accuracy. In this case, both the vertical and rotational stiffness of the shallow foundation system are investigated using experimental data and equations available in the literature. In the Winkler framework, vertical stiffness of the system may be subdivided into individual spring contributions, whereas contributions to rotational stiffness will be provided only through varying vertical spring elements properties. For example, allowing larger magnitude (and finer distribution) of end springs, as shown in Figure 4.11.

Vertical monotonic compression tests were conducted by Rosebrook and Kutter (2001a–c), Negro et al. (1998), and Bartlett (1976) in conjunction with the lateral load experiments in each test series. Load-settlement curves from these experiments provide an indication of the range of vertical stiffness provided by the various foundation configurations. In this case, a minimum and maximum (apparent elastic) stiffness  $K_v$ -min and  $K_v$ -max was estimated assuming an elasto-plastic (EP) idealization of the system. Figure 4.9 illustrates the approach adopted, whereby the area of the experimental response is preserved in either estimation of  $K_v$ -min or  $K_v$ -max. These maximum and minimum (apparent) stiffnesses were then compared with recommendations by Gazetas (1991), using best estimates of soil parameters from the experimental datasets and based on cumulative data available in EPRI (1993). Figure 4.10(a) shows the vertical stiffness determined either experimentally or using equations by Gazetas

(1991). Although the scatter in the data is fairly large, and Figure 4.10 is shown on a logarithmic scale, the average of the trend-lines of the normalized stiffness estimates Figure 4.10(b) suggest that  $K_v$  based on Gazetas equations are between 2.0 and 0.2 that estimated from the experimental data using a simple EP assumption. This range of values is certainly reasonable considering the difficulty in estimating soil properties and the generalized EP assumption. In addition, the  $K_v$  estimate based on Gazetas is conservative (resulting in overestimation of settlement if  $K_{v-max} < K_{v-Gazetas}$ ) as the design vertical factor of safety increases.

The rotational stiffness may be implicitly provided by either varying the load-deflection characteristics of the individual springs along the length or providing variations in the vertical stiffness of the laterally placed springs. One strategy is to provide a varying bearing-capacity distribution; however, this applies only if the full foundation bearing is mobilized. Alternatively, a varying magnitude of stiffness and distribution of the individual spring elements may be provided. The latter is suggested in ATC-40 as shown in Figure 4.11, where the end stiffness is suggested as approximately nine times that of the middle region stiffness. This approach was adopted in these numerical simulations, using suggested middle and end stiffness values and tighter spring spacing in the end region in which stiffness is increased, as shown in Figure 4.11. The degree of coupling between vertical and rotational stiffness is also important and may be approximated in the Winkler framework by providing larger or smaller end regions.

#### ***4.3.2.2 Ultimate Bearing Capacity***

In select experiments, vertical bearing (compression) experiments were conducted to failure, providing an indication of the ultimate vertical bearing capacity of the system. In this case, these values were input directly into the mesh generator and subsequently distributed based on the selected pressure distribution to individual springs. For experimental studies without this available data, estimates of ultimate bearing capacity were made using Terzaghi's conventional bearing-capacity theory, considering seismic reductions to account for load inclination and eccentricity on the foundation based on the methods of Paolucci and Pecker (1997) and Richards et al. (1993).

### 4.3.3 Model and Simulation Details

Winkler-based capabilities were studied using the OpenSees platform and available elements and material models discussed. In each of the following cases described, the shallow foundation experimental prototype was modeled using elastic beam-column elements to represent the structural foundation and the shear wall or column extension above ground level. A series of one-dimensional zero-length springs, with material properties as described in Section 4.3.1, were placed below the elastic foundation element at discretely spaced intervals. To allow us to efficiently study various parameters, the distribution of properties (stiffness, strength, and strain levels) is controlled by a mesh generator (described in Section 4.3.4). In select cases, a single spring was placed horizontally at the end of the Winkler-system to model any sliding observed during the experiments. The selected spring element consisted of a nonlinear p-y element (Boulangier et al. 1999) with gap capabilities placed in parallel with a low stiffness (2% of the elastic stiffness of the p-y element) elastic spring to allow for nominal post-yield hardening of the sliding response.

The precession of loading closely followed that reported by experimental investigators. Accurate modeling of the precompression to these systems is critical to subsequently accounting for the induced rocking settlements. Compression load iteration was conducted prior to application of lateral cyclic or monotonic rocking loads to ensure that the state of deformation below the foundation was compatible to that of the experiment at the time of loading. Iteration was conducted until a precompression settlement was obtained within 0.1% of that measured. Subsequently, displacement-controlled cyclic or monotonic loading was applied at the same point in the numerical model as in the physical experiments. Generally, this was applied to a rigid link at some point above the shallow foundation to produce a moment and, upon yielding of the foundation, caused rotation of the system. Both Newton and linear solution algorithms were investigated for solving the pseudo-time step system of equations. In general, the linear solution algorithm with 100 pseudo-time steps each loading increment resulted in a stable solution for the cases considered. Solution convergence was controlled within a tolerance of  $1e-12$  over a maximum of 30 iterations.

#### 4.3.4 *BNWFShallow* Mesh Generator

A mesh generator *BNWFShallow* is used to study the sensitivity of the Winkler model parameters for capturing the salient features of the rocking strip foundation. Currently, *BNWFShallow* is implemented in the TCL scripting language, which wraps the OpenSees platform. *BNWFShallow* allows the user to consider different: (1) lateral spring distributions, (2) bearing pressure distributions, and (3) variable material models and model parameters.

##### 4.3.4.1 *Lateral Spring Distribution*

Base spring lateral distributions of interest include both the number of springs (as a function of the footing length), the type of spacing of the springs, and the stiffness of the different springs. A nonuniform lateral distribution is suggested in ATC-40 (1996) and utilizes closer spacing at the ends to compensate for the heavily loaded edges of the footing, which may cause more densification at the edges. In *BNWFShallow*, the user can specify either uniformly distributed spring spacing or variable spring spacing along the length of the foundation, as shown in Figure 4.12. For the variable spring spacing, a distribution symmetric about the centerline of the footing element is assumed. Using this option, the user specifies the middle region length percentage ( $L_{mp}$ ) as a percentage of the entire footing length ( $L$ ). End and middle spring spacing and stiffness can then be independently specified using the variables:

1. Middle Length Ratio, ( $r_{atom}$ ) — This value specifies the length ratio in the middle region of the foundation, defined as the value of the length between nodes divided by the length of the middle region ( $L_{mp} * L$ ).
2. End Length Ratio, ( $r_{atioe}$ ) — This value specifies the length ratio in the end region of the foundation, defined as the value of the length between nodes divided by the length of one end of the foundation outside of the middle region ( $[(1 - L_{mp}) * L] / 2$ ).
3. Variable End Stiffness, ( $K_{ep}$ ) — This percentage is a multiplier for the stiffness value of springs outside the middle region defined above. This value is most likely greater than one.
4. Variable Middle Stiffness, ( $K_{mp}$ ) — This percentage is a multiplier for the stiffness value of springs inside the middle region defined above.

#### 4.3.4.2 Bearing Pressure Distribution

Applying the Winkler-based approach, perhaps the most important parameter for accurately modeling the system is the contact pressure distribution. This variation will depend upon the flexibility of the foundation and the nature of the soil below the foundation. Therefore, in the mesh generator, the user can specify different bearing pressure distributions to represent the ultimate soil capacity approximated by the Winkler spring system. The different distributions, uniform, triangular, trapezoidal, and parabolic are termed Types I–V (Fig. 4.13).

Other variables available for input into *BNWFShallow* include the end tip resistance of the spring system,  $q_i$ , the suction (suction or TP), and the initial pre-compression ( $i_d$ ). The tip resistance,  $q_i$ , defines the amount of soil pressure to be placed at the ends (last springs) of the bearing pressure distribution shown in Figure 4.13, for a non-uniform distribution. The mesh generator then calculates the curve of the distribution such that the system still retains the global bearing capacity similar to the uniform distribution. The suction (suction and TP variables) defines the amount of ultimate tension capacity of the individual springs. The variable “suction” is used to define this value for the q-z material, while the variable TP defines this value for the parallel hysteretic material. Initial pre-compression  $i_d$  is the value of settlement accrued prior to cyclic loading. For comparison with centrifuge experimental data this includes the settlement accrued during spin up (from 1–20g for example) and any tests not modeled in the sequence up to the current test. For application in numerical simulations where the history of the soil is not known, estimations using conventional settlement calculations were applied.

#### 4.3.5 Experimental-Numerical Comparisons in OpenSees

A number of available experimental datasets were modeled using the mesh generator described in the previous section. The primary objective was to observe the cyclic moment-rotation response of the shallow rocking foundation, while attempting to reasonably capture accrued settlements of the system. Datasets from 1g and centrifuge experiments were modeled, including foundations resting on sand and clay with a range of design vertical factors of safety. Results from select numerical studies are discussed in the following sections. The model parameters of each of the tests presented in this section are listed in Table 4.1. In each analysis described,

prototype scale numerical models were constructed and soil properties were estimated from the available data and using approaches described in Section 4.3.1.

#### ***4.3.5.1 Centrifuge Experiments***

Recent centrifuge experiments by Rosebrock and Kutter (2001a, b, c) [also summarized in Rosebrock 2001] incorporate a range of footing sizes, design vertical factors of safety (from  $FS_v = 1.6$ – $6.2$ ), and both clay and sand soil types. In these experiments, series KRR01 and KRR02 consider sandy soils, while series KRR03 considers systems resting on clayey soils. Select details of these experiments may be found in Chapter 3. The general displacement history applied to both the KRR02 and KRR03 series experiments consists of between three and six cycles of symmetric reversed cyclic loading each to a target constant displacement followed by increasing (typically by 50% or 100%) of the loading amplitude and application of another series of reversed cycles of constant amplitude.

The KRR02 series includes quasi-static lateral cyclic loading applied to a model rigid foundation and shear-wall system resting on dry Nevada sand ( $Dr=60\%$ ). Two simulations are presented for the KRR02 series results, and are denoted KRR02-S21 and KRR02-S38 for small and large footing, respectively. The design vertical factor of safety for these experiments was  $FS_v = 3.0$  and  $6.2$ , for the S21 and S38 series, respectively. The S21 series encompasses loading accrued from test series S21 through S35, resulting in three cycles to each of six amplitudes. Prior to this, the model specimen was subjected to two cycles of spin-up/spin-down in gravitational forces from 1–20g. Accrued pre-compressions were applied to the numerical model based on measurements taken during these test series (S14-S20). The S38 series encompasses loading accrued from test series S38 through S50, resulting in three cycles to each of seven amplitudes. Prior to this, the model specimen was subjected to one spin-up cycle from 1–20g. Accrued pre-compressions were applied to the numerical model based on measurements taken during this test series (S37).

The KRR03 series includes quasi-static lateral cyclic loading applied to a model rigid foundation and shear-wall system resting on stiff saturated clay. A simulation result from the KRR03-S18 (small footing) is provided (Figs. 4.15–4.16). The design vertical factor of safety for this experiment was  $FS_v = 2.8$ . The S18 series encompasses loading accrued from test series S18–S27, resulting in six cycles to each of five amplitudes. Prior to this, the model specimen was

subjected to one spin-up cycle from 1–20g and a period of consolidation in-flight. Measured settlement data were not collected during these series; thus estimates of settlement due to primary consolidation were applied to the model to preload the system.

Prototype footing sizes and soil properties for these specimens are listed in Table 4.1. For the KRR02 experiments, a friction angle of  $38^\circ$  was back-calculated from theoretical vertical bearing-capacity theory using vertical compression data for the small footing (compression tests were not performed for the larger footing). Estimation of the shear strength of clay ( $c_u = 103$  kPa) for the KRR03 experiments were based on review of Torvane measurements, sample compression tests, and bearing experiments, as described in Chapter 3.

Moment-rotation and settlement-rotation simulation results for the footings on sand (KRR02) series shown in Figures 4.14 and 4.15 generally match the experimentally measured response fairly well. Each of these numerical simulations generally captures the maximum moment response fairly well, including the increasing moment strength with increasing amplitudes of rotation observed in the experiments. In addition, the unloading and reloading of the hysteretic moment-rotation response, which provides for capturing the energy dissipation of the system is captured by the Winkler mesh generator. The general settlement response in part (b) of Figures 4.14 and 4.15 show that the upturned (“U”) shape upon increasing cyclic rotation amplitude is captured, though this shape is much less pronounced for the smaller footing with a lower factor of safety ( $F_{Sv}=3.0$ ). For the larger footing (Fig. 4.15), with a larger design factor of safety ( $F_{Sv}=6.2$ ), however, the simulation results overpredict the final accrued settlement by approximately 20%. Also shown in (c) is the lateral base displacement–pseudo time history of this simulation. In this case, a small amount of sliding is accrued in the final cycles, and appears in the nonsymmetric lateral base displacement history in select cycles. The nonlinear spring element with gap capabilities placed horizontally tends to overpredict the magnitude of this sliding displacement during certain cycles of loading, which may lead to the underestimation of moment resistance.

The moment-rotation simulation results for the footings on clay (KRR03) series, shown in Figure 4.16(a) generally match the experimentally measured response fairly well. The simulated permanent settlement of the system are within 5% of measured values ( $S_{\max(\text{exp})} = 345$  mm). The shape of the settlement response as shown in Figure 4.16(b) also results in the highly U-shaped deformation resulting from the stiff ends of the footing, and the limited rounding is generally matched with the numerical simulations. In addition, the moment-rotation response in

the numerical simulations is more “pinched” than that measured, leading to an underestimation of rotational energy dissipation.

#### ***4.3.5.2 One-g Experiments***

##### ***4.3.5.2.1 ELSA Laboratory Experiments***

One-g experiments were recently completed at ELSA (European Laboratory for Structural Assessment) in Italy. The results from these experiments are reported in Negro et al. (1998) and Faccioli et al. (2001). The system considered consisted of a 1m-sq foundation placed on a saturated Ticino sand base subjected to static vertical, static cyclic, and dynamic seismic lateral displacements. Two relative densities were considered in these experiments,  $D_r = 85\%$  and  $45\%$ . A constant vertical load is sustained by an air cushion system throughout the test, at 300 kN for the high-density test and 100 kN for the low-density test. This equates to an approximate design vertical factor of safety of 5.0 and 2.0, for the high-density and low-density cases, respectively. Rotation, applied to the foundation through a hydraulic actuator placed 0.9 m above the foundation, consists of single reversed (symmetric) cycles of increasing amplitude.

Figure 4.17 shows the moment-rotation (a), settlement-rotation (b), and lateral base displacement–pseudo time (c) response of this experiment, compared with simulated results using the BNWF mesh generator. While the general shape of the moment-rotation response is preserved by the numerical model there appears to be a measured nonsymmetry in the footing response, which might be attributed to the nonsymmetric sliding occurring [Fig. 4.17(c)]. The Winkler mesh approach underestimates the maximum permanent sliding displacement by approximately 60%. The numerical simulation does not capture this effect, though the shape of the hysteresis given the parameters selected appear reasonable. The permanent and cyclic settlement of the system is fairly well captured by the model. An underestimation in cumulative settlement of approximately 10% is observed.

##### ***4.3.5.2.2 New Zealand Experiments***

Model footing experiments were conducted at the University of New Zealand. The focus of these experiments was to investigate the nonlinearity developed in the soil and the uplift at the

interface of the soil and footing upon large-amplitude moment loading. The results are described in Taylor et al. (1981), Weissing (1979) and Bartlett (1976). Studies by Weissing (1979) considered the rocking response of foundations resting on dry sand, while studies by Bartlett (1976) considered foundations resting on clay. In these experiments, horizontal movement of the footing was restrained through the use of a steel tie-rod system. Each experiment consisted of five loading cycles to each of three increasing amplitude levels. Only the first, second, and fifth loading cycles from these experiments were simulated due to limited available data.

Figures 4.18(a)–(c) summarize experimental-numerical comparisons to select results conducted by Weissing (1979). A common footing element is used in these experiments, and as noted in Table 4.1, the Type A footings [(a) and (b)] denote rocking response about the strong axis of rotation of the footing (which is 2:1 in plan dimensions), while Type B footing denotes rocking response about the weak axis of rotation of the footing (c). The response results shown in these figures illustrate good correlation between the numerical results (both in moment rotation and settlement rotation) and the experimental results. Comparisons of accrued settlements for the Type B footing [Figure 4.18 (a) and (b)] are overestimated by 10% and 20% for the low and high FS<sub>v</sub>. Response of the Type B footing [Figure 4.18(c)] is fairly poorly matched with the Winkler approach. This system is perhaps better modeled using a two-dimensional array of nonlinear springs to better spread the nonlinear resistance below the long axis of the foundation.

Figures 4.19 and 4.20 summarize the experimental-numerical comparisons of the model specimens resting on clay and tested by Bartlett (1976). In general, clay specimens are observed to have a more pinched hysteretic response resulting in potential numerical convergence issues. Although these simulations shown are fairly reasonable in terms of capturing the desirable salient features of response, careful selection of the various properties in the mesh generator were required to come to a stable numerical solution convergence. This may be due in part to the low magnitudes of deformation applied to the system as a whole. It should be noted that the experimental settlement shown in Figure 4.19(b) was reported by Bartlett only for the later loading cycles. The location of initial settlement was set at the numerically determined settlement for this comparison.

## 4.4 SENSITIVITY STUDY AND DISCUSSION OF RESULTS

Appropriately capturing both the moment-rotation response and settlement-rotation response of the above systems provides the challenge of balancing between appropriate selection of strength (bearing pressure) and stiffness (both vertical and rotational) properties. In these simulations, an effort was taken to best capture both the moment capacity and accrued settlement by studying the general range of the mesh generator parameters. Using the mesh generator to efficiently vary parameters such as the end tip resistance, the length of the middle region, the amount of suction and the assumed bearing and stiffness (based on conventional theory) was the focus of the numerical simulations. Observing Table 4.1 the parameters, which provided the best-case simulation comparisons (described in the previous sections) are provided. In this case, modified strength or stiffness values were provided above conventionally predicted values. These factors are represented in Table 4.1 by the variables  $F_Q$ ,  $F_{K_m}$ , and  $F_{K_e}$ , where  $F_Q$  is applied uniformly across the foundation to the estimated ultimate bearing capacity (using either bearing capacity determined experimentally, if available, or using Terzaghi's bearing-capacity equations),  $F_{K_m}$  is a uniform modification applied to the stiffness of springs within the middle region of the Winkler mesh, and  $F_{K_e}$  is a uniform modification applied to the stiffness of springs within the end regions of the Winkler mesh. Parameter selection and the effects of varying their magnitude are discussed in subsequent sections. In this case, the K2S21 series data were selected for parameter variation — with a  $FS_v = 3.0$ , resting on a medium sand, this footing was felt most representative of many practical field conditions.

### 4.4.1 Bearing-Capacity Distribution and Magnitude

The range of tip resistance required at the ends of springs  $q_i$  suggests that a highly parabolic to inverse parabolic distribution is appropriate for capturing the rocking response of these systems. From the analyses summarized, it appears that foundations resting on dry sand, with the exception of K2S38, generally require an end tip resistance of less than  $q_i = 0.5$ . For those foundations resting on saturated sand or clay (T83 and K3S18, respectively), an inverse parabolic ( $q_i > 1.0$ ) shape appears most appropriate. Bartlett (1979) simulation comparisons provide the exception, with  $q_i = 0.5$  best matching experimental response. However, these experiments were conducted at fairly low confining stresses, and it may be difficult to generalize

regarding their required pressure distribution. Observing sensitivity studies varying the end tip resistance for the KRR02-S21 series data (Fig. 4.14), the range of end tip resistance from 100–10% (Fig. 4.21) suggests a uniform pressure distribution overestimates both moment resistance and permanent settlement. However, a highly parabolic distribution ( $q_i = 0.1$ ) resulted in an underestimation of both moment and permanent settlement. The selected distribution also changes the unloading rotational stiffness of the system, as observed in Figure 4.21(a).

Selection of the appropriate magnitude of compressive resistance for the Winkler mesh resulted in reductions applied to the estimated ultimate bearing pressure by a factor  $F_Q$  ranging from 0.5–2.0, as listed in Table 4.2. This range is reasonable given the uncertainty in estimating the capacity of the footing. As expected, the model is highly sensitive to the magnitude of bearing capacity distributed among the Winkler mesh. Figure 4.22 shows numerical envelopes of the moment-rotation response where the best-case bearing-capacity factor ( $F_Q = 0.6$ ) is scaled up and down by a factor of 2.0. An underestimation in qult (one half of best-case value) results in a nearly unstable solution and approximately a one-third reduction in estimation of moment resistance and comparable overestimation in permanent settlements (60% overestimation).

#### 4.4.2 Spring Stiffness

As mentioned, the magnitude of the end springs for these simulations was increased based on recommendations by ATC-40 (shown in Fig. 4.11). It is observed that the length over which this stiffness is increased,  $L_{ep}$ , will have a more pronounced effect on the shape of the cyclic settlement response. For those simulations examples described,  $L_{ep}$  ranged from 10-25% of the length of the footing. Lower  $L_{ep}$  values (10%) were required for lower  $FS_v$  ( $FS_v=2.0$  in this case, for T83 and Weissing Type A footing-low  $FS_v$ , shown in Figs. 4.17 and 4.18, respectively). Settlement response for the looser material was observed to be flatter during cyclic rotation [parts (b)]. Higher  $L_{ep}$  values (25%) were required for the very stiff clay case (K3S18, shown in Figure 4.16) to compensate for the highly U-shaped settlement-rotation response. Figure 4.23 shows the variation of  $L_{ep}$  from 0.1, 0.2, and 0.3 for test series K2S21. These results indicate the moment-rotation response is less sensitive to the value of  $L_{ep}$  selected.

The selected magnitude of initial stiffness for the Winkler springs will also result in highly varying response results. From the analyses results discussed, the variation in end and middle stiffness magnitudes from theoretical calculations (based on Gazetas' formula) were in

general modified by between 0.1–2.0 ( $F_{km}$  and  $F_{ke}$  values in Table 4.2). Select cases did require substantially larger amplification of originally estimated stiffnesses (Weissing 1979 and Bartlett 1976). Figure 4.24 shows the resulting response providing a uniform change to the best-case stiffnesses of all springs across the foundation (middle and end) up and down by a factor  $F_k = 2.0$ . Although softer springs are provided ( $F_k = 0.5$ ), this may not necessarily result in less permanent settlement, as seen in Figure 4.24(b), since the moment resistance provided by the foundation has been reduced.

#### **4.4.3 Tension Capacity**

The magnitude of tension capacity provided in each Winkler spring element was held constant along the length of the mesh. The cases described in Figures 4.14–4.20 resulted in suctions  $T_p$  varied between 1 and 10%. For the sand case at least, an increase in suction capacity was observed to only slightly increase the moment resistance of the foundation and had little effect on the permanent settlement of the footing as shown in Figure 4.24.

#### **4.4.4 Distribution of Springs**

Numerical-experimental comparisons provided in Figures 4.14–4.20 used a very fine mesh of Winkler springs distributed across the base of the foundation. For each of these simulations, a ratio of 0.02 was used, resulting in 151 springs in each case. It is instructive to observe the influence of the number of laterally placed springs on the numerical simulation results. Figure 4.26 shows a comparison of numerical-experimental moment-rotation envelopes and maximum settlements obtained for a coarse, medium-fine, and fine Winkler mesh of springs. While not immediately evident in the envelope of the response of the various numerical models, Figure 4.27 further shows the hysteresis response of the various mesh discretizations in (a)–(c). In this case, the staggered unloading and loading response and resulting change in moment-rotation energy dissipation is observed for the coarser mesh assumption. It should also be noted that for the coarser meshes studied, numerical instability is observed in the time-step solutions requiring finer iterations between displacement steps to solve the nonlinear equations.

## 4.5 ANALYSIS OF EXPERIMENTAL RESULTS

### 4.5.1 Energy Dissipation and Equivalent Viscous Damping

Soil-foundation interaction is highly nonlinear; the moment-rotation hysteresis curves display excellent ductility — good potential to dissipate energy that may otherwise damage the superstructure. A side effect of nonlinearity is the permanent settlement of the footing. As expected, the amount of settlement depends on the magnitude of the axial load and the cyclic rotation. Data available from experiments that isolate the nonlinear contributions of the foundation of a soil-structure system provide the opportunity to determine the energy that has been dissipated and the associated consequences of such energy dissipation. Such information will be valuable to the assessment of systems using nonlinear static procedures (NSPs), since many of these methods have their basis in the substitute structure approach. The substitute structure approach, diagrammatically shown in Figure 4.28, relies on idealizing the behavior of an inelastic system with that of an equivalent linear system using secant stiffness and equivalent viscous damping properties representative of the global behavior of the structure at an anticipated peak (or design) displacement level. Early works by Hudson (1965) and Jennings (1968) have provided the general approach. Subsequent modifications by Gulkan and Sozen (1974) describe the method applied to reinforced concrete frame structures. Kowalsky et al. (1995) describe a displacement-based design procedure for reinforced concrete bridge columns, which is based on the substitute structure method. Recent code procedures, for example ACT-40 (1996), adopt the approach in combination with the capacity spectrum approach (Freeman 1978) to provide an alternative design procedure for retrofit of reinforced concrete buildings.

To utilize the method in the context of the systems studied herein, the effective damping ratio versus demand relation needs to be determined for the rocking foundation system. The effective damping ratio  $\xi_{eff}$  is equivalent to the sum of the hysteretic damping of the system represented as an equivalent viscous damping term and a viscous damping component, i.e.,

$$\xi_{eff} = \xi_v + \xi_{eq} \quad (4.1)$$

The equivalent viscous damping may be determined by equating the energy dissipated in a vibrational cycle of the inelastic system with that of the equivalent linear system (Chopra 1995):

$$\xi_{eq} = \frac{1}{4\pi} \cdot \frac{E_D}{E_s} \quad (4.2)$$

where  $E_D$  = the hysteretic energy dissipated by the rocking shallow foundation system during one cycle of loading and  $E_s$  = the elastic strain energy associated with that cycle of motion, at a peak displacement. The hysteretic energy  $E_D$  for this system is a combination of the cyclic lateral and vertical translation and rocking energy, i.e.,

$$E_D = E_D^r + E_D^{LT} + E_D^{VT} = \int M(t) \cdot d\theta(t) + \int V(t) \cdot d\Delta_L(t) + \int P(t) \cdot d\Delta_T(t) \quad (4.3)$$

where  $E_D^r$  = energy associated with moment-rotational rocking,  $E_D^{LT}$  = energy associated with lateral translation, and  $E_D^{VT}$  = energy associated with vertical vibration. For this exercise, it is assumed that the rocking contribution to system energy dissipation dominates the calculation of  $E_D$ . The elastic strain energy (from Fig. 4.29) may be determined as:

$$E_s = \frac{M_{max} \cdot \theta_{max}}{2} \quad (4.4)$$

where  $M_{max}$  = the average maximum moment of the system and  $\theta_{max}$  = the associated maximum rotation.  $E_D$  and  $E_s$  may be determined, for example using the  $M$ - $\theta$  data shown in Figure 4.29, averaged over three cycles of uniform loading to the same target displacement level. The viscous damping ratio  $\xi_v$  in Equation 4-1 was kept constant at 2%.

Figure 4.30 shows the effective viscous damping versus the distortion (average settlement normalized by the foundation length) per cycle, where (a) shows data from sand experiments and (b) shows data from clay experiments. These data are shown for all experiments available with reversed cyclic static lateral loading (KRR series data, ELSA data, Bartlett 1976 and Weissing 1979 data). The results indicate that high levels of effective viscous damping are obtained within tolerable distortion levels (up to  $\xi_{eff} \sim 13\%$  for tolerable distortions for load-bearing walls).

Although limited data are available for  $FS_v < 3.0$ , the results in Figure 4.30(a) show that the trend line to the data for both high and low  $FS_v$  suggests similar  $\xi_{\text{eff}} - s/L$  values.

## **4.6 ADDITIONAL PLANS FOR THE STUDY**

### **4.6.1 Additional Available Experimental Datasets**

Experimental data recently conducted by Gajan and Kutter consider effects such as vertical cyclic loading and foundation embedment. Given these datasets, the Winkler-based mesh generator used in these studies may readily be evaluated for its applicability in modeling these systems. Other important areas for study include the variations in footing geometry and low shear-dominated loading and sensitivity of sliding on the modeling response.

### **4.6.2 Combined Nonlinear Structure and Soil-Interface Analysis**

Initial validation of the numerical models has led us to develop subsequent parametric studies that consider the combined dissipation of energy through nonlinearity in structural elements (e.g., in shear walls, at beam-column joints) and nonlinearity of foundation elements (through yielding of the soil). Parametric studies will consider moment-resisting frame (MRF) structures as well as coupled structural systems (MRFs and shear walls combined).

## **4.7 SUMMARY AND MAJOR FINDINGS**

A primary objective of this study is to contribute to the accurate numerical modeling of shallow rocking foundations using nonlinear Winkler-based approaches. To date, different experimental data have been collected and used to compare with the numerical solution predicted using a mesh of nonlinear Winkler springs and gap elements placed below the base of representative shallow footing systems. Data considered represent vertical factors of safety  $FS_v$  ranging from 1.5–6.2, including sand and clay and representing both 1g and 20g (centrifuge) experiments. Findings from the study to date include:

1. Reasonable comparison between the nonlinear Winkler-based approach and the experimental data selected can be obtained, provided proper selection of properties (stiffness, strength, etc.)

2. The moment-rotational ( $M-\theta$ ) response of foundations resting on clayey soils results in a more pinched behavior and a highly U-shaped settlement-rotation ( $s-\theta$ ) history. Given proper selection of the end spring resistance functions, this U-shaped behavior was captured. ATC-40 (1996) end spring amplifications reasonably account for the increased stiffness at the ends of the foundation, provided the proper length of the increased stiffness zone is selected.
3. The  $M-\theta$  and  $s-\theta$  responses using a Winkler mesh are most sensitive to the selection of bearing-pressure distribution and magnitude. A parabolic shape resulted in more reasonable comparisons for footings on sands, while an inverse parabolic (higher-end capacities) resulted in a more reasonable comparison with clay experimental results. The  $M-\theta$  and  $s-\theta$  responses using a Winkler mesh are least sensitive to magnitude of tension capacity provided in the springs
4. Overall, the response is highly sensitive to the amount of sliding occurring; though conservative estimates based on design interface friction angles were used, it may be that a more suitable estimate of interface friction is related to the critical state friction angle.
5. Analysis of these data investigating the hysteretic energy dissipated indicates high levels of energy dissipation with moderate consequences (settlement in this case).

**Table 4.1 Details of experimental-numerical specimen results presented**

Experiment Series	Reference	Soil Type	FS <sub>v</sub> <sup>1</sup>	Length L (m)	Width B (m)	Depth of Embedment D (m)	φ (°)	D <sub>r</sub> (%)	c <sub>u</sub> (kN/m <sup>2</sup> )
K2S21	Rosebrook and Kutter (2001b)	Sand	3.0 (φ = 38)	2.67	0.69	0	38	60	0
K2S38	Rosebrook and Kutter (2001b)	Sand	6.2	3.94	1.08	0	38	60	0
T83	Negro et al. (1998)	Saturated Sand (LD)	2.0 (φ = 35)	1.0	1.0	0	35	45	0
K3S18	Rosebrook and Kutter (2001c)	Clay	2.8	2.67	0.69	0.26	0	-	103
W-Type A (Low FS <sub>v</sub> )	Weissing (1979) <sup>2</sup>	Sand	2.0 (φ = 43)	0.5	0.25	0	43	93	0
W-Type A (High FS <sub>v</sub> )	Weissing (1979) <sup>2</sup>	Sand	5.0 (φ = 43)	0.5	0.25	0	43	93	0
W-Type B (High FS <sub>v</sub> )	Weissing (1979) <sup>2</sup>	Sand	5.0 (φ = 43)	0.25	0.5	0	43	93	0
B-Type B	Bartlett (1976) <sup>2</sup>	Clay	1.5	0.25	0.5	0	0	-	49
B-Type A	Bartlett (1976) <sup>2</sup>	Clay	3.0	0.5	0.25	0	0	-	49

<sup>1</sup> Determined either based on back-calculation from a given friction angle (φ used provided in parenthesis), as directly reported by authors, or from compression experiments, for KRR test series details, refer to Table 3.2.

<sup>2</sup> Also reported in Taylor et al. (1981)

**Table 4.2 Summary of BNWF simulation details for modeled experiments**

Experiment Series	qi (as % of Qu/L) <sup>1</sup>	Lep (as % L)	Suction (as % of Qu)	Lateral Spring k <sup>1</sup>	F <sub>Q</sub>	F <sub>Km</sub>	F <sub>Ke</sub>
K2S21	50	20	2.0	1/3 (alum)	0.6	2.0	2.0
K2S38	80	20	1.0	1/3 (alum)	0.6	0.2	0.1
T83	300	10	10.0	1/2 (conc)	1.0	0.3	0.1
K3S18	200	25	10.0	0.4 (clay)	0.5	2.0	2.0
W-Type A (Low FSv)	50	10	10.0	NA	1.3	0.5	0.5
W-Type A (High FSv)	40	15	1.0	NA	0.8	0.3	0.3
W-Type B (High FSv)	20	20	1.0	NA	1.0	10.0	15.0
B-Type B	50	20	1.0	NA	1.4	5.0	5.0
B-Type A	50	20	1.0	NA	2.0	5.0	5.0

<sup>1</sup> Where applicable, a lateral spring was defined with resistance proportional to  $Tan(k\phi)$ , for sand, or  $kc_u$ , for clay, where k is defined above based on the interface material. NA denotes experiments where sliding was restrained.

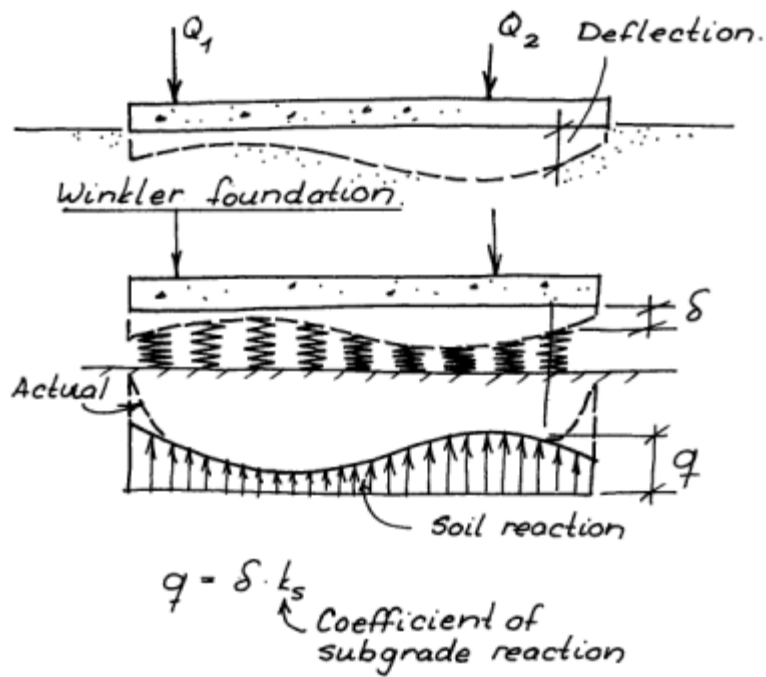


Fig. 4.1 Winkler foundation concepts (after Broms, 2003)

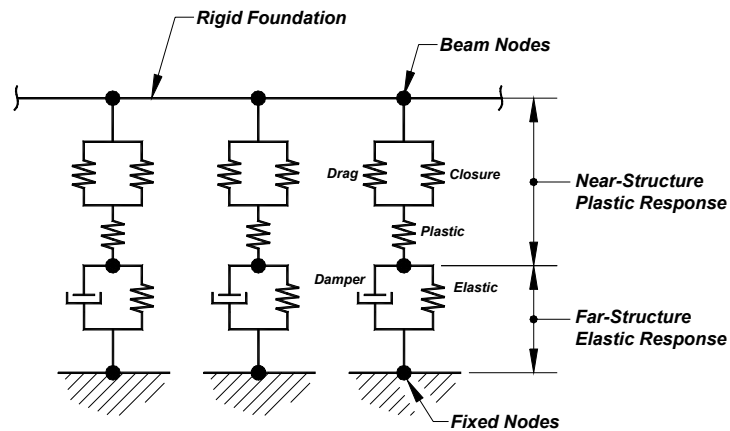


Fig. 4.2 Example series of Winkler springs below a rigid foundation represented by two-dimensional finite elements (after Boulanger et al. 1999)

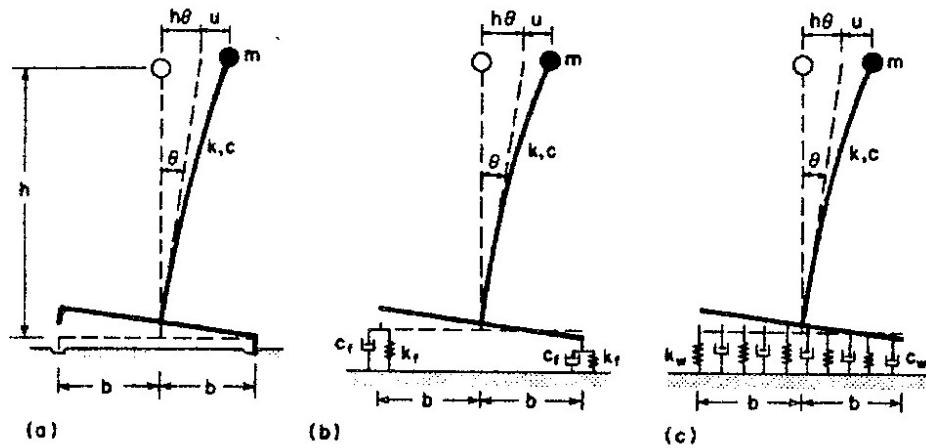


Fig. 4.3 Idealized foundation system by Chopra and Yim (1985): (a) rigid foundation, (b) two-element (spring-dashpot) system, and (c) distributed Winkler (spring-dashpot) system

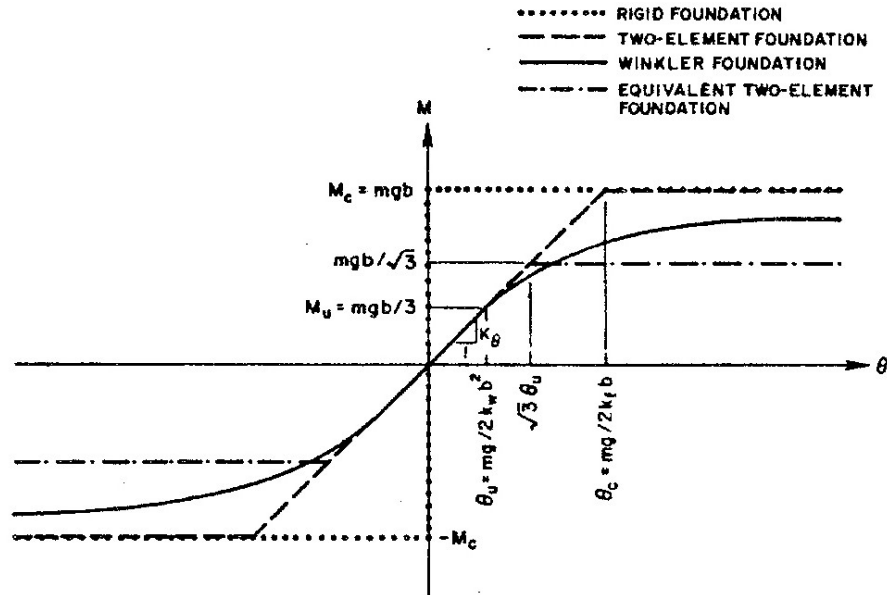


Fig. 4.4 Moment-rotation envelope assuming different idealized foundations (Chopra and Yim, 1985)

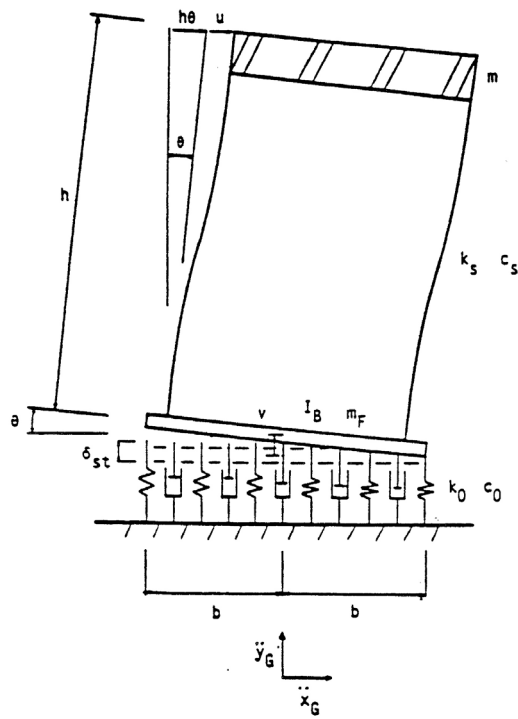


Fig. 4.5 Winkler-foundation system below a model inelastic shear wall (Nakaki and Hart 1987)

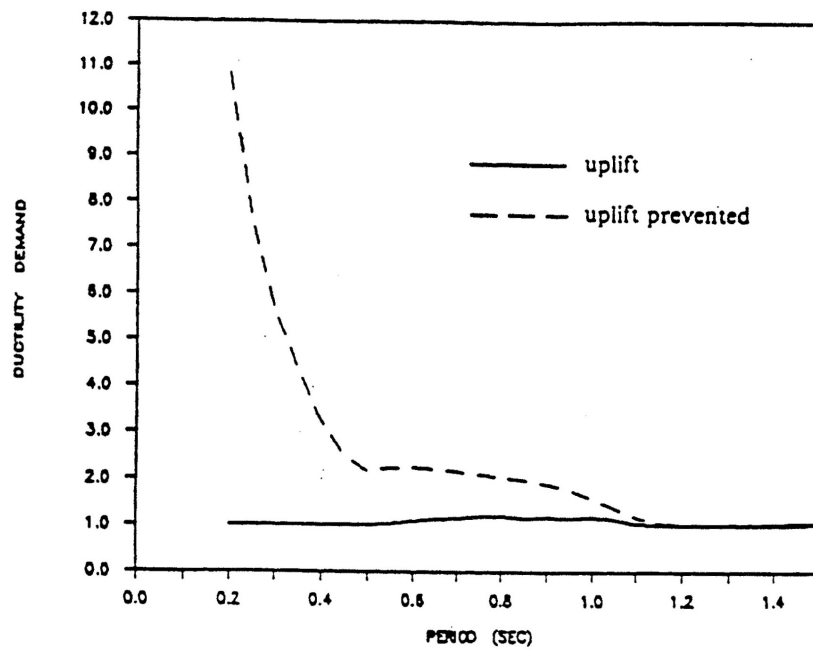


Fig. 4.6 Ductility demand versus period relation for structures allowing and preventing uplift (results from analyses using the El Centro earthquake) (Nakaki and Hart, 1987)

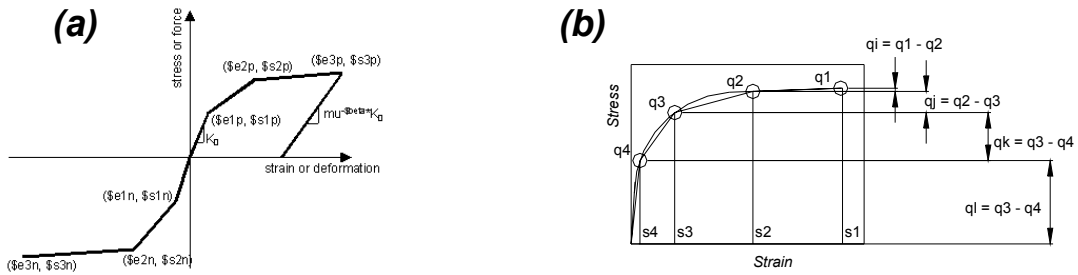


Fig. 4.7 Hysteretic material backbone curve: (a) single material and (b) multiple hysteretic material elements placed in parallel

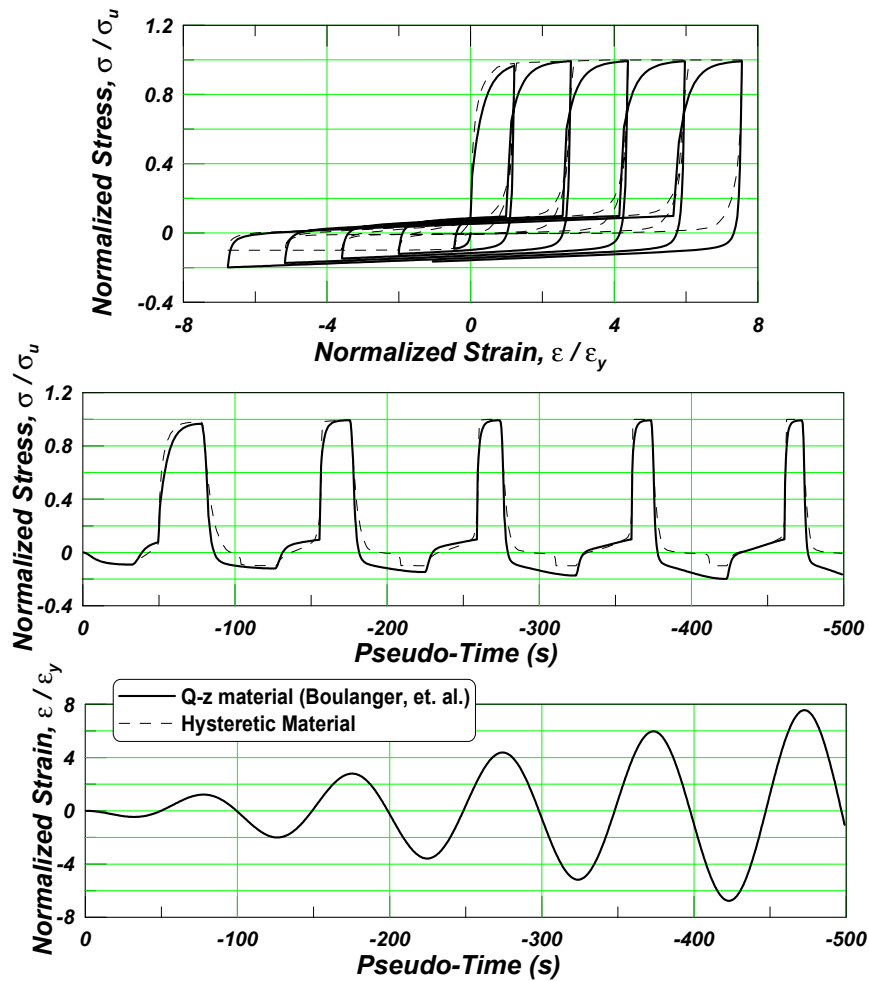


Fig. 4.8 Comparison of material response — single element parallel hysteretic and qzsimple1 material in OpenSees

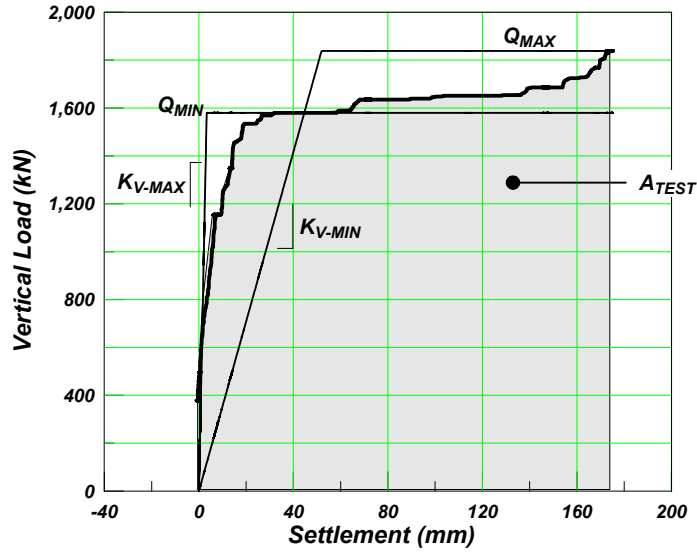


Fig. 4.9 Determination of maximum and minimum vertical (*apparent elastic*) stiffnesses based on elasto-plastic idealization of experimental data

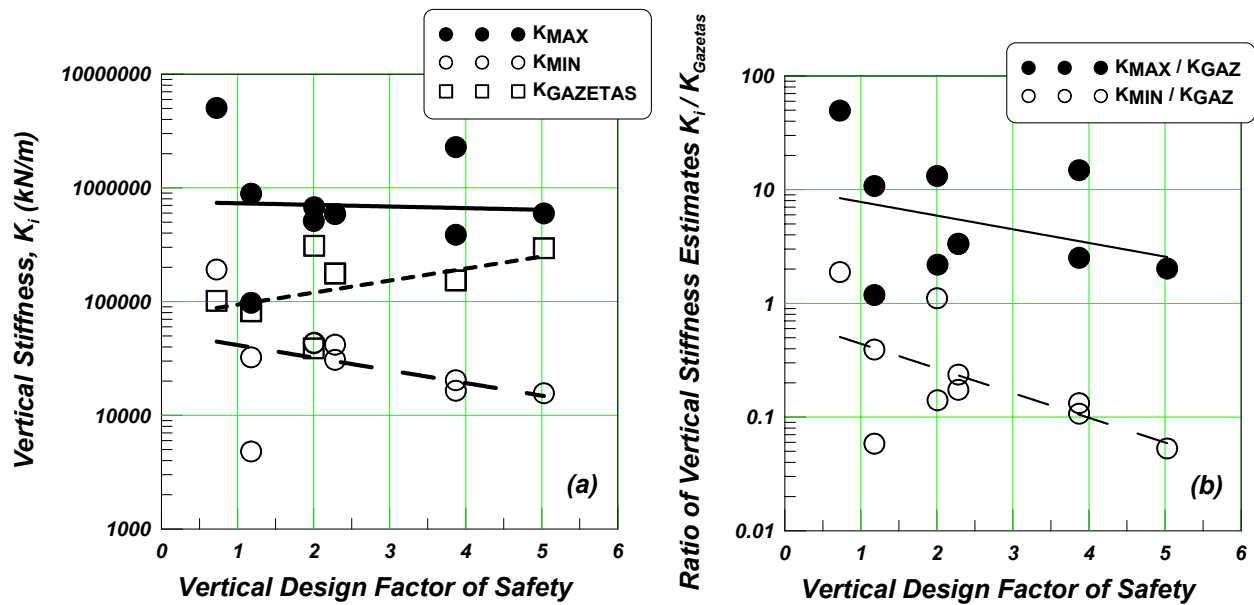
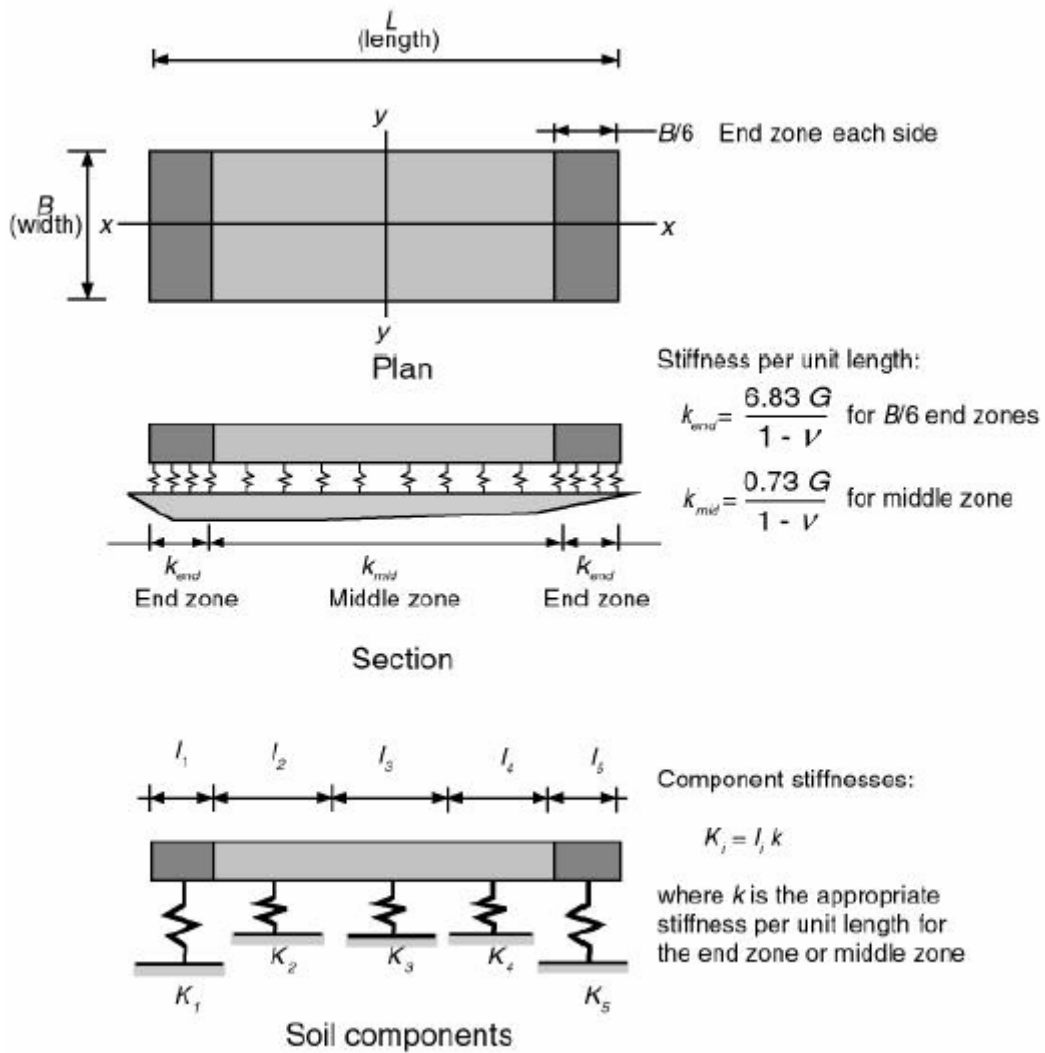
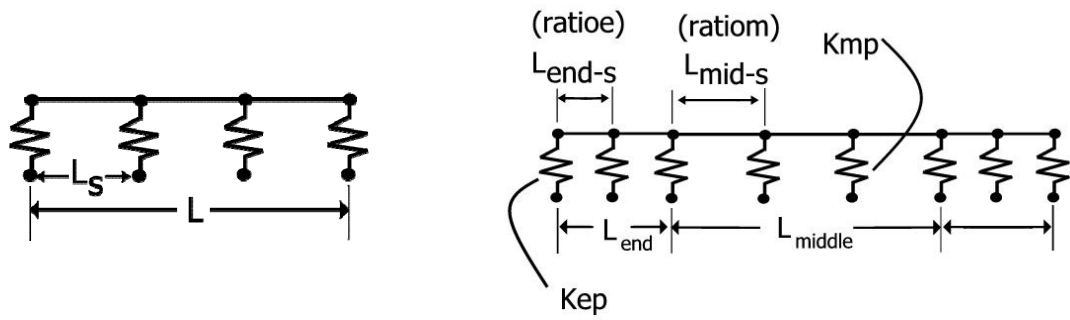


Fig. 4.10 Vertical stiffness determination from pure compression experiments, compared with elastic-halfspace stiffness solutions provided by Gazetas (1991): (a) vertical stiffness versus design FSv and (b) ratio of vertical stiffness estimates (max and min experimental) normalized by Gazetas (1991) stiffness versus design FSv



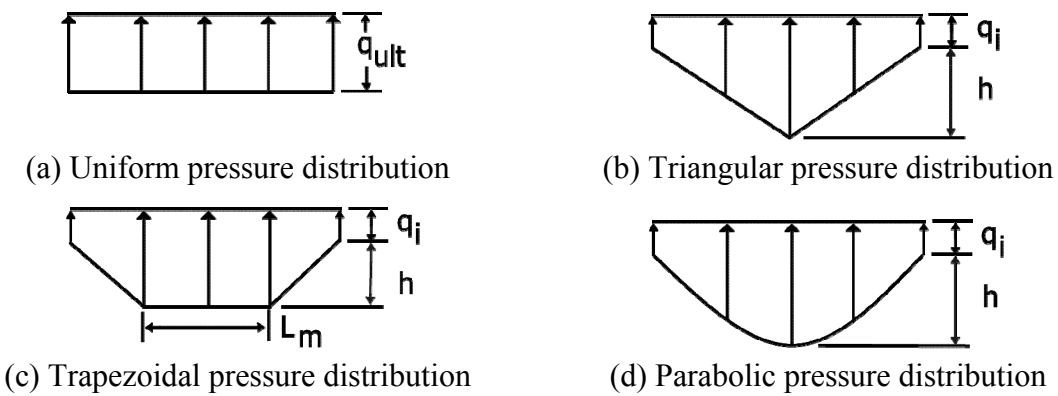
**Fig. 4.11 Compensation for highly coupled vertical and rotational system stiffness as recommended in ATC-40 (1996)**



(a) Uniform lateral spring spacing

(b) Variable lateral spring spacing

**Fig. 4.12 Lateral spring distributions in *BNWFShallow* mesh generator**



(a) Uniform pressure distribution

(b) Triangular pressure distribution

(c) Trapezoidal pressure distribution

(d) Parabolic pressure distribution

**Fig 4.13 Bearing-capacity distributions available in *BNWFShallow* mesh generator**

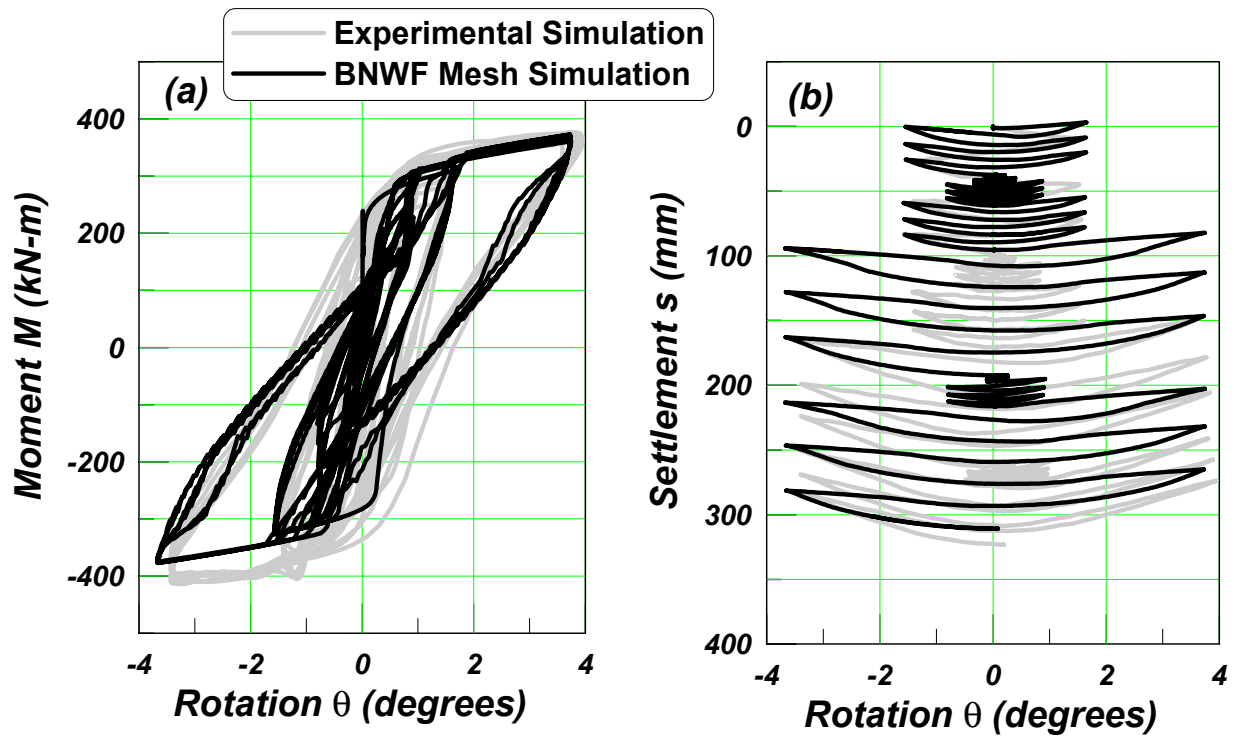


**Fig. 4.14 Comparison of experimental and numerical simulation of rocking shallow foundation: (a) moment-rotation response and (b) settlement-rotation response. Experimental dataset: KRR02-S21 (Parameters: centrifuge, sand, small footing,  $FS_v = 3.0$ ).**

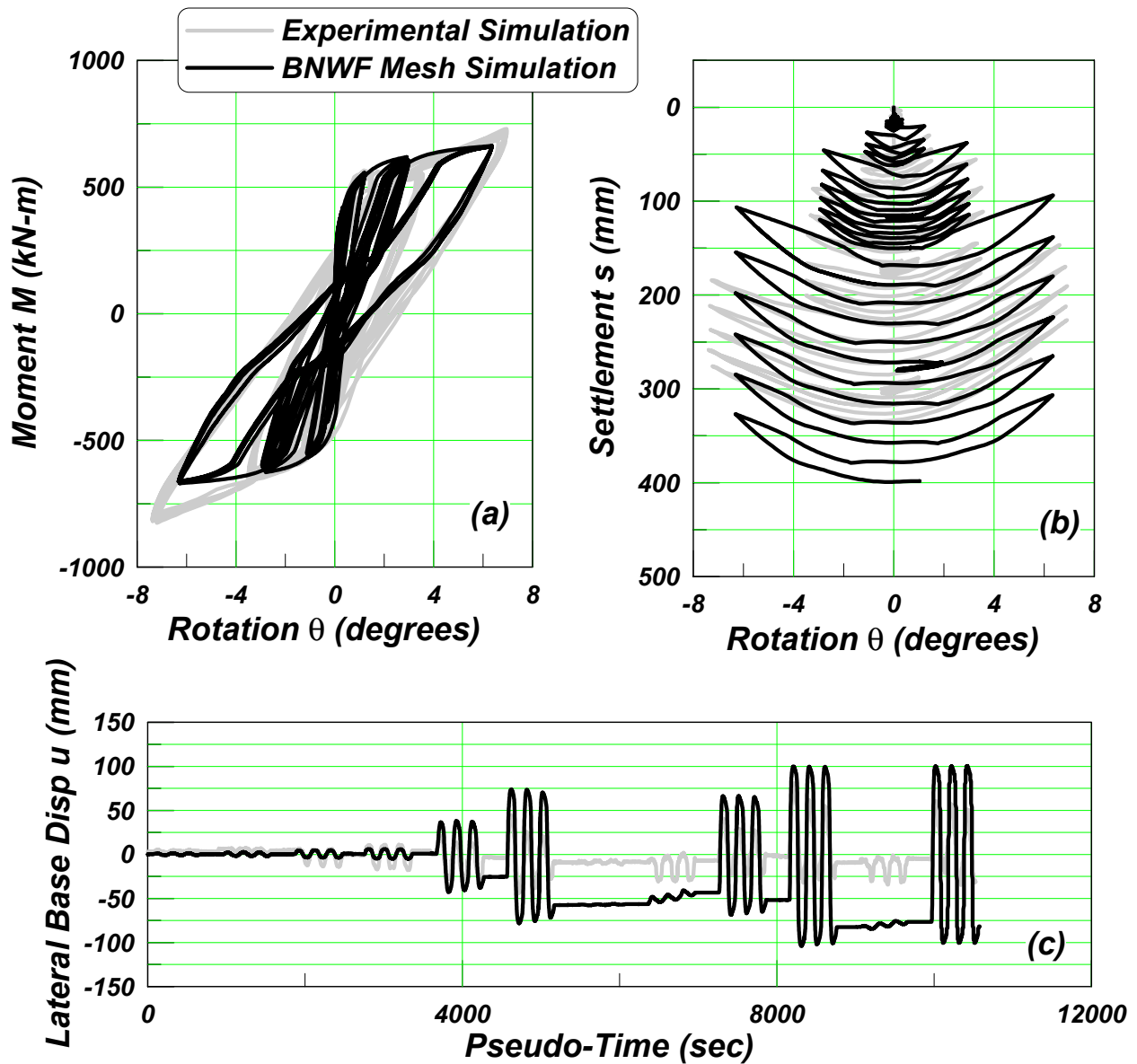


Fig. 4.15 Comparison of experimental and numerical simulation of rocking shallow foundation: (a) moment-rotation response, (b) settlement-rotation response, and (c) lateral base displacement versus pseudo-time. Experimental dataset: KRR02-S38 (Parameters: centrifuge, sand, large footing, FSv = 6.2).

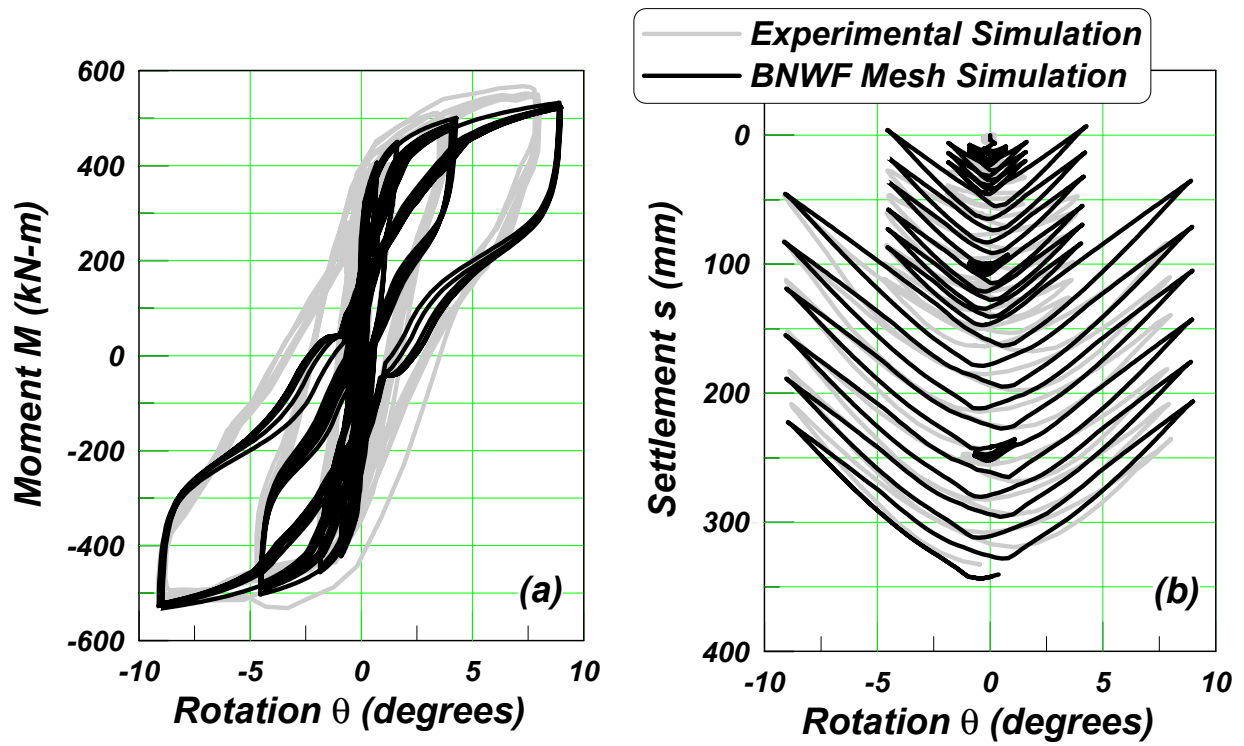


Fig. 4.16 Comparison of experimental and numerical simulation of rocking shallow foundation: (a) moment-rotation response and (b) settlement-rotation response. Experimental dataset: KRR03-S18 (Parameters: centrifuge, clay, small footing, FSv = 2.8).

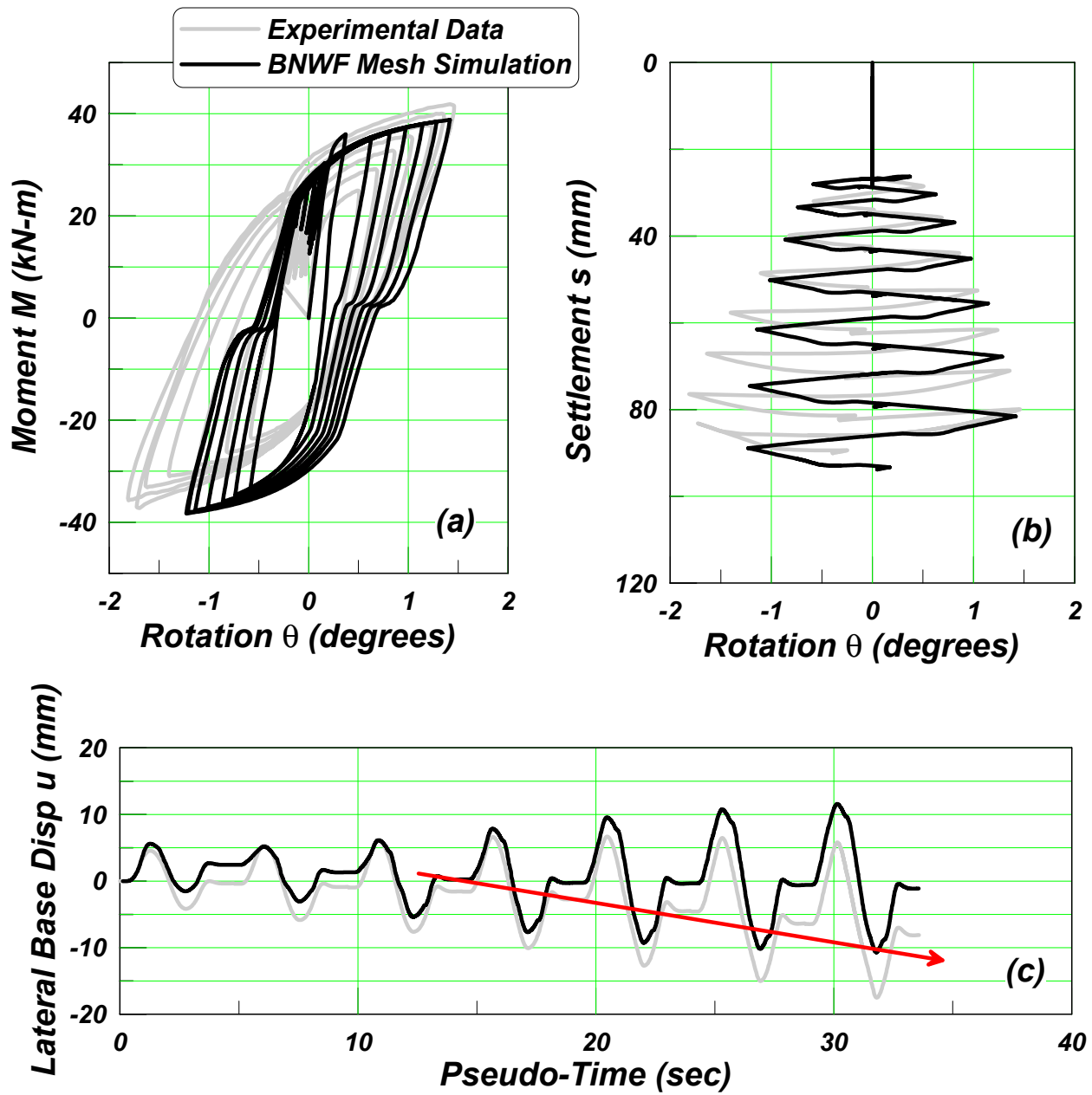
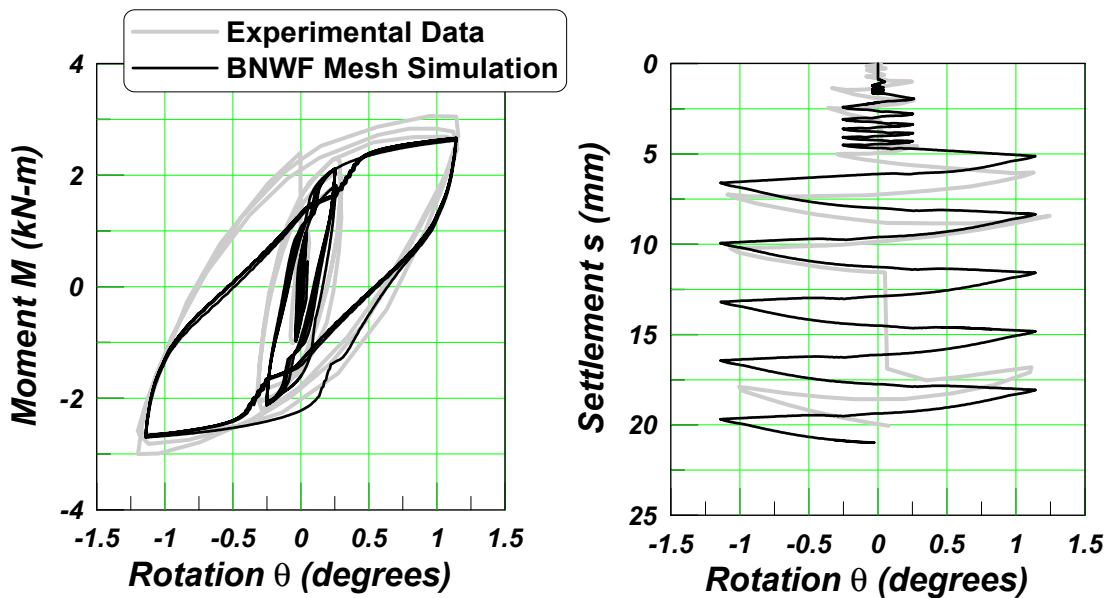
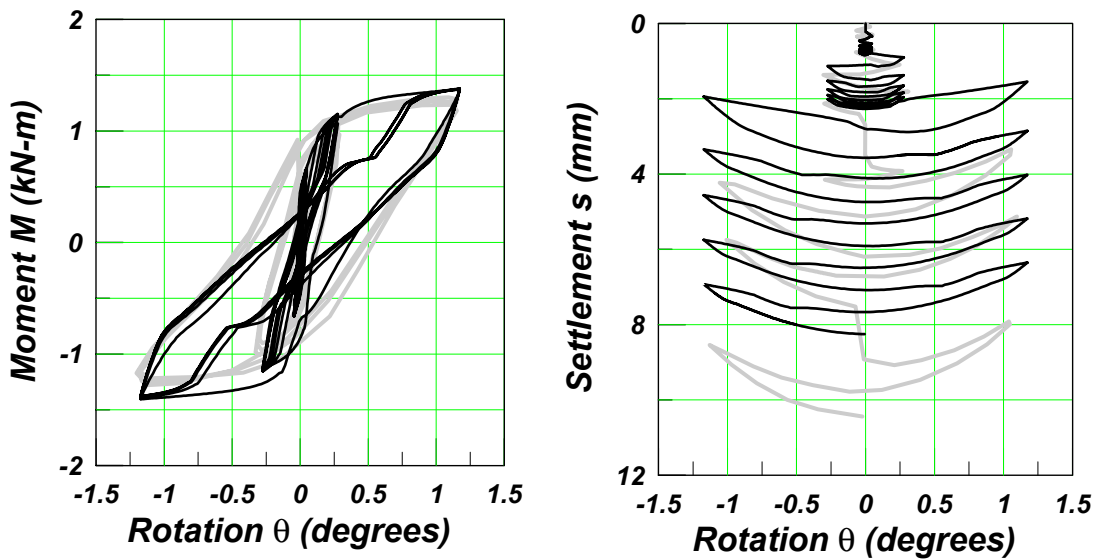


Fig. 4.17 Comparison of experimental and numerical simulation of rocking shallow foundation: (a) moment-rotation response, (b) settlement-rotation response, and (c) lateral base displacement versus pseudo-time. Experimental dataset: TRISEE83 (Parameters: 1g, (low-density) sand, square footing, FSv = 2.0).



**(a) Weissing Test Series Type A Footing (FSv = 2.0)**



**(b) Weissing Test Series Type A Footing (FSv = 5.0)**

Type A Footings: Strong Axis Rocking

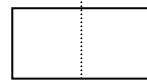
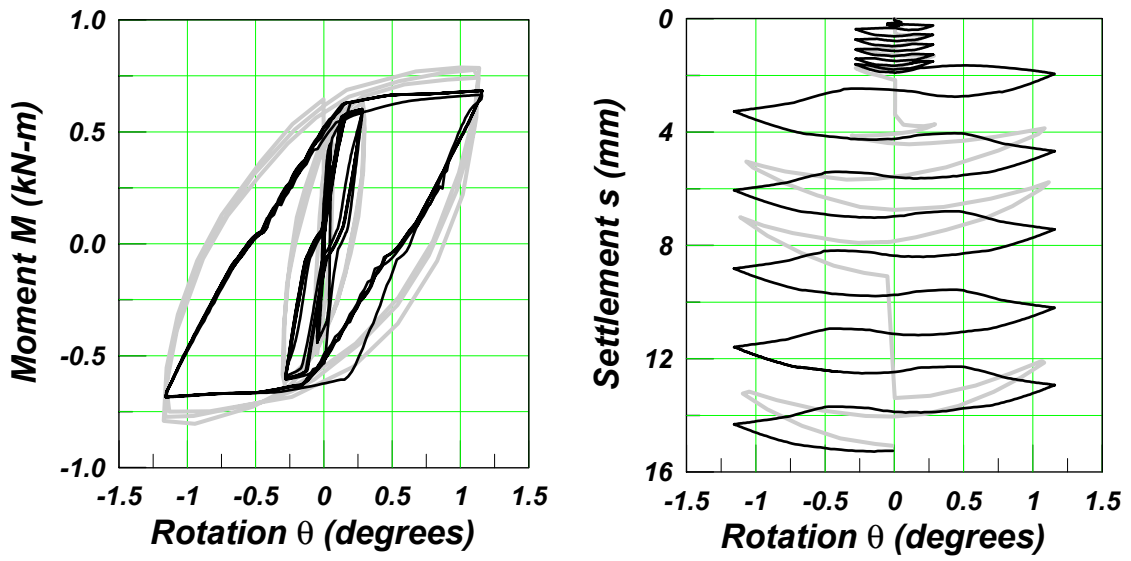
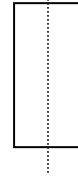


Fig. 4.18 Comparison of experimental and numerical simulation of rocking shallow foundation: moment-rotation and settlement-rotation response: (a) Type A footing (FSv = 2.0), (b) Type A footing (FSv = 5.0) and (c) Type B footing (FSv = 5.0). Experimental dataset: Weissing (1979) (Parameters: 1g, and sand).



**(c) Weissing Test Series Type B Footing ( $FS_v = 5.0$ )**

Type B Footings: Weak Axis Rocking



**Fig. 4.18—Continued**

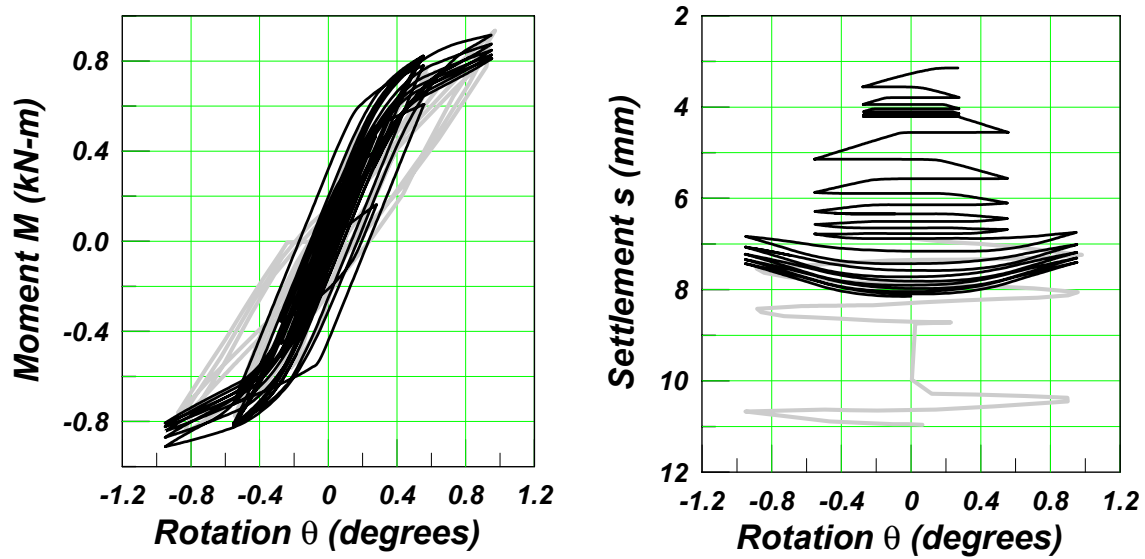


**Fig. 4.19 Comparison of experimental and numerical simulation of rocking shallow foundation: moment-rotation and settlement-rotation response:**  
**(a) Experimental response and (b) numerical response. Experimental dataset: Bartlett (1976) (Parameters: 1g, clay, Type B footing and  $FS_v = 1.5$ ).**

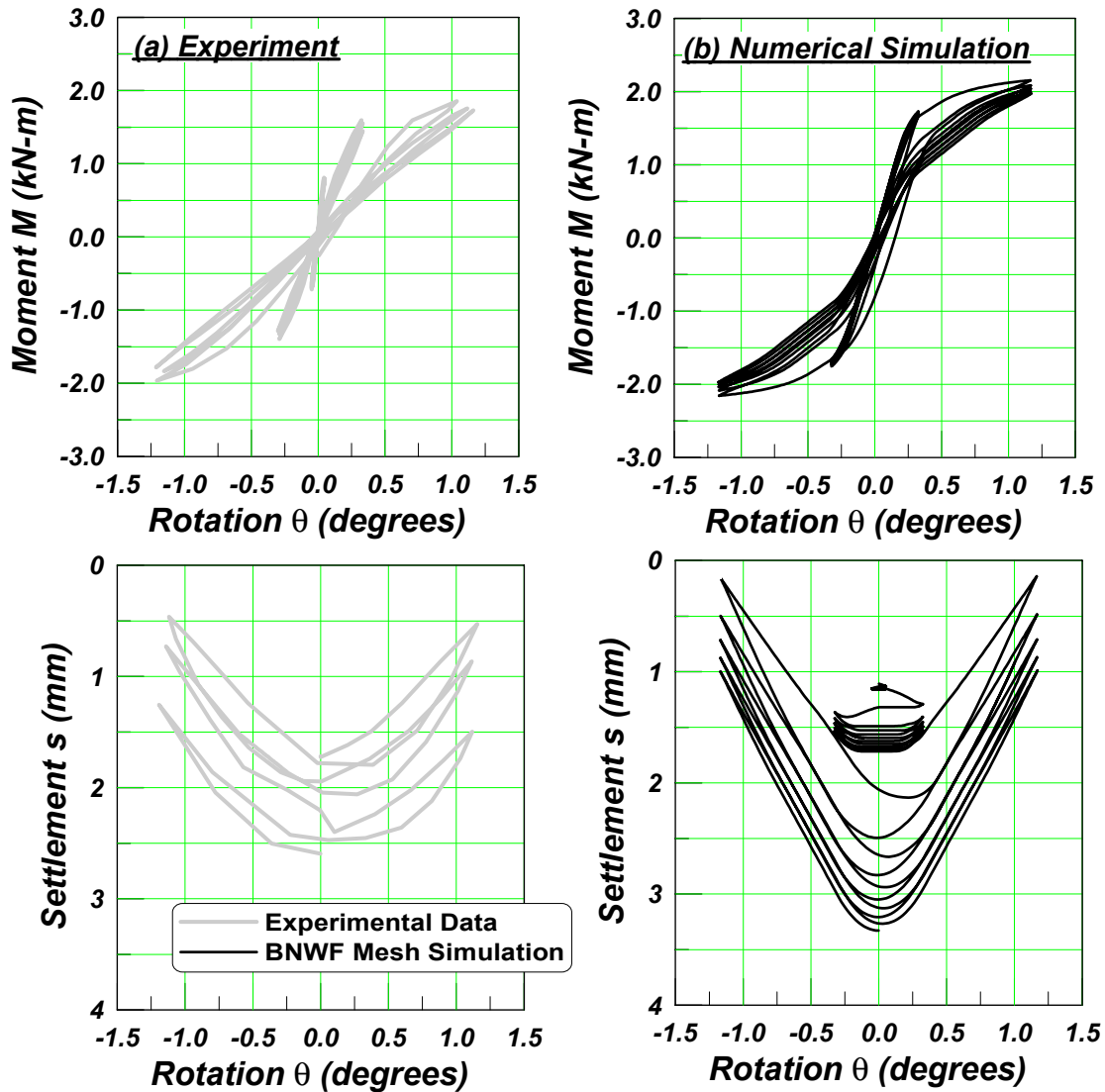


**Fig. 4.20** Comparison of experimental and numerical simulation of rocking shallow foundation: moment-rotation and settlement-rotation response: (a) Experimental response and (b) numerical response. Experimental dataset: Bartlett (1976). (Parameters: 1g, clay, Type A footing and  $FS_v = 3.0$ ).

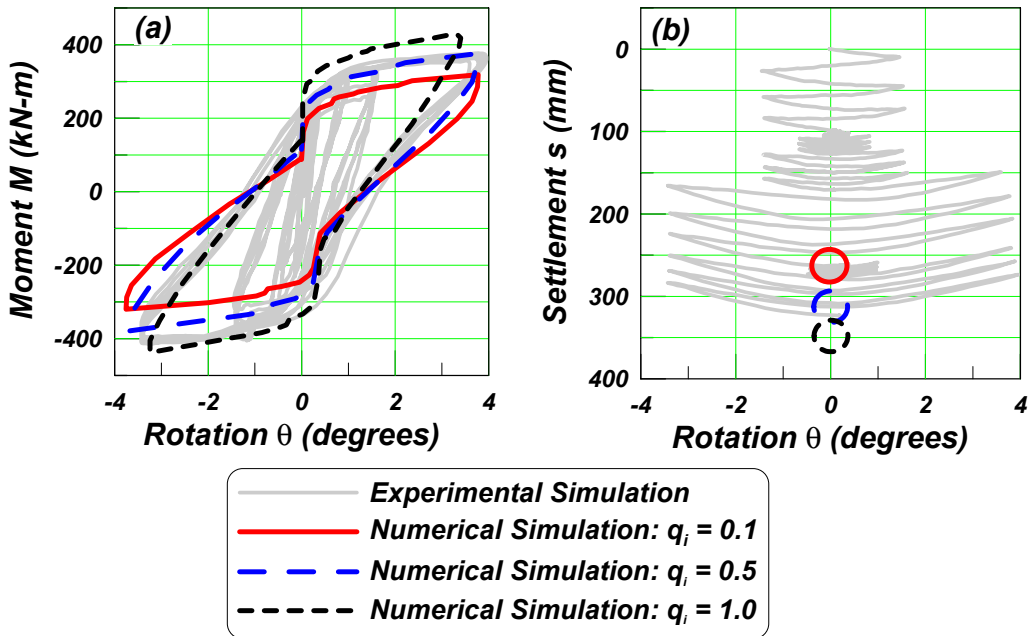


Fig. 4.21 Sensitivity of analysis results considering varying end tip resistance  $q_i$ : (a) moment-rotation behavior and (b) settlement-rotation behavior (KRR02-S21 Series data)

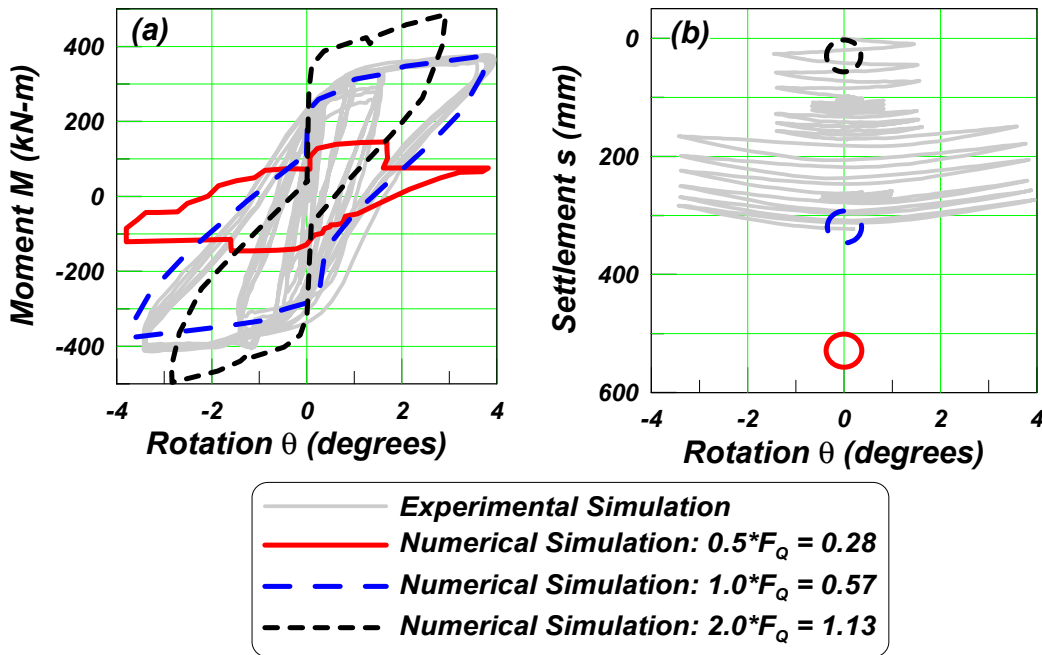


Fig. 4.22 Sensitivity of analysis results considering varying bearing-capacity factors  $F_Q$ : (a) moment-rotation behavior and (b) settlement-rotation behavior (KRR02-S21 Series data)

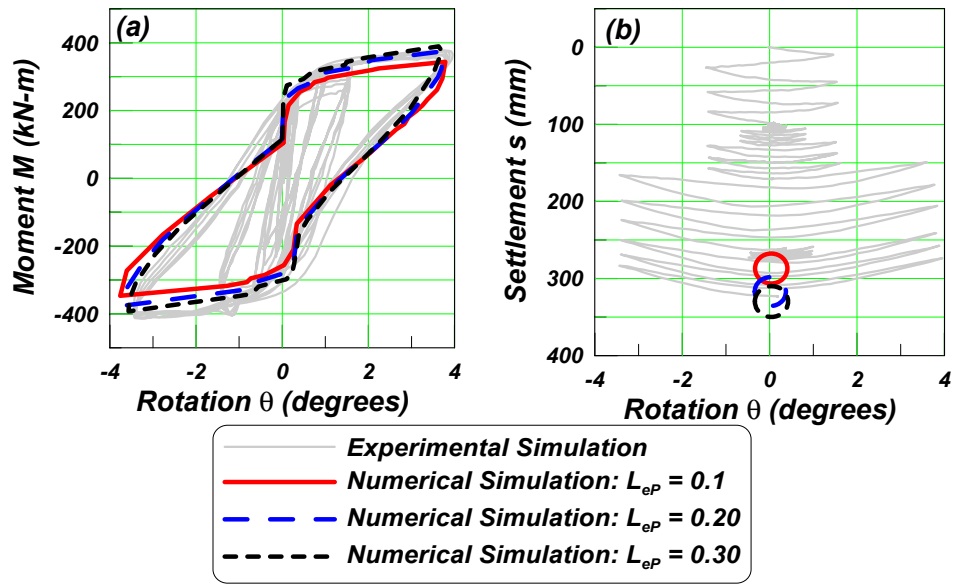


Fig. 4.23 Sensitivity of analysis results considering varying end length  $L_{ep}$ : (a) moment-rotation behavior and (b) settlement-rotation behavior (KRR02-S21 Series data)

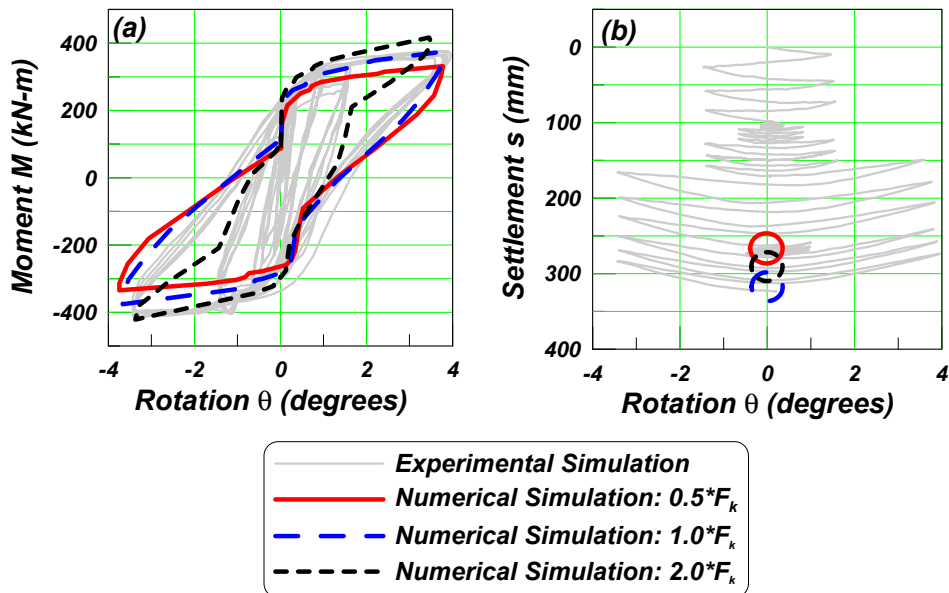


Fig. 4.24 Sensitivity of analysis results considering varying vertical spring stiffness: (a) moment-rotation behavior and (b) settlement-rotation behavior (KRR02-S21 Series data)

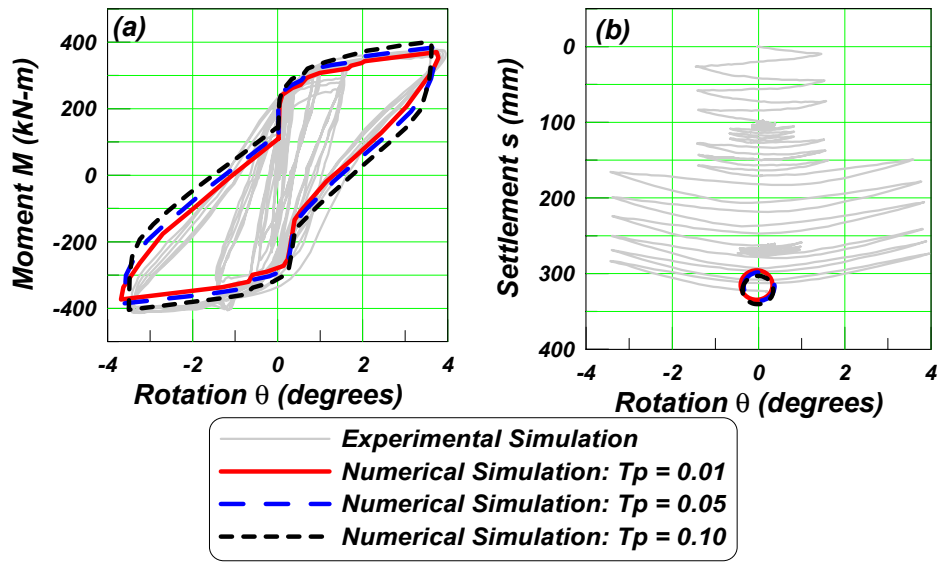


Fig. 4.25 Sensitivity of analysis results considering variations in suction (as a function of total compression capacity): (a) moment-rotation behavior and (b) settlement-rotation behavior (KRR02-S21 Series data)

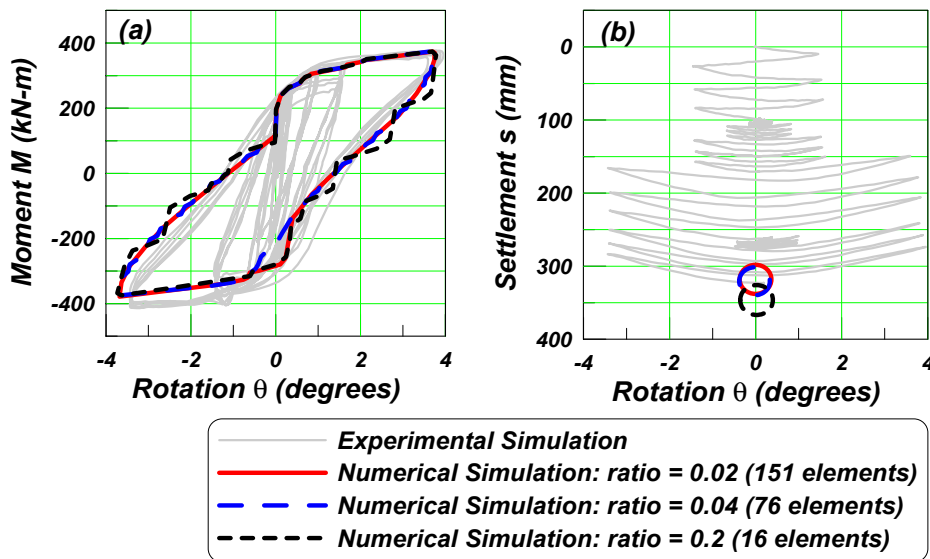


Fig. 4.26 Sensitivity of analysis results considering varying lateral spring distribution: (a) moment-rotation behavior and (b) settlement-rotation behavior (KRR02-S21 Series data)

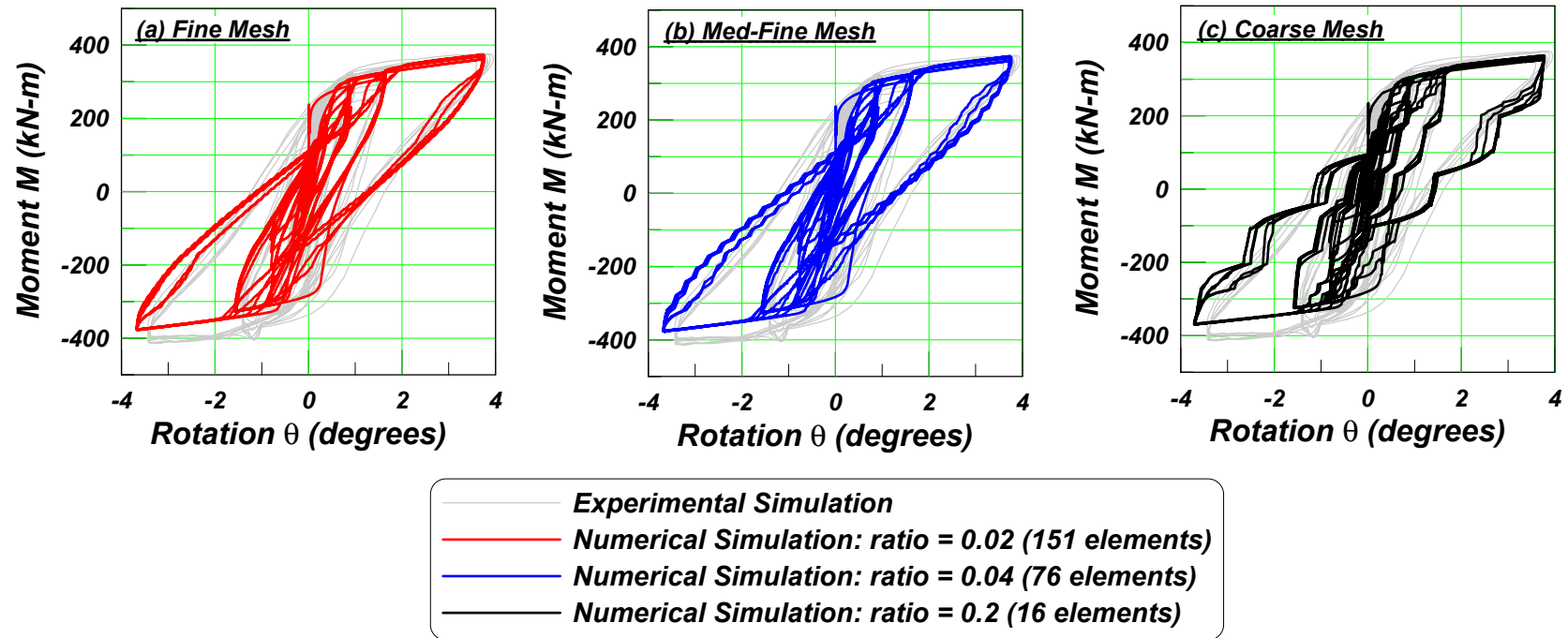
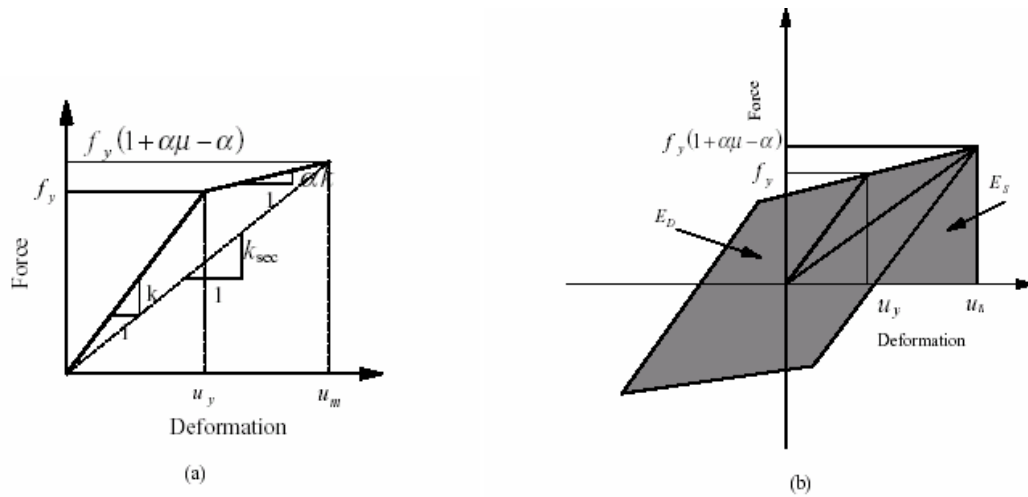
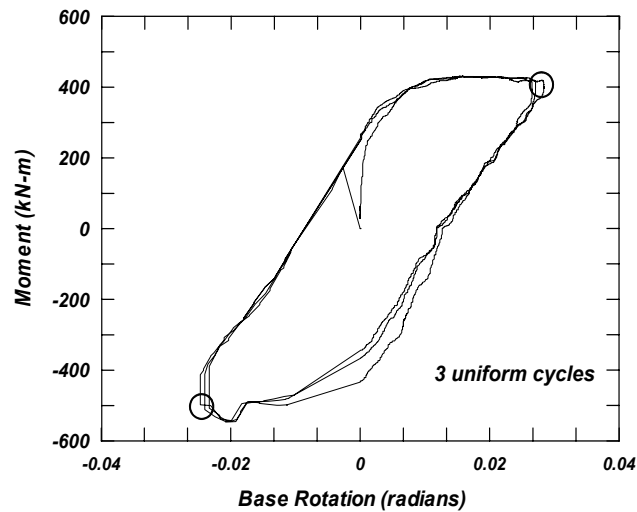


Fig. 4.27 Sensitivity of moment-rotation behavior results considering varying lateral spring distributions: (a) fine mesh, (b) medium-fine mesh, and (c) coarse mesh. (KRR02-S21 Series data)



**Fig. 4.28 Equivalent linear system approach (after Chopra and Goel 1999): (a) inelastic system bilinear response and (b) determination of equivalent viscous damping due to hysteretic energy dissipation**



**Fig. 4.29 Estimation of equivalent damping using experimental M- $\theta$  data**

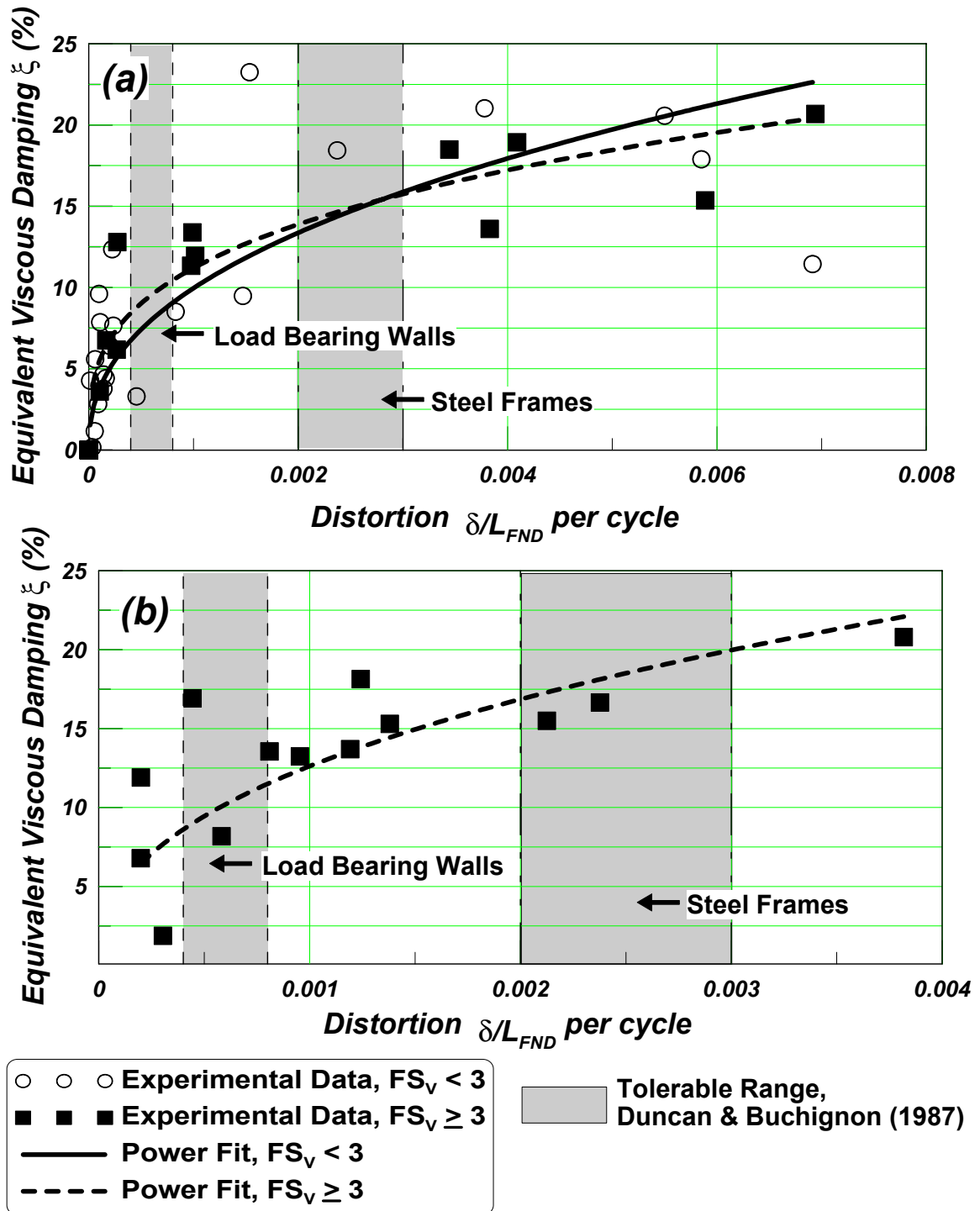


Fig. 4.30 Effective viscous damping versus maximum footing distortion (settlement normalized by footing length) per cycle: (a) sand data and (b) clay data

# 5 Macro-Element Model

## 5.1 INTRODUCTION

The concept of macro-element modeling to simulate the load-displacement behavior of shallow foundations under monotonic, slow-cyclic, and dynamic loading conditions has been proposed by many authors. The macro-element constitutive model, based on plasticity theory, considers the foundation and the soil as a macro-element for which the loading acts as generalized stress variables while the displacements of the foundations are the corresponding generalized strain variables. Nova and Montrasio (1991) developed a macro-element model that evaluates the displacements of rigid shallow foundations on sand under combined action of inclined and eccentric loading conditions. The constitutive law of the macro element is rigid-plastic strain-hardening with a nonassociative flow rule. Houlsby and Cassidy (2002) developed a macro-element model, based on work-hardening plasticity theory, to predict the behavior of rigid circular footings on sand when subjected to combined vertical, horizontal and moment loading. The models proposed by Nova and Montrasio (1991) and Houlsby and Cassidy (2002) were developed for monotonic loading conditions, and the model parameters were obtained from experiments conducted in 1-g model tests for a wide range of monotonic loading paths. Cremer et al. (2001) proposed a nonlinear soil-structure interaction cyclic macro-element model for shallow foundations on cohesive soil. The element describes the behavior of the foundation under cyclic loading, reproducing the material nonlinearities (yielding of soil under the foundation) as well as the geometrical nonlinearities (uplift at the soil-foundation interface). Model parameters were identified by using the simulations of the finite element program Dynaflo for various types of cyclic loading paths.

## 5.2 NOVA AND MONTRASIO (1991) MODEL

The sign conventions used in all the models is shown in Figure 5.1, where  $V$ ,  $H$ , and  $M$  are vertical force, horizontal force, and moment, respectively, and  $w$ ,  $u$ , and  $\theta$  are settlement, lateral sliding, and rotation, respectively. The vertical load-settlement curve, for pure vertical loading, was modeled by means of a simple analytical relationship:

$$\frac{V}{V_M} = 1 - \exp\left(-\frac{R_0 w}{V_M}\right) \quad (5.1)$$

where,  $V$  is the vertical load,  $V_M$  is the vertical failure load (for pure vertical loading),  $R_0$  is the initial slope of the load-settlement curve, and  $w$  is the settlement.  $V_M$  and  $R_0$  can be determined from experiments.

### 5.2.1 Generalized Forces and Displacements

The dimensionless generalized forces ( $F_V, F_H, F_M$ ) and displacements ( $U_V, U_H, U_M$ ) are defined in such a way that the vector product  $(F_V, F_H, F_M) \bullet (U_V, U_H, U_M)$  is a proper expression for the work density.

$$\begin{pmatrix} F_V \\ F_H \\ F_M \end{pmatrix} = \frac{1}{V_M} \begin{pmatrix} V \\ \frac{H}{\mu} \\ \frac{M}{\psi \cdot B} \end{pmatrix} \quad \text{and} \quad \begin{pmatrix} U_V \\ U_H \\ U_M \end{pmatrix} = V_M \begin{pmatrix} w \\ \mu \cdot u \\ \psi \cdot B \cdot \theta \end{pmatrix} \quad (5.2)$$

where  $V$ ,  $H$ , and  $M$  are vertical force, horizontal force and moment, respectively, and  $w$ ,  $u$ , and  $\theta$  are settlement, lateral sliding, and rotation, respectively,  $B$  is the foundation width,  $\mu$  is the initial slope of the failure envelope in the  $(F_H-F_V)$  plane (soil-foundation friction coefficient), and  $\psi$  is the initial slope of the failure envelope in the  $(F_M-F_V)$  plane. The parameters  $\mu$  and  $\psi$  can be determined from experiments.

### 5.2.2 Interaction Diagrams and Failure Envelope

Interaction diagrams in the (H-V) plane and in the (M-V) plane at failure were obtained using experimental results. Figures 5.2 and 5.3 show the interaction diagrams in the (H-V) and (M-V) planes, respectively. The analytical expressions used to describe the interaction diagrams are very similar to those obtained by Butterfield and Tico (1979).

In (H-V) plane (Fig. 5.2):

$$f(F_H, F_V) = F_H - F_V(1 - F_V)^\beta = 0 \quad (5.3)$$

In (M-V) plane (Fig. 5.3):

$$f(F_M, F_V) = F_M - F_V(1 - F_V)^\beta = 0 \quad (5.4)$$

and the final failure envelope under combined (V-H-M) loading is expressed in terms of generalized force variables.

$$f(F_H, F_M, F_V) = F_H^2 + F_M^2 - F_V^2(1 - F_V)^{2\beta} = 0 \quad (5.5)$$

where  $\beta$ , a parameter that controls the shape of the failure surface, can be found from experiments.

### 5.2.3 Yield Surface and Hardening Law

The model neglects the elastic displacements. Plastic displacements occur as the load path touches the yield surface. The equation of the yield surface is written as:

$$f = F_H^2 + F_M^2 - F_V^2 \left( 1 - \frac{F_V}{\rho_c} \right)^{2\beta} = 0 \quad (5.6)$$

where,  $\rho_c$  is a function of the history of the system (intercept of  $f$  in  $F_V$  axis, an isotropic hardening parameter). The yield surface is a closed surface in forces' space, which has the same shape of the failure envelope and coincides with it when  $\rho_c = 1$ . A convenient measure of  $\rho_c$  is a scalar function of generalized strains. It was assumed that:

$$\rho_c = 1 - \exp \left[ - \frac{R_0}{V_M^2} \left( U_V^2 + \left( \frac{\alpha |U_H|}{\mu} \right)^2 + \left( \frac{\gamma |U_M|}{\psi} \right)^2 \right)^{\frac{1}{2}} \right] \quad (5.7)$$

where,  $\alpha$  and  $\gamma$  nondimensional hardening parameters, can be determined from experiments.

#### 5.2.4 Plastic Potential and Flow Rule

It is assumed that the plastic potential is given by:

$$g = \lambda^2 F_H^2 + \chi^2 F_M^2 - F_V^2 \left( 1 - \frac{F_V}{\rho_g} \right)^{2\beta} = 0 \quad (5.8)$$

where  $\lambda = \mu / \mu_g$  and  $\chi = \psi / \psi_g$ , and  $\mu_g$  and  $\psi_g$  are constitutive parameters that can be determined experimentally. If  $\lambda = \chi = 1$ , the plastic potential and yield surface coincide and the flow rule is associated. However experimental evidence suggests that  $\mu_g$  and  $\psi_g$  are larger than  $\mu$  and  $\psi$ , respectively; hence a nonassociative flow rule is appropriate.

### 5.3 HOULSBY AND CASSIDY (2002) MODEL

The concept adopted in this model is that for any penetration of a foundation into the soil, a yield surface in (V-H-M) space will be established. Any changes of load within this surface will result only in elastic displacements. The shape of the yield surface is constant, but size may vary, with the yield surface expanding as the footing is pushed further into the soil.

### 5.3.1 Elastic Behavior

The elastic relationship is given by:

$$\begin{pmatrix} dV \\ \frac{dM}{2R} \\ dH \end{pmatrix} = 2R \cdot G \begin{pmatrix} k_v & 0 & 0 \\ 0 & k_m & k_c \\ 0 & k_c & k_h \end{pmatrix} \begin{pmatrix} dw_e \\ 2R \cdot d\theta_e \\ du_e \end{pmatrix} \quad (5.9)$$

where,  $R$  is the radius and  $G$  is the representative shear modulus, and  $k_v$ ,  $k_m$ ,  $k_h$ ,  $k_c$  are dimensionless elastic stiffness constants. The values of these elastic constants depend on the geometry of the footing and the Poisson's ratio of the sand.  $G$  depends on both the stress level and shear strain, and is given by:

$$\frac{G}{P_a} = g \sqrt{\frac{V}{A \cdot P_a}} \quad (5.10)$$

where,  $P_a$  is atmospheric pressure,  $A$  is the plan area of the footing, and  $g$  is a dimensionless constant.

### 5.3.2 Yield Surface

The yield surface is expressed in dimensionless terms using the variables  $v = V/V_0$ ,  $m = M/2RV_0$ , and  $h = H/V_0$ , where  $V_0$  is the maximum past vertical load for pure vertical loading (dimension of the yield surface in  $V$ -direction). The chosen form of the yield surface fits well with the experimental findings of Martin (1994).

$$f = \left(\frac{h}{h_0}\right)^2 + \left(\frac{m}{m_0}\right)^2 - 2a \frac{h}{h_0} \frac{m}{m_0} - \beta_{12} (v)^{2\beta_1} (1-v)^{2\beta_2} = 0 \quad (5.11)$$

where the factor  $\beta_{12} = \left(\frac{(\beta_1 + \beta_2)^{\beta_1 + \beta_2}}{(\beta_1)^{\beta_1} (\beta_2)^{\beta_2}}\right)^2$ .

This is a rugby-ball-shaped surface that is elliptical in section on planes at constant  $V$ , and parabolic on any section including the  $V$ -axis (Fig. 5.4). The size of the surface is determined by the point on the surface at maximum  $V$  value ( $V = V_0$ ). The shape of the surface is determined by the two parameters  $h_0$  and  $m_0$ , which determine the ratios of  $H/V$  and  $M/2RV$  at the widest section of the surface, which occurs at  $V = V_0/2$ , if  $\beta_1 = \beta_2$ . The factor “a” allows the ellipse to become eccentric. The purpose of factors  $\beta_1$  and  $\beta_2$  are twofold: (1) the position of the maximum size of the elliptical section can be moved ( $V = \beta_2 V_0 / (\beta_1 + \beta_2)$ ) and (2) by choosing  $\beta_1 < 1$  and  $\beta_2 < 1$  the sharp points on the surface at  $V = 0$  and  $V = V_0$  can be eliminated.

### 5.3.3 Hardening Law

The strain-hardening expression is determined from the vertical load-penetration curve for pure vertical loading. The isotropic hardening parameter  $V_0$  is a function of plastic component of the settlement ( $w_p$ ).

$$V_0 = \frac{k \cdot w_p + \left( \frac{f_p}{1 - f_p} \right) \left( \frac{w_p}{w_{pm}} \right)^2 V_{0m}}{1 + \left( \frac{k \cdot w_{pm}}{V_{0m}} - 2 \right) \left( \frac{w_p}{w_{pm}} \right) + \left( \frac{f_p}{1 - f_p} \right) \left( \frac{w_p}{w_{pm}} \right)^2} \quad (5.12)$$

where  $k$  is an initial plastic stiffness,  $V_{0m}$  is the peak value of  $V_0$ , and  $w_{pm}$  is the value of  $w_p$  at this peak. The dimensionless constant  $f_p$  describes the limiting magnitude of vertical load as a proportion of  $V_{0m}$  (i.e.,  $V_0$  approaches to  $f_p V_{0m}$  as  $w_p$  approaches to infinity).

### 5.3.4 Plastic Potential

In the  $(M/2R, H)$  plane an associated flow rule is found to work well, but this is not the case in the  $(V, M/2R)$  or  $(V, H)$  planes, for which an associated flow rule is found to predict large vertical displacements. Therefore, for nonassociative flow rule, two association factors are used to increase the values of  $h_0$  and  $m_0$ . These factors enable the shape of the potential plastic to change in the radial plane and consequently changes radial plastic displacements.

$$g = \left( \frac{h'}{\alpha_h h_0} \right)^2 + \left( \frac{m'}{\alpha_m m_0} \right)^2 - 2a \frac{h'}{\alpha_h h_0} \frac{m'}{\alpha_m m_0} - \beta_{34} (v')^{2\beta_3} (1-v')^{2\beta_4} = 0 \quad (5.13)$$

where  $\beta_{34} = \left( \frac{(\beta_3 + \beta_4)^{\beta_3 + \beta_4}}{(\beta_3)^{\beta_{31}} (\beta_4)^{\beta_4}} \right)^2$ .

The condition  $g = 0$  is used to define a dummy parameter  $V_0'$  which gives the intersection of the plastic potential with the V-axis. The primed parameters are defined by  $v' = V/V_0'$ ,  $m' = M/2RV_0'$ , and  $h' = H/V_0'$ . Factors  $\beta_3$  and  $\beta_4$  can be chosen independently from  $\beta_1$  and  $\beta_2$ . The values of the association factors were obtained from the best fit of experimental data of Gottardi and Houlsby (1995).

$$\alpha_h = \frac{k' + \alpha_{h\infty} \left( \frac{u_p}{w_p} \right)}{k' + \left( \frac{u_p}{w_p} \right)} \quad \text{and} \quad \alpha_m = \frac{k' + \alpha_{m\infty} \left( \frac{2R\theta_p}{w_p} \right)}{k' + \left( \frac{2R\theta_p}{w_p} \right)} \quad (5.14)$$

The values of rate of change of the association factor ( $k'$ ),  $\alpha_{h\infty}$ , and  $\alpha_{m\infty}$  can be determined from experiments.

**Note:** There is a striking analogy between the structure of the above model and that of constitutive models based on critical state concepts. In the analogy the vertical load plays the same role as the mean normal stress,  $p'$ , the horizontal load or the moment are equivalent to deviator stress,  $q$ , and the vertical penetration plays the same role (with a change of sign) as the void ratio or specific volume (Houlsby and Cassidy 2002).

#### 5.4 CREMER ET AL. (2001) MODEL

The model was chosen to build around two different models, one in plasticity and one in uplift, separated but coupled. The coupling between both submodels accounts for the influence of plastic yielding on uplift and vice versa. The displacements calculated for given forces are

obtained by summing the different components; i.e., the elastic and plastic displacements issued from the plasticity model, and the uplift displacement issued from the uplift model.

## 5.4.1 Plasticity Model

### 5.4.1.1 Elastic Behavior

The elastic stiffness matrix is given by:

$$\mathbf{K} = \begin{pmatrix} K'_{zz} & 0 & 0 \\ 0 & K'_{xx} & 0 \\ 0 & 0 & K'_{\theta\theta} \end{pmatrix} \quad \text{with} \quad (5.15)$$

$$K'_{zz} = \frac{K_{zz}}{q_{\max}}, \quad K'_{xx} = \frac{K_{xx}}{q_{\max}}, \quad K'_{\theta\theta} = \frac{K_{\theta\theta}}{B^2 \cdot q_{\max}}$$

The diagonal terms are functions of the geometrical properties of the foundation (width) and of the elastic properties of the soil (shear modulus and Poisson's ratio). The off-diagonal terms were neglected because they are very low when compared to the diagonal terms and do not significantly influence the foundation response.

### 5.4.1.2 Failure Envelope

The global variables (forces and displacements) were made dimensionless to work with a system independent of the foundation width  $B$  and the plastic properties of the soil (cohesion):

$$\mathbf{F} = \begin{pmatrix} F_V \\ F_H \\ F_M \end{pmatrix} = \frac{1}{V_{\max}} \begin{pmatrix} V \\ H \\ \frac{M}{B} \end{pmatrix} \quad \mathbf{U} = \begin{pmatrix} U_V \\ U_H \\ U_M \end{pmatrix} = \frac{1}{B} \begin{pmatrix} w \\ u \\ B \cdot \theta \end{pmatrix} \quad (5.16)$$

where  $V_{\max} = q_{\max} \cdot B$ , with  $q_{\max}$  being the foundation ultimate pressure under vertical centered load.

Bearing-capacity solutions, under any loading combination (in V-H-M space), for a strip foundation lying on a homogeneous cohesive halfspace, were proposed by Pecker (1997) for a

soil obeying the Tresca criterion with and without tensile strength. For a homogeneous cohesive soil without tensile strength, the equation of the failure envelope is (Fig. 5.5):

$$\left( \frac{F_H}{aF_V^c(1-F_V)^d} \right)^2 + \left( \frac{F_M}{bF_V^e(1-F_V)^f} \right)^2 - 1 = 0 \quad (5.17)$$

with the coefficients a and b that define the size of the bounding surface of elliptic shape in the  $(F_H, F_M)$  plane, and c, d and e, f that define the parabolic shape of the bounding surface in the  $(F_V, F_H)$  and  $(F_V, F_M)$  planes, respectively.

These coefficients were determined from the curves proposed by Ukritchon et al. (1998), who derived solutions for a heterogeneous cohesive soil profile exhibiting a constant gradient of cohesion with depth.

#### **5.4.1.3 Yield Surface**

The evolution of yield surface, dragged by the forces point, moves toward the failure surface when the forces increase. The choice was guided by the need for reproducing the behavior of the soil and foundation, initially submitted to the weight of the structure, and then solicited along any loading path. The paths are mainly radial in the  $(H, M)$  plane with vertical force  $(V)$  being almost constant (Fig. 5.6). The model is particularly well adapted for these paths.

During the initialization phase of the gravity loads, the loading surface is reduced to a straight-line segment along the  $F_V$ -axis ( $F_M = F_H = 0$ ):

$$f = F_V \text{ with } F_V \in [0, \chi] \text{ and } \chi \in [0, 1]$$

At the end of initialization,

$$F_V = \chi = \frac{N}{V_{\max}} \quad (5.18)$$

where N is the weight of the structure.

As shown in Figure 5.7, for any loading, the surface dragged along by the forces point F. It simultaneously undergoes an isotropic growth and a kinematic translation of the ellipse centers

in the  $(F_H, F_M)$  plane, with a movement of the extreme point P along the  $F_V$ -axis. This point moves in such a way that when point F reaches the failure surface, point P simultaneously reaches the extreme failure point  $F_V = 1$ .

According to the above evolution, the loading surfaces are written as:

$$f = \left( \frac{F_H - \alpha \Gamma_H^\gamma}{\rho \Gamma_H^\gamma} \right)^2 + \left( \frac{F_M - \beta \Gamma_M^\gamma}{\rho \Gamma_M^\gamma} \right)^2 - 1 = 0 \quad \text{with}$$

$$\Gamma_H^\gamma = a.F_V^c (\gamma - F_V)^d \quad \text{and} \quad \Gamma_M^\gamma = b.F_V^e (\gamma - F_V)^f \quad (5.19)$$

The parameter  $\gamma$  is given by,  $\gamma = \chi + (1 - \chi) (\rho + \tau)$ .

where  $\boldsymbol{\tau} = \begin{pmatrix} 0 \\ \alpha \\ \beta \end{pmatrix}$  is the kinematic hardening vector, with  $\tau^2 = (\boldsymbol{\tau} : \boldsymbol{\tau}) = \alpha^2 + \beta^2$ , and  $\rho$  is the isotropic hardening parameter.

#### 5.4.1.4 Hardening Laws

The hardening laws describe the evolution of  $\rho$  and  $\boldsymbol{\tau}$  parameters. Cremer et al. (2001) proposed that:

$$\dot{\boldsymbol{\tau}} = \dot{\tau} \frac{\boldsymbol{\mu}}{|\boldsymbol{\mu}|} \quad (5.20)$$

where  $\dot{\tau}$  that defines the amplitude of the kinematic increment and  $\boldsymbol{\mu} / |\boldsymbol{\mu}|$  its direction.

Hardening laws are deduced from three relationships:

1. The relationship between  $\dot{\rho}$  and  $\dot{\tau}$  (Fig. 5.8). It is observed for the  $M' - \theta'$  relationship that loading of the foundation on one side almost does not influence its behavior on the other side. This condition is written as (for a radial path):

$$\dot{\rho} = \dot{\tau} \quad (5.21)$$

2. The criterion of noninterpenetration of the failure surface by the loading surface (Fig. 5.9). This criterion ensures an evolution of the loading surface such that at failure, the representative point of the forces state coincides with the meeting point of the loading surface with the failure surface. The following equations are obtained based on the above condition:

$$\boldsymbol{\mu} = \begin{bmatrix} 0 \\ \frac{(\Gamma_H)^1 \cdot \cos(\psi) - F_H}{(\Gamma_H)^\gamma} \\ \frac{(\Gamma_M)^1 \cdot \sin(\psi) - F_M}{(\Gamma_M)^\gamma} \end{bmatrix} \quad \text{where} \quad \psi = \text{atan} \left[ \frac{(\Gamma_H)^1 \cdot F_M - \beta \cdot (\Gamma_M)^1}{(\Gamma_M)^1 \cdot F_H - \alpha \cdot (\Gamma_H)^1} \right] \quad (5.22)$$

where  $(\Gamma_H)^1$  and  $(\Gamma_M)^1$  are equivalent to  $(\Gamma_H)^\gamma$  and  $(\Gamma_M)^\gamma$  but defined for the failure surface, i.e., for  $\gamma = 1$ .

3. The consistency rule:

$$\dot{f} = 0 \quad (5.23)$$

determines the amplitude  $\tau$  of the kinematic hardening incremental vector.

#### **5.4.1.5 Plastic Potential and Flow Rule**

Nonassociative flow rule is, in this particular case, required to correctly model the evolution of the plastic displacements. The choice of a nonassociative flow rule is justified because the outer normal to the yield surface is not convenient for defining the direction of the plastic displacements. This is particularly obvious for loading with small  $F_V$  (Fig. 5.10). The plastic potential is chosen as:

$$g = \left( \frac{F_H}{\kappa} \right)^2 + \left( \frac{F_M}{\xi} \right)^2 + F_V^2 - 1 = 0 \quad (5.24)$$

where the parameters  $\kappa$  and  $\xi$  determine the shape of the plastic potential.

**Note:** For the calculation of foundation settlement under a vertical centered load, the relationship proposed by Nova and Montrasio (1991) is chosen:

$$F_v = 1 - \exp(-K'_{zz} U_v) \quad (5.25)$$

## 5.4.2 Uplift Model

The separation ratio of the foundation of width  $B$  is noted as  $\delta$  (percentage of uplift); it is defined as the ratio of the length of the foundation not in contact with the soil divided by the foundation width. The displacements due to uplift of a foundation lying on an elastic soil is first determined. A cyclic model, coupled to the plasticity model, is then proposed which takes into account the irreversibility of the uplift behavior due to plasticity.

### 5.4.2.1 Uplift Model for Elastic Soil

For a foundation lying on an elastic soil layer, the following relationships are proposed for monotonic loading:

1. Before uplift:  $|M| \leq |M_0|$

$$\delta = 0; \quad \theta^{up} = 0; \quad w^{up} = 0$$

2. During uplift:  $|M| > |M_0|$

$$\delta = \frac{M}{M_0} - 1; \quad \theta^{up} = \theta_0 \frac{\delta^2}{1 - \delta}; \quad w^{up} = \frac{B\theta_0}{2} \left( \frac{\delta}{1 - \delta} + \ln(1 - \delta) \right) \quad \text{with } \delta > 0 \quad (5.26)$$

where,  $M_0 = \pm \frac{VB}{4}$ , is the moment for which uplift is initiated for a perfectly rigid shallow foundation lying on an elastic homogeneous soil medium, under the assumption of an actual vertical stress distribution under the foundation, i.e., vertical stresses tending toward infinity at the edges of the foundation (Cremer et al., 2001), and  $\theta_0$  is the rotation corresponding to  $M_0$ .

### 5.4.2.2 Uplift Model for Elasto-Plastic Soil

Uplift behavior on plastic soil is strongly coupled to and influenced by yielding of soil (during cyclic loading). Similar to what is done in the plasticity model, i.e., a yield surface growing inside the failure envelope for a particular yield level, in the uplift model, an uplift surface moving inside an uplift domain defining the percentage of uplift. The iso-uplift surfaces are shown in Figure 5.11 (their shapes are deduced from Dynaflow numerical simulation). They are superimposed on the failure criterion of the plasticity model. The only values of uplift, which may be reached during loading, are defined by the part of the uplift domain located inside the failure criterion. The evolution of  $\delta$  is a linear function of  $(M/V)$  or  $(F_M / F_V)$ . The initial slope is dependent on the current plastic or elastic state defined by the plasticity model. Figure 5.12 shows the coupling between plasticity and uplift.

As shown in Figure 5.12, for a given  $F_H$  and  $F_V$ , uplift occurs if  $|F_M| > |F_{M0}^{(i)}|$  and is equal to:

1. If  $|F_M| > |F_{Mp}^{(i)}|$ :

$$\delta = \frac{4}{F_V} |F_M - F_{M0}^{(0)}| \quad (5.27)$$

where  $F_{M0}^{(0)} = \pm \frac{F_V}{4} \cdot \exp(-AF_V)$ , the moment at the uplift onset during virgin loading, and  $A$  is a constant.

2. If  $|F_M| \leq |F_{Mp}^{(i)}|$ :

$$\delta = \frac{4}{\eta F_V} |F_M - F_{M0}^{(i)}| \quad (5.28)$$

where  $F_{M0}^{(i)} = F_{Mp}^{(i)} - \frac{\eta F_V}{4} \delta_p^{(i)}$ , the moment at the uplift onset during unloading-reloading. It depends on the maximum moment reached during the previous loadings. The  $(i)$  index refers to this greatest loading state. The factor  $\eta$  defines the slope increase during unloading-reloading where  $F_{Mp}^{(i)}$  is the moment belonging to the loading surface. It corresponds to the greatest loading state previously reached;  $\delta_p^{(i)}$  is the uplift corresponding to  $F_{Mp}^{(i)}$ .

In order to ensure that  $U_M^{up}$  tends toward infinity when the soil fails under a purely overturning mechanism (i.e., for  $F_H$  tends to zero),  $\delta$  is replaced by the ratio of  $\delta/\delta_{max}$ .  $\delta_{max}$  is the maximum percentage of separation width reached at failure for a given  $F_V$  and for  $F_H = 0$ .

$$\delta_{max} = \frac{4}{F_V} (F_{M_{max}} - F_{M0}) \quad (5.29)$$

where  $F_{M_{max}} = bF_V^e(1 - F_V)^f$ , is the maximum moment reached at failure for a given  $F_V$  and  $F_H=0$ .

The displacement components due to uplift are expressed as:

$$U_M^{up} = (1 - F_V)\theta_0 \frac{(\delta/\delta_{max})^2}{(1 - \delta/\delta_{max})} \quad (5.30)$$

$$U_V^{up} = (1 - F_V) \frac{\theta_0}{2} \left( \frac{\delta/\delta_{max}}{1 - \delta/\delta_{max}} + \ln(1 - \delta/\delta_{max}) \right) \quad (5.31)$$

The coupling between yielding and uplift is included by the term  $(1-F_V)$ . When  $F_V$  tends to 0, the coefficient is equal to 1 (no yielding), and when  $F_V$  tends to 1, the coefficient is equal to 0 (no uplift).

## 5.5 IMPLEMENTATION OF CREMER ET AL. (2001) MODEL

The model is implemented in C++. First, the model behavior is explored during monotonic loading and slow cyclic loading conditions. Initialization is done by applying the self weight, and then the structure is subjected to a monotonic and slow cyclic lateral push at a constant height ( $M/H = \text{constant}$ ). It should be noted that the model is particularly well suited for these kinds of loading conditions. Implementation is carried out in both the load control and displacement control methods. Implementation of the load control method is simple compared to the displacement control method; however the load control method cannot predict the softening behavior. The displacement control method is complicated, particularly in this case, because the total displacements consist of elastic, plastic, and uplift components that are calculated from two

different, but coupled models (plasticity model and uplift model). The calculations are done using the methods used in standard finite element procedures: explicit method and implicit method. The explicit method is faster than the implicit method, but less accurate. Although the implicit method is more accurate, the calculations are time consuming.

### 5.5.1 Explicit Method

The global model can be written as:

$$\underline{\dot{F}} = \left[ \underline{\underline{K}}^{\text{elpl}} \right]^{-1} + \left[ \underline{\underline{K}}^{\text{up}} \right]^{-1} : \underline{\dot{u}} \quad \text{where} \quad \underline{\dot{u}} = \underline{\dot{u}}^{\text{el}} + \underline{\dot{u}}^{\text{pl}} + \underline{\dot{u}}^{\text{up}} \quad (5.32)$$

The expression for the elasto-plastic tangent stiffness matrix can be derived as:

$$\underline{\dot{F}} = \left[ \underline{\underline{K}}^{\text{el}} - \frac{1}{h' + h_0} (\underline{\underline{K}}^{\text{el}} : \underline{\mathbf{P}}) \otimes (\underline{\mathbf{Q}} : \underline{\underline{K}}^{\text{el}}) \right] : \underline{\dot{u}}^{\text{elpl}} \quad \text{with} \quad h_0 = \underline{\mathbf{Q}} : \underline{\underline{K}}^{\text{el}} : \underline{\mathbf{P}} \quad (5.33)$$

where,  $\mathbf{K}^{\text{el}}$  is the elastic stiffness matrix,  $h'$  is the plastic modulus,  $\mathbf{P}$  contains the derivatives of plastic potential with respect to forces, and  $\mathbf{Q}$  contains the derivatives of the yield surface with respect to forces.

The displacements due to uplift can be obtained from the uplift model:

$$\underline{\dot{F}} = \underline{\underline{K}}^{\text{up}} : \underline{\dot{u}}^{\text{up}} \quad (5.34)$$

### 5.5.2 Implicit Method

Implicit calculations are done using the backward Euler method and modified Newton-Raphson iteration procedures. The backward Euler algorithm uses the “predictor-corrector” method to get the load and displacement components more accurate.

$$\underline{\mathbf{F}}^i = \underline{\mathbf{F}}^{\text{pred}} - \dot{\lambda}^i (\underline{\mathbf{K}}^{\text{el}} : \underline{\mathbf{P}}^i) \quad \text{with} \quad \dot{\lambda}^i = \frac{f^i}{h^{\prime i} + \underline{\mathbf{Q}}^i : \underline{\mathbf{K}}^{\text{el}} : \underline{\mathbf{P}}^i} \quad (5.35)$$

where,  $f$  is the yield function,  $\lambda$  is the plastic multiplier or loading index, and “ $i$ ” refers to the current iteration step.

## 5.6 SUMMARY

A review of macro-element modeling in the literature is fairly complete, and we have attempted to implement Cremer's model into computer code. The model assumes that there are displacements due to elasticity, plasticity, and uplift. The model is quite complex and we have not yet succeeded in implementation. Based upon experience to date we have the following preliminary conclusions:

Cremer's model was developed for clay, and we have not been able to confirm that the predictions would be reasonable for sand. If not, we will need to modify the model. The model assumes for cyclic loading elastic behavior that does not exceed the maximum past stress, while the experimental data indicate that there is substantial energy dissipation even for smaller loading cycles.

The macro-element models developed by Hously and Cassidy are applicable to sand, but their models published to date are largely limited to monotonic loading. One different feature of the Hously and Cassidy model is that loads are normalized by the maximum past vertical load; they do not normalize by the vertical bearing capacity.

An improved macro-element model may be derived by combining the features of Cremer's model and the Hously and Cassidy model.

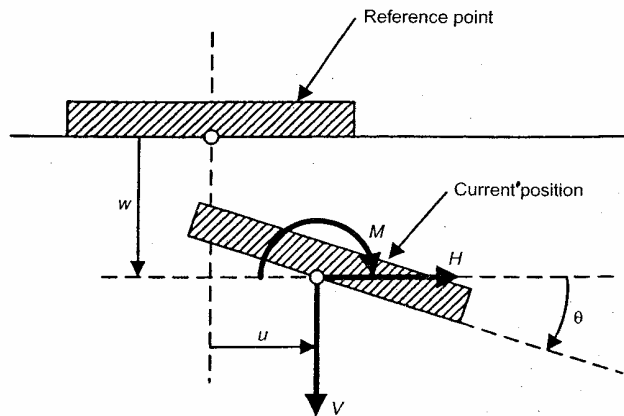


Fig. 5.1 Sign conventions for load and displacements (after Hously and Cassidy, 2002)

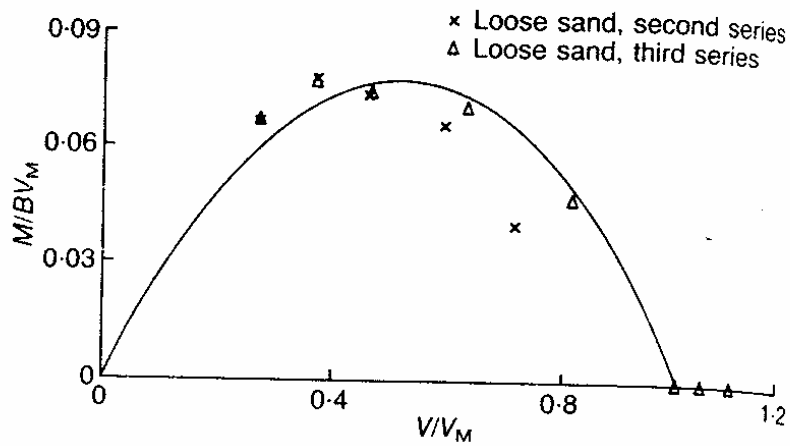


Fig. 5.2 Failure envelope in  $(F_H-F_V)$  plane (after Nova and Montrasio, 1991)

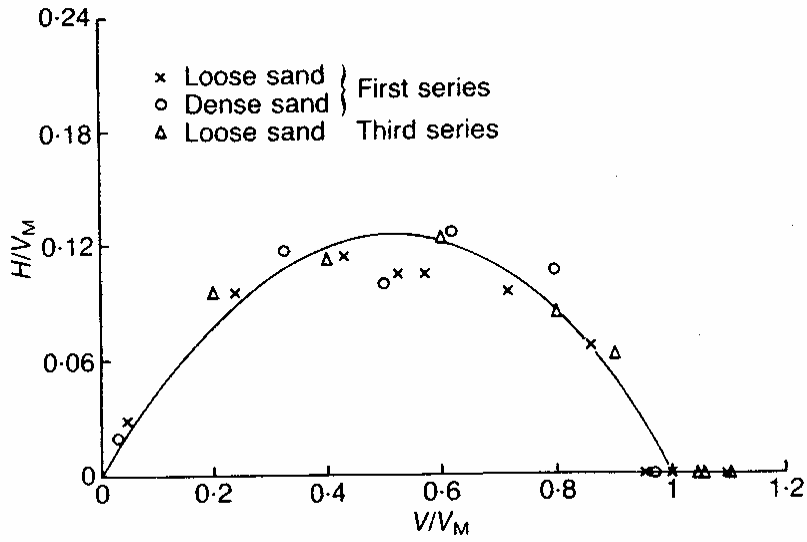


Fig. 5.3 Failure envelope in  $(F_H - F_V)$  plane (after Nova and Montrasio, 1991)

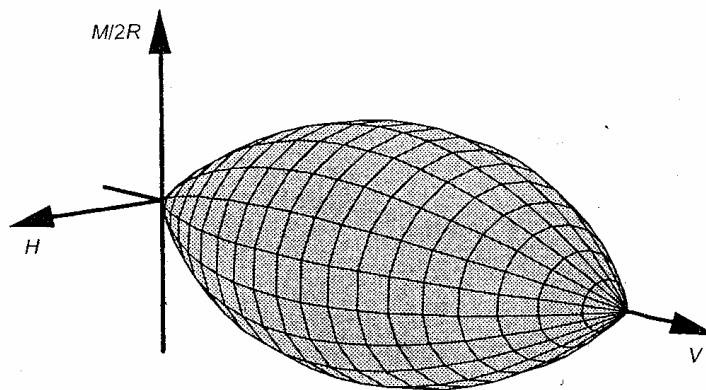


Fig. 5.4 Shape of the yield surface in  $(V, H, M/2R)$  space (after Houlsby and Cassidy, 2002)

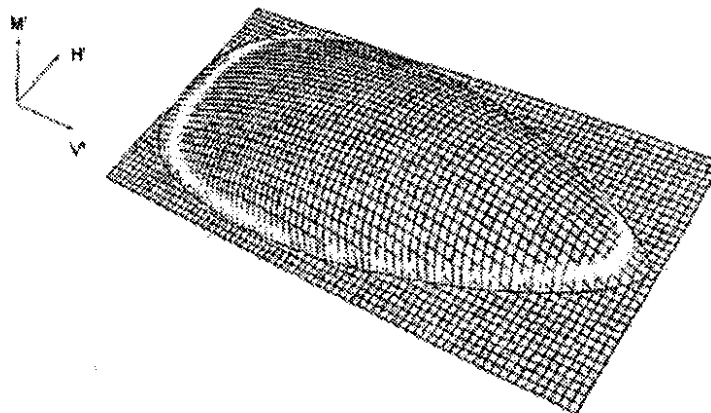
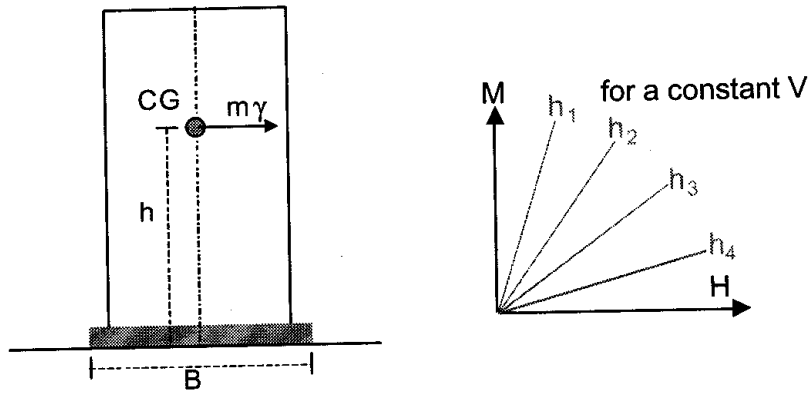
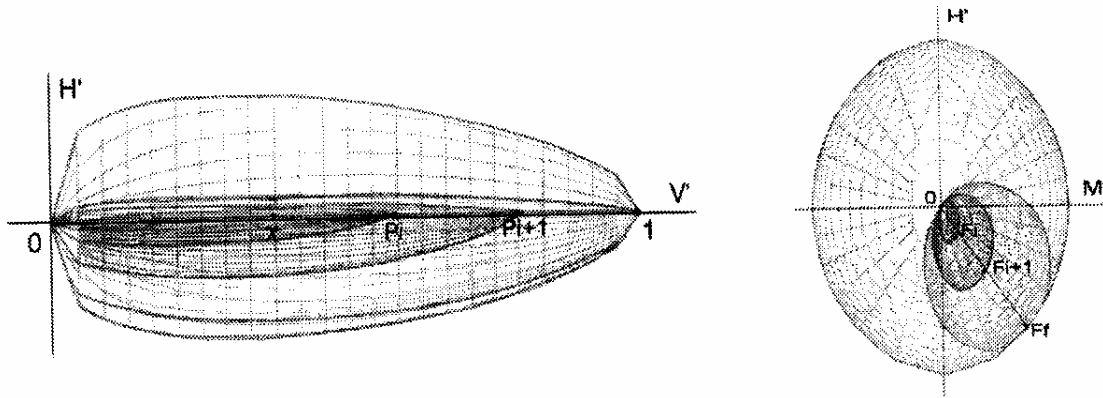


Fig. 5.5 Failure envelope in  $(F_V - F_H - F_M)$  space (after Cremer et al., 2001)



**Fig. 5.6** Types of loading path preferentially developed during seismic action for a structure with one predominant mode (after Cremer et al., 2001)



**Fig. 5.7** Evolution of the loading surface (after Cremer et al., 2001)

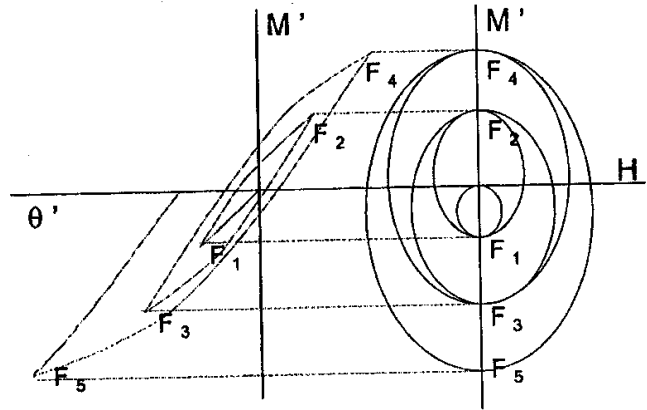


**Fig. 5.8 Relationship between isotropic and kinematic hardening parameters after Cremer et al., 2001)**

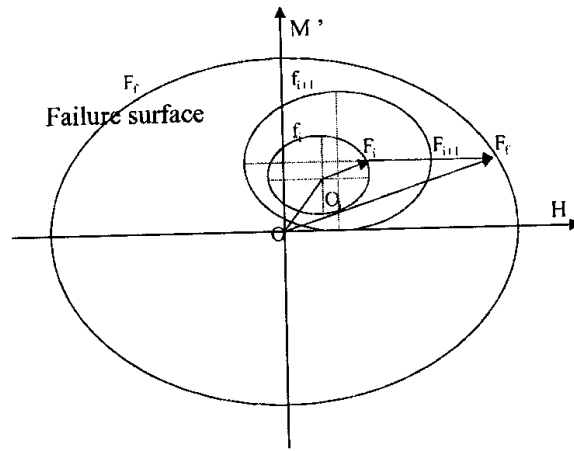


**Fig. 5.9 Noninterpenetration criterion (after Cremer et al., 2001)**

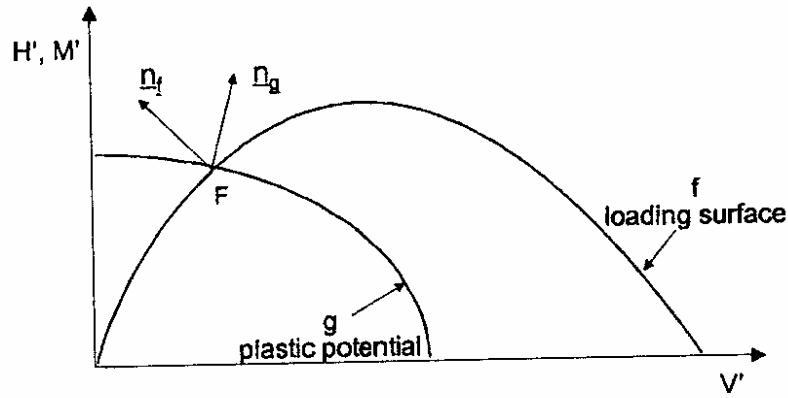


Fig. 5.10 Nonassociative flow rule. External normals of the loading surface and of the plastic potential (after Cremer et al., 2001)

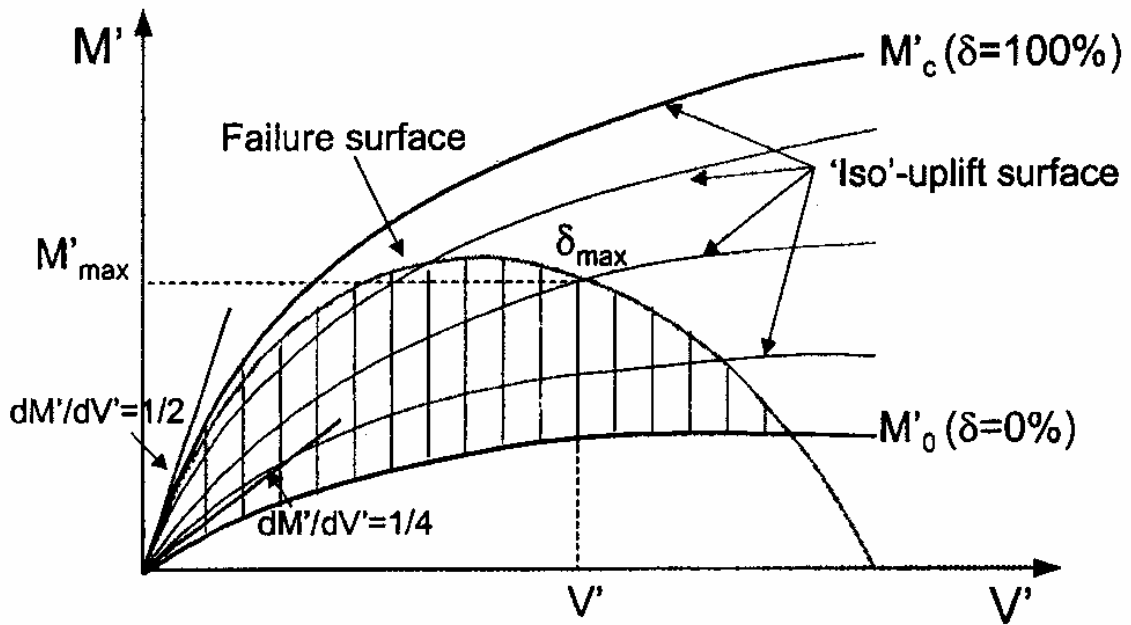


Fig. 5.11 Iso-uplift surfaces and failure criterion in the  $(F_M - F_H)$  plane (after Cremer et al., 2001)

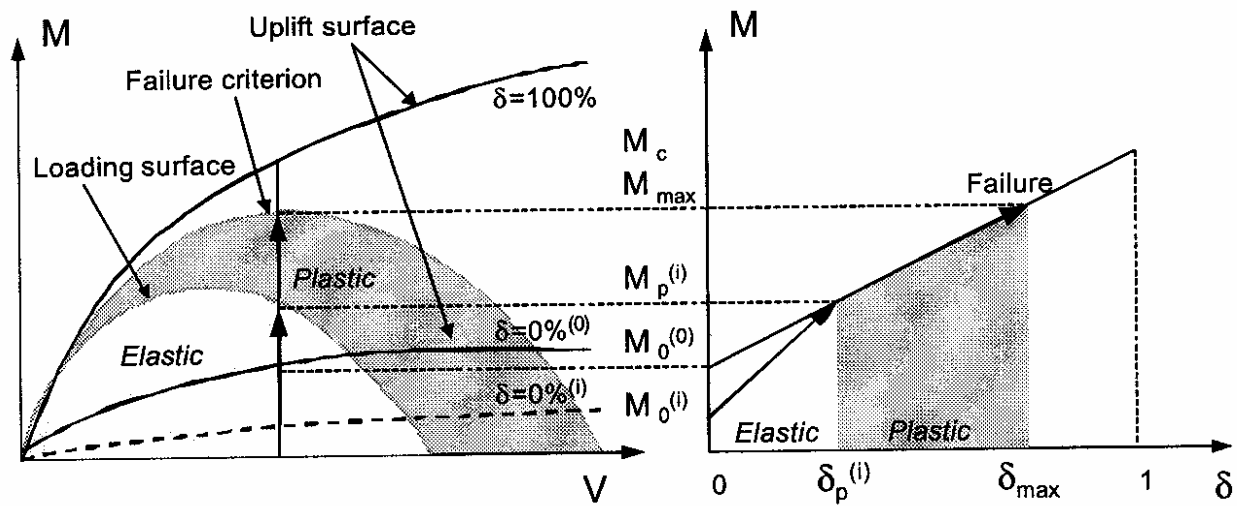


Fig. 5.12 Coupling between plasticity and uplift (Cremer et al., 2001)

## 6 Summary and Preliminary Conclusions

Representation of shallow foundation stiffness by elastic parameters has been the past focus of attention for shallow foundation soil-foundation-structure interaction analyses, and is the approach most cited in existing seismic design codes or guidelines. Such an approach is designed to primarily examine the effect of period shift on force demands. However, for performance-based design of structures, a significant design issue is that of the influence of capacity mobilization of shallow foundations under structural inertial loading, particularly under rocking modes.

The forces induced in buildings or bridges by the response to earthquake ground motion, are limited by the stiffness and capacity of foundation systems. In the case of shallow footings, rocking or uplift provide limiting mechanisms and a source of energy dissipation, and hence use of traditional elastic force-based analysis, can lead to unrealistically high foundation forces. Retrofit to avoid exceeding moment capacity may transfer energy-dissipating mechanisms to the structure and could lead to excessive retrofit cost.

New retrofit guidelines in the United States document nonlinear analysis methods, where displacements are used as a measure of performance. These methods require engineers to establish nonlinear load-deformation characteristics of foundations and allow mobilization of ultimate capacity during earthquake loading, albeit the effects of induced progressive settlement needs to be considered. Analytical studies to date incorporating the nonlinear- and capacity-related moment and rocking behavior of footings in structural response analyses have shown potential benefits to structural ductility demands.

To reinforce the performance-based deformation approach being adopted in seismic design codes, it is clear that an improved understanding of the nonlinear and capacity deformation behavior of shallow footings is needed, particularly for retrofit analyses. Both new experimental data and modeling approaches are required to enable practical design approaches to

be developed with some degree of confidence. This critical need has also been identified by researchers responsible for the development of the Eurocode.

To address the above needs, the PEER research plan is focusing on:

1. The influence of nonlinear deformation and moment capacity on the rocking behavior of shallow footings supporting shear walls.
2. The development of an experimental database for both sands and clay foundation soils using centrifuge testing at UC Davis, to simulate earthquake loading on shear wall structures supported by strip footings.
3. The development and integration of nonlinear Winkler-type spring models (as an interface foundation model) into the PEER structural analysis program OpenSees, and subsequent verification using the centrifuge test results. (UC Irvine research project)
4. The development of a single-element macro model as an alternative interface modeling method. (UC Davis research project)
5. The evaluation of structural response parametric analyses using the above models, to determine the effects of nonlinear response on structural ductility demands.

## **6.1 CENTRIFUGE MODEL TESTS**

The research, to date, has effectively modeled shear walls and their shallow foundations on moderately dense sandy soil to produce seismic response data for varying realistic factors of safety.

1. There is great potential for the soil beneath a footing to dissipate a large amount of energy during dynamic loading. The moment-rotation relationships enclose a large area, and for the dry sand and stiff clay tested to date, the moment-resistance does not decay significantly with amplitude or number of cycles. Data have shown that the backbone of the moment-rotation curve and the hysteresis curves are similar for dynamic and slow cyclic loading tests.
2. The disadvantage of using a footing to dissipate energy is that the footing may experience permanent settlement, sliding, and rotation. These permanent deformations continue to accumulate with the number of cycles of loading, though the rate of accumulation of settlement decreases as the footing embeds itself.

3. An attempt was made to compare a normalized settlement per cycle as a function of the amplitude of the cyclic rotation. The relationship appears fairly consistent for tests in the present study as well as for tests performed by other researchers. The settlements tend to increase as the factor of safety decreases and as the amplitude of rotation increases in a consistent pattern. Building settlements due to dynamic shaking are larger than the building settlements during slow cyclic tests for a given amplitude of rotation. Much of the difference appears to be due to free field settlements, but this point needs further investigation.
4. The observed failure envelopes in moment-axial load space and moment-shear load space seem reasonably consistent with empirical and theoretical envelopes proposed by others.

## **6.2 MODELING FOUNDATION BEHAVIOR USING THE BNWF APPROACH**

A primary objective of this study is to contribute to the accurate numerical modeling of shallow rocking foundations using nonlinear Winkler-based approaches. To date, different experimental data have been collected and used to compare with the numerical solution predicted using a mesh of nonlinear Winkler springs and gap elements placed below the base of representative shallow footing systems. Data considered represent vertical factors of safety  $FS_v$  ranging from 1.5–6.2, including sand and clay and representing both 1g and 20g (centrifuge) experiments. Findings from the study to date include:

1. Reasonable comparison between the nonlinear Winkler-based approach and the experimental data selected can be obtained, provided there is proper selection of properties (stiffness, strength, etc.)
2. The moment-rotational ( $M-\theta$ ) response of foundations resting on clayey soils results in a more pinched behavior and a highly U-shaped settlement-rotation ( $s-\theta$ ) history. Given proper selection of the end spring resistance functions, this U-shaped behavior was captured. ATC-40 (1996) end spring amplifications reasonably account for the increased stiffness at the ends of the foundation, provided the proper length of the increased stiffness zone is selected.
3. The  $M-\theta$  and  $s-\theta$  response using a Winkler mesh is most sensitive to the selection of bearing pressure distribution and magnitude. A parabolic shape resulted in more reasonable comparisons for footings on sands, while an inverse parabolic (higher-end

capacities) resulted in a more reasonable comparison with clay experimental results. The  $M-\theta$  and  $s-\theta$  response using a Winkler mesh is least sensitive to the magnitude of tension capacity provided in the springs

### **6.3 MACRO-ELEMENT MODELING**

A literature review of related macro-element modeling is fairly complete, and we have attempted to implement Cremer's model into a computer code. The model assumes that there are displacements due to elasticity, plasticity, and uplift. The model is quite complex and we have not yet succeeded in implementation. Based upon experience to date we have the following preliminary conclusions:

1. Cremer's model was implemented for clay, but we have not been able to confirm that the predictions would be reasonable for sand. The model assumes elastic behavior for cyclic load that does not exceed the maximum past stress, while the experimental data indicate that there is substantial energy dissipation even for smaller loading cycles.
2. The macro-element models developed by Houlsby and Cassidy are applicable to sand, but their models published to date are largely limited to monotonic loading. A difference between the Houlsby and Cassidy model is that loads are normalized by the maximum past vertical load; rather than the vertical bearing capacity.
3. An improved macro-element model may be derived by combining the features of Cremer's model with those of the Houlsby and Cassidy model.

### **6.4 COMMENTS AND SUGGESTIONS FROM WORKSHOP PARTICIPANTS**

Structures were founded in rectangular (strip) footings with different dimensions in all experiments. It was suggested to do some tests with different footing geometry, such as square or circular footings with almost the same bearing capacity, to see the effect of footing geometry on the structural behavior. Footings were tested on dry sand with different densities and one test series on saturated clay. It was also suggested to do some tests on  $c-\phi$  soils.

In all the centrifuge experiments performed to date, settlement continued to increase as the number of cycles increased, though the rate of increase in settlement reduced as the footing

settled down and embedded itself. It was suggested that a number of cycles of loading need to be conducted to see if the settlement stabilizes at some point.

The behavior of structures during tip-over failure, even for shorter structures, is interesting to study. Pure sliding response should be one test case so that we can look at it as a simple shear test to consider the effects of cyclic shear stress on settlement. In experiments so far, the shear wall structures were loaded symmetrically. It is interesting to see the effects of unsymmetrical loading in the lateral direction.

Previous studies presented at the SEAOC convention looked at the effects of rocking and lift-off for braced frames. Their results indicated that, for flexible structures, lift-off had less effect on moment in structures. Rigid shear wall structures and footings were tested in the centrifuge to date. In the next series of experiments, it is advisable to carry out at least one test on a structure with flexible beams and columns.

Two different types of numerical methods to model shallow foundation–soil interface behavior during slow cyclic and dynamic loading were presented in the workshop: the Winkler spring model and macro-element model. Another method, the use of continuum models, is gradually coming into practice. There are advantages and disadvantages to each method of analysis.

Moment-rotation stiffness values used in the Winkler spring model should be directly compared with Gazetas' equations. FLAC analysis by Yan might also help with the selection of Winkler spring stiffness. After the calibration of Winkler spring stiffness, some blind predictions of centrifuge experiments are necessary to validate the Winkler model.

The macro-element model may be hard to calibrate, since it has a factor of safety as its only primary parameter. All analysis methods should be used to look at load combinations from simulations of realistic buildings.

Heterogeneity of soil influences the distribution of loads beneath the foundation. One consideration was that how accurately the real world soil heterogeneity could be included in analyses. The uncertainty in soil properties obtained from site investigation should also be considered regarding the uncertainty in numerical model predictions. Does it really matter if an accurate complicated analysis is used when certain soil properties are uncertain?

The effects of radiation damping should also be included in the analysis. Radiation damping is preferable to nonlinearity of soil. It was questioned whether the soil nonlinearity could be used as a mechanical fuse.

Where does this all fit in PEER's performance-based earthquake engineering framework? Does it require a fourth integral? Or, do we need to include soil and structure in the model that converts intensity measure (IM) to engineering demand parameter (EDP)?

## **6.5 UPDATE AND FUTURE DIRECTIONS**

Following the discussion during the workshop and subsequent progress and findings, an update on the evolution of these PEER research project accomplishments and future directions is presented below.

### **6.5.1 Subgrade Reaction Spring Modeling in OpenSees**

A "ShallowBNWF" TCL/tk script has been developed to enable users to build subgrade reaction spring properties to model foundations beneath shear walls. The script logic has been evaluated by comparing numerical results with data from the UC Davis centrifuge tests. Sensitivity studies have been conducted to study the significance of the various nonlinear spring parameters and their distribution details.

### **6.5.2 Macro-Element Modeling in OpenSees**

The macro-element model development is rapidly progressing now that we have discovered a conceptually simple way to treat the soil-footing interface using a moving contact model. The insight from this work is complementing a parallel development of a bounding-surface-type model for the macro element. The macro-element model(s) are being implemented in OpenSees and will be compared to the centrifuge test data and to a parallel modeling effort under way at UC Irvine.

### **6.5.3 Centrifuge Model Testing**

We have developed a new, two-actuator loading mechanism to allow independent control of rotation and sliding. This device would enable obtaining significantly more data from each model structure, as load paths would not be restricted to a constant moment to shear ratio. We

continue to investigate the observed differences in the amount of settlement that occurs during shaking tests as opposed to the settlement that occurs during slow cyclic tests. In the next phase of testing, we are hoping to model shear walls with a moment frame building attached. This would be the first time that a combined “building” and shear wall with a foundation resting on nonlinear soil will be shaken in a controlled experiment. This will provide unique, system-level data that should enable direct observation of how footing behavior is propagated into demand on the building structure. We are extending the parametric study to include footings of different shape and footings in intermediate soil types.

#### **6.5.4 An Eye on the Bigger Picture**

Now that a significant set of data is available and we are gaining confidence in the numerical procedures, it will be important to step back and compare the results to current methods used in design practice for estimating inelastic displacement demands (e.g., FEMA 356/273, ICB 2003, ATC-40). These comparisons would help answer the question: How accurate are these simplified procedures when rocking is allowed at the foundation? Furthermore, the incompatibility of the stiffness of the combined structural system (frame and shear wall) and the relatively stiff shear wall, results in difficulties when using simple design methods (e.g., at the connection between the two systems).

More attention will also be focused on providing recommendations on how the new footing elements in OpenSees can be used in a probabilistic-based framework. That is, we need to resolve how to propagate uncertainties in field measurements of soil properties to uncertainties in the new constitutive model parameters and finally into the demands placed on the building. This would likely be done using an exploratory set of Monte Carlo simulations.

Additional PEER shallow foundations work is also planned where parameters will be added to UCI BNWF models to account for radiation damping and for kinematic interaction due to base-slab averaging. Finally, we will start from a hazard curve and integrate the uncertainties to get EDPs and their dispersion for implementation in the framework of performance-based design (PBD). This effort will help integrate results from this focused study to PEER's larger mission of developing a robust PBD framework.

## REFERENCES

The most recent publications resulting from this research are summarized below (alphabetically):

- Gajan, S., Phalen, J. D., Kutter, B. L. 2003. *Soil-foundation-structure interaction: Shallow foundations, Centrifuge Data Report for SSG02*. Report No. UCD/CGMDR-03/01. Center for Geotechnical Modeling, UC Davis
- Gajan, S., Phalen, J. D., Kutter, B. L. 2003. *Soil-foundation-structure interaction: Shallow foundations, Centrifuge Data Report for SSG03*. Report No. UCD/CGMDR-03/02. Center for Geotechnical Modeling, UC Davis.
- Gajan, S., Phalen, J. D., Kutter, B. L., Hutchinson, T. C. and Martin, G. 2004. Centrifuge modeling of nonlinear cyclic load-deformation behavior of shallow foundations. *Proc. 11th Intl. Conf. Soil Dynamics and Earthquake Engineering*. UC Berkeley.
- Harden, C. (2003). Numerical modeling of the nonlinear cyclic response of shallow foundations. M.S. thesis, University of California, Irvine.
- Harden, C., Hutchinson, T. C., Kutter, B. L., Martin, G. 2005. *Numerical modeling of the nonlinear cyclic response of shallow foundations*. PEER Report 2005/04.
- Harden, C., Hutchinson, T. C., Moore, M. 2004. Investigation into the effects of foundation uplift on simplified seismic design procedures. *Proceedings of the Structural Engineers Association of California (SEAOC)*.
- Phalen, J. D. 2003. Physical modeling of the soil-foundation interaction of spread footings subjected to lateral cyclic loading, M.S. thesis, University of California, Davis, College of Engineering.
- Rosebrook, K. R., Kutter, B. L. 2001. *Soil-foundation-structure interaction: Shallow foundations. Centrifuge Data Report for test series KRR01*. University of California, Davis, Report No. UCD/CGMDR-01/09.
- Rosebrook, K. R., Kutter, B. L. 2001. *Soil-foundation-structure interaction: Shallow foundations. Centrifuge Data Report for test series KRR02*. University of California, Davis, Report No. UCD/CGMDR-01/10.
- Rosebrook, K. R., Kutter, B. L. 2001. *Soil-foundation-structure interaction: Shallow foundations. Centrifuge Data Report for test series KRR03*. University of California, Davis, Report No. UCD/CGMDR-01/11.
- Rosebrook, K. R. (2001) Moment loading on shallow foundations: Centrifuge test data archives. M.S. thesis, University of California, Davis, College of Engineering.

## PEER REPORTS

PEER reports are available from the National Information Service for Earthquake Engineering (NISEE). To order PEER reports, please contact the Pacific Earthquake Engineering Research Center, 1301 South 46<sup>th</sup> Street, Richmond, California 94804-4698. Tel.: (510) 231-9468; Fax: (510) 231-9 461.

- PEER 2005/14** *Workshop on Modeling of Nonlinear Cyclic Load-Deformation Behavior of Shallow Foundations.* Bruce L. Kutter, Geoffrey Martin, Tara Hutchinson, Chad Harden, Sivapalan Gajan, and Justin Phalen. March 2006.
- PEER 2005/12** *PEER Testbed Study on a Laboratory Building: Exercising Seismic Performance Assessment.* Mary C. Comerio, editor. November 2005.
- PEER 2005/11** *Van Nuys Hotel Building Testbed Report: Exercising Seismic Performance Assessment.* Helmut Krawinkler, editor. October 2005.
- PEER 2005/10** *First NEES/E-Defense Workshop on Collapse Simulation of Reinforced Concrete Building Structures.* September 2005.
- PEER 2005/07** *Experimental and Analytical Studies on the Seismic Response of Freestanding and Anchored Laboratory Equipment.* Dimitrios Konstantinidis and Nicos Makris. January 2005.
- PEER 2005/06** *Global Collapse of Frame Structures under Seismic Excitations.* Luis F. Ibarra and Helmut Krawinkler. September 2005.
- PEER 2005/04** *Numerical Modeling of the Nonlinear Cyclic Response of Shallow Foundations.* Chad Harden, Tara Hutchinson, Geoffrey R. Martin, and Bruce L. Kutter. August 2005.
- PEER 2005/03** *A Taxonomy of Building Components for Performance-Based Earthquake Engineering.* Keith A. Porter. September 2005.
- PEER 2005/02** *Fragility Basis for California Highway Overpass Bridge Seismic Decision Making.* Kevin R. Mackie and Bozidar Stojadinovic. June 2005.
- PEER 2005/01** *Empirical Characterization of Site Conditions on Strong Ground Motion.* Jonathan P. Stewart, Yoojoong Choi, and Robert W. Graves. June 2005.
- PEER 2004/09** *Electrical Substation Equipment Interaction: Experimental Rigid Conductor Studies.* Christopher Stearns and André Filiatrault. February 2005.
- PEER 2004/08** *Seismic Qualification and Fragility Testing of Line Break 550-kV Disconnect Switches.* Shakhzod M. Takhirov, Gregory L. Fenves, and Eric Fujisaki. January 2005.
- PEER 2004/07** *Ground Motions for Earthquake Simulator Qualification of Electrical Substation Equipment.* Shakhzod M. Takhirov, Gregory L. Fenves, Eric Fujisaki, and Don Clyde. January 2005.
- PEER 2004/06** *Performance-Based Regulation and Regulatory Regimes.* Peter J. May and Chris Koski. September 2004.
- PEER 2004/05** *Performance-Based Seismic Design Concepts and Implementation: Proceedings of an International Workshop.* Peter Fajfar and Helmut Krawinkler, editors. September 2004.
- PEER 2004/04** *Seismic Performance of an Instrumented Tilt-up Wall Building.* James C. Anderson and Vitelmo V. Bertero. July 2004.
- PEER 2004/03** *Evaluation and Application of Concrete Tilt-up Assessment Methodologies.* Timothy Graf and James O. Malley. October 2004.
- PEER 2004/02** *Analytical Investigations of New Methods for Reducing Residual Displacements of Reinforced Concrete Bridge Columns.* Junichi Sakai and Stephen A. Mahin. August 2004.
- PEER 2004/01** *Seismic Performance of Masonry Buildings and Design Implications.* Kerri Anne Taeko Tokoro, James C. Anderson, and Vitelmo V. Bertero. February 2004.
- PEER 2003/18** *Performance Models for Flexural Damage in Reinforced Concrete Columns.* Michael Berry and Marc Eberhard. August 2003.
- PEER 2003/17** *Predicting Earthquake Damage in Older Reinforced Concrete Beam-Column Joints.* Catherine Pagni and Laura Lowes. October 2004.

- PEER 2003/16** *Seismic Demands for Performance-Based Design of Bridges*. Kevin Mackie and Božidar Stojadinovic. August 2003.
- PEER 2003/15** *Seismic Demands for Nondeteriorating Frame Structures and Their Dependence on Ground Motions*. Ricardo Antonio Medina and Helmut Krawinkler. May 2004.
- PEER 2003/14** *Finite Element Reliability and Sensitivity Methods for Performance-Based Earthquake Engineering*. Terje Haukaas and Armen Der Kiureghian. April 2004.
- PEER 2003/13** *Effects of Connection Hysteretic Degradation on the Seismic Behavior of Steel Moment-Resisting Frames*. Janise E. Rodgers and Stephen A. Mahin. March 2004.
- PEER 2003/12** *Implementation Manual for the Seismic Protection of Laboratory Contents: Format and Case Studies*. William T. Holmes and Mary C. Comerio. October 2003.
- PEER 2003/11** *Fifth U.S.-Japan Workshop on Performance-Based Earthquake Engineering Methodology for Reinforced Concrete Building Structures*. February 2004.
- PEER 2003/10** *A Beam-Column Joint Model for Simulating the Earthquake Response of Reinforced Concrete Frames*. Laura N. Lowes, Nilanjan Mitra, and Arash Altoontash. February 2004.
- PEER 2003/09** *Sequencing Repairs after an Earthquake: An Economic Approach*. Marco Casari and Simon J. Wilkie. April 2004.
- PEER 2003/08** *A Technical Framework for Probability-Based Demand and Capacity Factor Design (DCFD) Seismic Formats*. Fatemeh Jalayer and C. Allin Cornell. November 2003.
- PEER 2003/07** *Uncertainty Specification and Propagation for Loss Estimation Using FOSM Methods*. Jack W. Baker and C. Allin Cornell. September 2003.
- PEER 2003/06** *Performance of Circular Reinforced Concrete Bridge Columns under Bidirectional Earthquake Loading*. Mahmoud M. Hachem, Stephen A. Mahin, and Jack P. Moehle. February 2003.
- PEER 2003/05** *Response Assessment for Building-Specific Loss Estimation*. Eduardo Miranda and Shahram Taghavi. September 2003.
- PEER 2003/04** *Experimental Assessment of Columns with Short Lap Splices Subjected to Cyclic Loads*. Murat Melek, John W. Wallace, and Joel Conte. April 2003.
- PEER 2003/03** *Probabilistic Response Assessment for Building-Specific Loss Estimation*. Eduardo Miranda and Hesameddin Aslani. September 2003.
- PEER 2003/02** *Software Framework for Collaborative Development of Nonlinear Dynamic Analysis Program*. Jun Peng and Kincho H. Law. September 2003.
- PEER 2003/01** *Shake Table Tests and Analytical Studies on the Gravity Load Collapse of Reinforced Concrete Frames*. Kenneth John Elwood and Jack P. Moehle. November 2003.
- PEER 2002/24** *Performance of Beam to Column Bridge Joints Subjected to a Large Velocity Pulse*. Natalie Gibson, André Filiatrault, and Scott A. Ashford. April 2002.
- PEER 2002/23** *Effects of Large Velocity Pulses on Reinforced Concrete Bridge Columns*. Greg L. Orozco and Scott A. Ashford. April 2002.
- PEER 2002/22** *Characterization of Large Velocity Pulses for Laboratory Testing*. Kenneth E. Cox and Scott A. Ashford. April 2002.
- PEER 2002/21** *Fourth U.S.-Japan Workshop on Performance-Based Earthquake Engineering Methodology for Reinforced Concrete Building Structures*. December 2002.
- PEER 2002/20** *Barriers to Adoption and Implementation of PBEE Innovations*. Peter J. May. August 2002.
- PEER 2002/19** *Economic-Engineered Integrated Models for Earthquakes: Socioeconomic Impacts*. Peter Gordon, James E. Moore II, and Harry W. Richardson. July 2002.
- PEER 2002/18** *Assessment of Reinforced Concrete Building Exterior Joints with Substandard Details*. Chris P. Pantelides, Jon Hansen, Justin Nadauld, and Lawrence D. Reaveley. May 2002.
- PEER 2002/17** *Structural Characterization and Seismic Response Analysis of a Highway Overcrossing Equipped with Elastomeric Bearings and Fluid Dampers: A Case Study*. Nicos Makris and Jian Zhang. November 2002.
- PEER 2002/16** *Estimation of Uncertainty in Geotechnical Properties for Performance-Based Earthquake Engineering*. Allen L. Jones, Steven L. Kramer, and Pedro Arduino. December 2002.

- PEER 2002/15** *Seismic Behavior of Bridge Columns Subjected to Various Loading Patterns.* Asadollah Esmaeily-Gh. and Yan Xiao. December 2002.
- PEER 2002/14** *Inelastic Seismic Response of Extended Pile Shaft Supported Bridge Structures.* T.C. Hutchinson, R.W. Boulanger, Y.H. Chai, and I.M. Idriss. December 2002.
- PEER 2002/13** *Probabilistic Models and Fragility Estimates for Bridge Components and Systems.* Paolo Gardoni, Armen Der Kiureghian, and Khalid M. Mosalam. June 2002.
- PEER 2002/12** *Effects of Fault Dip and Slip Rake on Near-Source Ground Motions: Why Chi-Chi Was a Relatively Mild M7.6 Earthquake.* Brad T. Aagaard, John F. Hall, and Thomas H. Heaton. December 2002.
- PEER 2002/11** *Analytical and Experimental Study of Fiber-Reinforced Strip Isolators.* James M. Kelly and Shakhzod M. Takhirov. September 2002.
- PEER 2002/10** *Centrifuge Modeling of Settlement and Lateral Spreading with Comparisons to Numerical Analyses.* Sivapalan Gajan and Bruce L. Kutter. January 2003.
- PEER 2002/09** *Documentation and Analysis of Field Case Histories of Seismic Compression during the 1994 Northridge, California, Earthquake.* Jonathan P. Stewart, Patrick M. Smith, Daniel H. Whang, and Jonathan D. Bray. October 2002.
- PEER 2002/08** *Component Testing, Stability Analysis and Characterization of Buckling-Restrained Unbonded Braces™.* Cameron Black, Nicos Makris, and Ian Aiken. September 2002.
- PEER 2002/07** *Seismic Performance of Pile-Wharf Connections.* Charles W. Roeder, Robert Graff, Jennifer Soderstrom, and Jun Han Yoo. December 2001.
- PEER 2002/06** *The Use of Benefit-Cost Analysis for Evaluation of Performance-Based Earthquake Engineering Decisions.* Richard O. Zerbe and Anthony Falit-Baiamonte. September 2001.
- PEER 2002/05** *Guidelines, Specifications, and Seismic Performance Characterization of Nonstructural Building Components and Equipment.* André Filiatrault, Constantin Christopoulos, and Christopher Stearns. September 2001.
- PEER 2002/04** *Consortium of Organizations for Strong-Motion Observation Systems and the Pacific Earthquake Engineering Research Center Lifelines Program: Invited Workshop on Archiving and Web Dissemination of Geotechnical Data, 4–5 October 2001.* September 2002.
- PEER 2002/03** *Investigation of Sensitivity of Building Loss Estimates to Major Uncertain Variables for the Van Nuys Testbed.* Keith A. Porter, James L. Beck, and Rustem V. Shaikhutdinov. August 2002.
- PEER 2002/02** *The Third U.S.-Japan Workshop on Performance-Based Earthquake Engineering Methodology for Reinforced Concrete Building Structures.* July 2002.
- PEER 2002/01** *Nonstructural Loss Estimation: The UC Berkeley Case Study.* Mary C. Comerio and John C. Stallmeyer. December 2001.
- PEER 2001/16** *Statistics of SDF-System Estimate of Roof Displacement for Pushover Analysis of Buildings.* Anil K. Chopra, Rakesh K. Goel, and Chatpan Chintanapakdee. December 2001.
- PEER 2001/15** *Damage to Bridges during the 2001 Nisqually Earthquake.* R. Tyler Ranf, Marc O. Eberhard, and Michael P. Berry. November 2001.
- PEER 2001/14** *Rocking Response of Equipment Anchored to a Base Foundation.* Nicos Makris and Cameron J. Black. September 2001.
- PEER 2001/13** *Modeling Soil Liquefaction Hazards for Performance-Based Earthquake Engineering.* Steven L. Kramer and Ahmed-W. Elgamal. February 2001.
- PEER 2001/12** *Development of Geotechnical Capabilities in OpenSees.* Boris Jeremić. September 2001.
- PEER 2001/11** *Analytical and Experimental Study of Fiber-Reinforced Elastomeric Isolators.* James M. Kelly and Shakhzod M. Takhirov. September 2001.
- PEER 2001/10** *Amplification Factors for Spectral Acceleration in Active Regions.* Jonathan P. Stewart, Andrew H. Liu, Yoojoong Choi, and Mehmet B. Baturay. December 2001.
- PEER 2001/09** *Ground Motion Evaluation Procedures for Performance-Based Design.* Jonathan P. Stewart, Shyh-Jeng Chiou, Jonathan D. Bray, Robert W. Graves, Paul G. Somerville, and Norman A. Abrahamson. September 2001.
- PEER 2001/08** *Experimental and Computational Evaluation of Reinforced Concrete Bridge Beam-Column Connections for Seismic Performance.* Clay J. Naito, Jack P. Moehle, and Khalid M. Mosalam. November 2001.

- PEER 2001/07** *The Rocking Spectrum and the Shortcomings of Design Guidelines.* Nicos Makris and Dimitrios Konstantinidis. August 2001.
- PEER 2001/06** *Development of an Electrical Substation Equipment Performance Database for Evaluation of Equipment Fragilities.* Thalia Agnanos. April 1999.
- PEER 2001/05** *Stiffness Analysis of Fiber-Reinforced Elastomeric Isolators.* Hsiang-Chuan Tsai and James M. Kelly. May 2001.
- PEER 2001/04** *Organizational and Societal Considerations for Performance-Based Earthquake Engineering.* Peter J. May. April 2001.
- PEER 2001/03** *A Modal Pushover Analysis Procedure to Estimate Seismic Demands for Buildings: Theory and Preliminary Evaluation.* Anil K. Chopra and Rakesh K. Goel. January 2001.
- PEER 2001/02** *Seismic Response Analysis of Highway Overcrossings Including Soil-Structure Interaction.* Jian Zhang and Nicos Makris. March 2001.
- PEER 2001/01** *Experimental Study of Large Seismic Steel Beam-to-Column Connections.* Egor P. Popov and Shakhzod M. Takhirov. November 2000.
- PEER 2000/10** *The Second U.S.-Japan Workshop on Performance-Based Earthquake Engineering Methodology for Reinforced Concrete Building Structures.* March 2000.
- PEER 2000/09** *Structural Engineering Reconnaissance of the August 17, 1999 Earthquake: Kocaeli (Izmit), Turkey.* Halil Sezen, Kenneth J. Elwood, Andrew S. Whittaker, Khalid Mosalam, John J. Wallace, and John F. Stanton. December 2000.
- PEER 2000/08** *Behavior of Reinforced Concrete Bridge Columns Having Varying Aspect Ratios and Varying Lengths of Confinement.* Anthony J. Calderone, Dawn E. Lehman, and Jack P. Moehle. January 2001.
- PEER 2000/07** *Cover-Plate and Flange-Plate Reinforced Steel Moment-Resisting Connections.* Taejin Kim, Andrew S. Whittaker, Amir S. Gilani, Vitelmo V. Bertero, and Shakhzod M. Takhirov. September 2000.
- PEER 2000/06** *Seismic Evaluation and Analysis of 230-kV Disconnect Switches.* Amir S. J. Gilani, Andrew S. Whittaker, Gregory L. Fenves, Chun-Hao Chen, Henry Ho, and Eric Fujisaki. July 2000.
- PEER 2000/05** *Performance-Based Evaluation of Exterior Reinforced Concrete Building Joints for Seismic Excitation.* Chandra Clyde, Chris P. Pantelides, and Lawrence D. Reaveley. July 2000.
- PEER 2000/04** *An Evaluation of Seismic Energy Demand: An Attenuation Approach.* Chung-Che Chou and Chia-Ming Uang. July 1999.
- PEER 2000/03** *Framing Earthquake Retrofitting Decisions: The Case of Hillside Homes in Los Angeles.* Detlof von Winterfeldt, Nels Roselund, and Alicia Kitsuse. March 2000.
- PEER 2000/02** *U.S.-Japan Workshop on the Effects of Near-Field Earthquake Shaking.* Andrew Whittaker, ed. July 2000.
- PEER 2000/01** *Further Studies on Seismic Interaction in Interconnected Electrical Substation Equipment.* Armen Der Kiureghian, Kee-Jeung Hong, and Jerome L. Sackman. November 1999.
- PEER 1999/14** *Seismic Evaluation and Retrofit of 230-kV Porcelain Transformer Bushings.* Amir S. Gilani, Andrew S. Whittaker, Gregory L. Fenves, and Eric Fujisaki. December 1999.
- PEER 1999/13** *Building Vulnerability Studies: Modeling and Evaluation of Tilt-up and Steel Reinforced Concrete Buildings.* John W. Wallace, Jonathan P. Stewart, and Andrew S. Whittaker, editors. December 1999.
- PEER 1999/12** *Rehabilitation of Nonductile RC Frame Building Using Encasement Plates and Energy-Dissipating Devices.* Mehrdad Sasani, Vitelmo V. Bertero, James C. Anderson. December 1999.
- PEER 1999/11** *Performance Evaluation Database for Concrete Bridge Components and Systems under Simulated Seismic Loads.* Yael D. Hose and Frieder Seible. November 1999.
- PEER 1999/10** *U.S.-Japan Workshop on Performance-Based Earthquake Engineering Methodology for Reinforced Concrete Building Structures.* December 1999.
- PEER 1999/09** *Performance Improvement of Long Period Building Structures Subjected to Severe Pulse-Type Ground Motions.* James C. Anderson, Vitelmo V. Bertero, and Raul Bertero. October 1999.
- PEER 1999/08** *Envelopes for Seismic Response Vectors.* Charles Menun and Armen Der Kiureghian. July 1999.

- PEER 1999/07** *Documentation of Strengths and Weaknesses of Current Computer Analysis Methods for Seismic Performance of Reinforced Concrete Members.* William F. Cofer. November 1999.
- PEER 1999/06** *Rocking Response and Overturning of Anchored Equipment under Seismic Excitations.* Nicos Makris and Jian Zhang. November 1999.
- PEER 1999/05** *Seismic Evaluation of 550 kV Porcelain Transformer Bushings.* Amir S. Gilani, Andrew S. Whittaker, Gregory L. Fenves, and Eric Fujisaki. October 1999.
- PEER 1999/04** *Adoption and Enforcement of Earthquake Risk-Reduction Measures.* Peter J. May, Raymond J. Burby, T. Jens Feeley, and Robert Wood.
- PEER 1999/03** *Task 3 Characterization of Site Response General Site Categories.* Adrian Rodriguez-Marek, Jonathan D. Bray, and Norman Abrahamson. February 1999.
- PEER 1999/02** *Capacity-Demand-Diagram Methods for Estimating Seismic Deformation of Inelastic Structures: SDF Systems.* Anil K. Chopra and Rakesh Goel. April 1999.
- PEER 1999/01** *Interaction in Interconnected Electrical Substation Equipment Subjected to Earthquake Ground Motions.* Armen Der Kiureghian, Jerome L. Sackman, and Kee-Jeung Hong. February 1999.
- PEER 1998/08** *Behavior and Failure Analysis of a Multiple-Frame Highway Bridge in the 1994 Northridge Earthquake.* Gregory L. Fenves and Michael Ellery. December 1998.
- PEER 1998/07** *Empirical Evaluation of Inertial Soil-Structure Interaction Effects.* Jonathan P. Stewart, Raymond B. Seed, and Gregory L. Fenves. November 1998.
- PEER 1998/06** *Effect of Damping Mechanisms on the Response of Seismic Isolated Structures.* Nicos Makris and Shih-Po Chang. November 1998.
- PEER 1998/05** *Rocking Response and Overturning of Equipment under Horizontal Pulse-Type Motions.* Nicos Makris and Yiannis Roussos. October 1998.
- PEER 1998/04** *Pacific Earthquake Engineering Research Invitational Workshop Proceedings, May 14–15, 1998: Defining the Links between Planning, Policy Analysis, Economics and Earthquake Engineering.* Mary Comerio and Peter Gordon. September 1998.
- PEER 1998/03** *Repair/Upgrade Procedures for Welded Beam to Column Connections.* James C. Anderson and Xiaojing Duan. May 1998.
- PEER 1998/02** *Seismic Evaluation of 196 kV Porcelain Transformer Bushings.* Amir S. Gilani, Juan W. Chavez, Gregory L. Fenves, and Andrew S. Whittaker. May 1998.
- PEER 1998/01** *Seismic Performance of Well-Confined Concrete Bridge Columns.* Dawn E. Lehman and Jack P. Moehle. December 2000.